

Multifunctional thermosensitive liposomes for antitumor therapy

Dissertation

zur

Erlangung des Doktorgrades
der Naturwissenschaften

(Dr. rer. nat.)

dem

Fachbereich Pharmazie der
Philipps-Universität Marburg
vorgelegt von

Tan Shi

aus

Heilongjiang, China

Marburg/Lahn 2023

Erstgutachter: **Prof. Dr. Udo Bakowsky**
Zweitgutachter: **Prof. Dr. Frank Runkel**

Eingereicht am **10.08.2023**

Tag der mündlichen Prüfung am **26.09.2023**

Hochschulkenziffer: **1180**

Multifunctional thermosensitive liposomes for antitumor therapy

Thesis

Submitted in the fulfillment of the requirements of the degree of

Doctor of Natural Sciences (Dr.rer.nat.)

equivalent to

Doctor of Philosophy (Ph.D.)

to

The Faculty of Pharmacy,
Philipps University of Marburg

by

Tan Shi

from

Heilongjiang, China

Marburg/Lahn **2023**

First advisor: **Prof. Dr. Udo Bakowsky**
Second advisor: **Prof. Dr. Frank Runkel**

Submitted on **10.08.2023**

Examination day **26.09.2023**

Hochschulkenziffer: **1180**

Die vorliegende Arbeit entstand auf Anregung und unter der Leitung von

Prof. Dr. Udo Bakowsky

am Institut für Pharmazeutische Technologie und Biopharmazie

der Philipps-Universität Marburg

To my dear grandma, your blessing is the eternal light in the darkness.

*To my beloved mom and dad, your love and encouragement give me the strength to face any
challenges in life.*

献给我的家人

ERKLÄRUNG

Ich versichere, dass ich meine Dissertation

„Multifunctional thermosensitive liposomes for antitumor therapy“

selbständig ohne unerlaubte Hilfe angefertigt und mich dabei keiner anderen als der von mir ausdrücklich bezeichneten Quellen bedient habe. Alle vollständig oder sinngemäß übernommenen Zitate sind als solche gekennzeichnet.

Die Dissertation wurde in der jetzigen oder einer ähnlichen Form noch bei keiner anderen Hochschule eingereicht und hat noch keinen sonstigen Prüfungszwecken gedient.

Marburg, den 10.08.2023

(Tan Shi)

STATUTORY DECLARATION

I declare that this doctoral thesis

“Multifunctional thermosensitive liposomes for antitumor therapy”

has been written entirely by myself except unless stated otherwise by reference or acknowledgment. The research was carried out at the Department of Pharmaceutics and Biopharmaceutics, Philipps University of Marburg, under the supervision of Professor Udo Bakowsky.

This thesis has not been submitted in any form elsewhere for a higher degree.

Marburg, 10.08.2023

(Tan Shi)

Acknowledgement

It has been a wonderful journey pursuing a PhD degree at Philipps University Marburg. I would like to take this opportunity to express my heartfelt gratitude to the incredible network of colleagues, friends and family who have supported me. Their unwavering encouragement, understanding, and love have been the pillars of strength that pushed me forward, and for that, I am immensely grateful. I'm so glad working in this great group with great peoples who supported and accompanied me in accomplishing this dissertation.

First and foremost, I would like to express my most sincere gratitude to my supervisor Prof. Dr. Udo Bakowsky. Without his guidance and utmost support throughout my study, this work would have never been accomplished. I appreciate it more than I can say.

I would like to thank to my committee, Prof. Dr. Frank Runkel, Prof. Dr. Cornelius Krasel, Prof. Dr. Torsten Steinmetzer. I'm gratefully in your support and contribution of your time and energy on my dissertation; I appreciate a lot for your valuable comments.

I would like to acknowledge Dr. Jana Brüller, who supported me a lot at the beginning of my PhD. She was always available when I needed her professional advice and the conversations always resulted in good discussions.

Great thanks to Dr. Jens Schäfer, Dr. Shashank Pinnapireddy, Dr. Eduard Preis for their technical assistance and professional advice during my research.

Special thanks go to Dr. Umair Amin for his positive encouragement at different stage of my study and support in CLSM and TEM images; Dr. Konrad Engelhardt, who spent mass of time on the great AFM images.

I would like to especially thank Mrs. Eva Maria Mohr, who led me to the cell culture and always encouraged me when I'm stressed and lack of confidence. She showed me the greatest love such as a family member.

I would like to thank Julia Michaelis, Mrs. Susanne Lüttebrandt, Mrs. Henriette Dietrich, Dr. Jarmila Jedelská and Mrs. Doris Reissenweber for their technical assistance and uttermost patience and support.

I'm very grateful for Abdallah Ayoub for his numerous supports of many experiments and fruitful conversations during my study, which I appreciate a lot.

I want to extend my thanks to all my past and current research group colleagues: Dr. Mohamad Alawak, Dr. Muhammad Yasir Ali, Dr. Sajid Ali, Martina Bonsu, Lena Bender, Valeri Roschenko, Dr. Ahmad Mohamed, Dr. Michael Raschpichlar, Julia Janina Schürer, Dr. Hirva Shah, Jan Schulze, Dr. Jennifer Lehmann, Dr. Sascha Hubing, Dr. Bernd Gutberlet, Stefanie Klein and Dr. Lili Duse and Dr. Matthias Wojcik.

I would like to thank Prof. Dr. Jörg Bartsch, who brought me grate support and encouragement at the wobbly start.

Throughout the PhD study, there is so much love I would appreciate for my whole life.

Dr. Alice Abu Dayyih, who always brings me warmth and light as an angel and supports me personally and professionally, Dr. Abraham Abraham shows me the most genuine care and always reminds me that I'm not alone.

I'm also eternally grateful to my friends who supported me throughout my whole study in Germany. Wen Li, Yunyun Mu, Jenny Zhou, Haowen Wang, Dr. Liujuan Zheng, we support and encourage each other in the difficult time, and celebrate together in happy moments.

Shan Jiang, Ke Chen, Xinyu Wang, Lingna Dai, Yuqian Wu, who sent me continuously virtual love through internet.

Lika Kohl, Sergey Shifrin, Carolin Naumann, Benedikt Naumann, who we spent countless Saturday nights and witnessed all the big moments of each other.

Additionally, I would like to thank Daniela Mey, Olivia Naumann, Kai Schulze and Gypsi, thank you for bringing this warm family atmosphere and releasing my stress. It would have been a great loss without your genuine care.

I would like to thank my husband, Linus Naumann, who cheers me up when I had impostor syndrome and always says "don't believe yourself, believe me who believes in you". Thank you for the joy you bring; for the support, encouragement and companionship; for creating the comfortable environment that allows me to focus on my work. Your love, sacrifices, understanding, and unwavering support have been the driving force behind my success in completing this doctoral journey. I'm truly blessed to have you as my partner in life. I'm looking forward to exploring the world with you and creating our fulfilling life together.

At the end, I would bring my deepest appreciation to my beloved parents, who always support and encourage me, enabling me to go further on my educational journey. Your wisdom and patience are the most precious treasures in my life. I appreciate the education and nurturing that shaped me into the person I am today. You support me to chase my dream and always stand as my unwavering pillars of strength and guides. The constant belief and unconditional love have been essential in my life.

This was the most unforgettable journey I have had. While challenging, it was undoubtedly exciting. Thanks for everyone I have met along the way.

Table of content

1. Introduction.....	1
1.1 Triple negative breast cancer	2
1.2 Doxorubicin (DOX).....	2
1.2.1 History and structure of Doxorubicin	2
1.2.2 Mechanism of activity.....	3
1.2.3 Doxorubicin in cancer therapy.....	4
1.3 Liposomes.....	5
1.3.1 Definition and structure	5
1.3.2 PEGylated liposomes	8
1.3.3 Lipid.....	9
1.3.4.1 DPPC and DSPC.....	9
1.3.4.2 DSPE-mPEG-2000	9
1.3.4.3 Cholesterol	10
1.3.4 Doxorubicin remote loading	10
1.3.5 Thermosensitive liposomes and triggered release	11
1.3.6 Thermotropic behavior of the phospholipid bilayer	12
1.4 EPR effect	13
1.5 Hyperthermia in cancer therapy.....	15
1.6 Indocyanine green (ICG)	18
1.6.1 History and structure.....	18
1.6.2 ICG in photodynamic therapy.....	20
1.6.3 ICG in photothermal therapy	21
1.6.4 Clinical usage of ICG.....	23
1.6.5 Liposomal ICG formulation.....	24
1.7 3D cell culture.....	25
1.7.1 Background and structure of 3D cell culture	25
1.7.2 Comparison of 2D and 3D cell culture	26

1.7.3	3D cell culture in modern drug development	27
1.8	Aims and objectives	29
2	Materials and methods	31
2.1	Materials and devices.....	32
2.1.1	List of materials and chemicals.....	32
2.1.2	List of devices	35
2.2	Methods.....	37
2.2.1	Preparation of liposome	37
2.2.1.1	Thin-film hydration method.....	37
2.2.1.2	Preparation of doxorubicin thermosensitive liposomes (DOX-TSL)	38
2.2.1.3	Preparation of multifunctional liposomes (ICG-DOX-mTSL).....	39
2.2.2	Light source	40
2.2.3	Characterization of Liposomes	40
2.2.3.1	Dynamic light scattering (DLS).....	40
2.2.3.2	Laser Doppler velocimetry (LDV).....	41
2.2.3.3	Atomic force microscopy (AFM)	41
2.2.3.4	Transmission electron microscopy (TEM)	41
2.2.3.5	Differential scanning calorimetry (DSC).....	42
2.2.3.6	Encapsulation efficiency	42
2.2.3.7	Liposomes stability	43
2.2.3.8	Drug release	43
2.2.4	Cell culture experiments	44
2.2.4.1	Cell condition.....	44
2.2.4.2	3D cell culture model (spheroids) formation	44
2.2.4.3	Cytotoxicity studies of DOX-TSL upon hyperthermia.....	45
2.2.4.3.1	3D cell (spheroids) viability assay	46
2.2.4.3.2	3D cell (spheroids) cellular uptake assay.....	47
2.2.4.3.3	3D cell (spheroids) live/dead staining assay	47

3	Result and discussion.....	48
3.1	Doxorubicin encapsulated thermosensitive liposomes (DOX-TSL): characterization and visualization.....	49
3.1.1	Physicochemical characterization of liposomes	49
3.1.2	Encapsulation efficiency (EE%)	50
3.1.3	Differential scanning calorimetry (DSC).....	51
3.1.4	Visualization of DOX-TSL.....	52
3.1.4.1	Atomic force microscopy (AFM)	52
3.1.4.2	Transmission electron microscopy (TEM)	53
3.1.5	Stability of DOX-TSL.....	54
3.1.5.1	Colloidal stability.....	54
3.1.5.2	Serum stability	55
3.1.6	Drug release assay.....	57
3.2	Cell culture experiments	58
3.2.1	Spheroid generation	58
3.2.2	Spheroids growth curve	61
3.2.3	Spheroids fusion experiment.....	63
3.2.4	3D cell viability assay.....	64
3.2.5	Live/dead stain assay	68
3.2.6	Cellular uptake assay	70
3.3	Characterization of multifunctional liposome (ICG-DOX-mTSL)	75
3.3.1	Physicochemical characterization of liposomes	75
3.3.2	Encapsulate efficiency (EE %)	76
3.3.3	Differential scanning calorimetry (DSC).....	78
3.3.4	Visualization of ICG-DOX-mTSL.....	78
4	Summary and outlook.....	81
5	Zusammenfassung und Ausblick	87
6	Appendix.....	93

6.1	References.....	94
6.2	Abbreviations.....	117
6.3	List of figures.....	119
6.4	List of tables.....	121
6.5	Publications and Presentations.....	122
6.6	Curriculum vitae	123

1. Introduction

1.1 Triple negative breast cancer

Breast cancer is the most frequent malignant cancer globally and the main cause of cancer death in woman [1]. From 2000 to 2018, the number of global diagnoses rapidly increased from 1.05 million to 2.09 million annually [2].

As a diverse disease, breast cancer manifests in several different types of histology, genetics, clinical behaviors and responses to treatment [3]. In order to improve clinical management and therapeutic strategies, these types of breast cancer were classified into different sub-groups according to the statuses of histology and hormone receptor expression in the early 2000s. These are the estrogen receptor (ER); the progesterone receptor (PR) and the human epidermal growth factor receptor 2 (HER2) [4, 5]. In October 2005, the triple negative breast cancer (TNBC), which is defined by the lack of the expression of ER, PR and HER2 was mentioned for the first time [5]. TNBCs are further subdivided into the basal-like and non-basal-like subtypes, with the majority of cases belonging to the basal-like subtype, which is characterized by a high expression of cytokine-5 (CK5), cytokine-14 (CK14), caveolin-1, carbonic anhydrase IX (CAIX), p63 and epidermal growth factor receptor (EGFR/HER1) [6].

TNBC accounts for 15% of all breast cancer cases and shows aggressive clinical behavior such as high invasiveness, distant metastasis, relapse and mortality [7]. Due to the absence of well-defined targets, the therapeutic strategy of TNBC is often limited, therefore, surgery with the combination of radiotherapy and chemotherapy are usually the first option [8, 9].

1.2 Doxorubicin (DOX)

1.2.1 History and structure of Doxorubicin

Doxorubicin (DOX, market name: Adriamycin) is one of the most potent antineoplastic chemotherapy drugs. It was isolated from the actinobacterium *Streptomyces peucetius var. caesius* in the 1960s and belongs to the nonselective class I anthracycline antibiotics [10, 11].

The DOX molecule ((7S,9S)-7-[(2R,4S,5S,6S)-4-Amino-5-hydroxy-6-methyloxan-2-yl]oxy-6,9,11-trihydroxy-9-(2-hydroxyacetyl)-4-methoxy-8,10-dihydro-7H-tetracene-5,12-dione) is composed by a tetrahydroxy-anthraquinone and a six-member dianosamine sugar with a glycosyl moiety, which represents the general structure of anthracycline antibiotics [12]. DOX molecular weight is 579.99 g/mol and it carries one positive charge at physiological pH.

Doxorubicin hydrochloride is the most common form used for therapy and research. It is a hygroscopic crystalline powder composed of orange-red thin needles. It has its absorption maxima at 233, 252, 288, 479, 495 and 529 nm in methanol due to the dihydroxyanthraquinone chromophore. The absorption can be varied by any changes to the chromophore, including, but not limited to, pH, binding ions, solvent type and ionic strength. It is observed that DOX shows orange to red color at pH 7, violet at pH 11, and blue at pH 13 [13, 14].

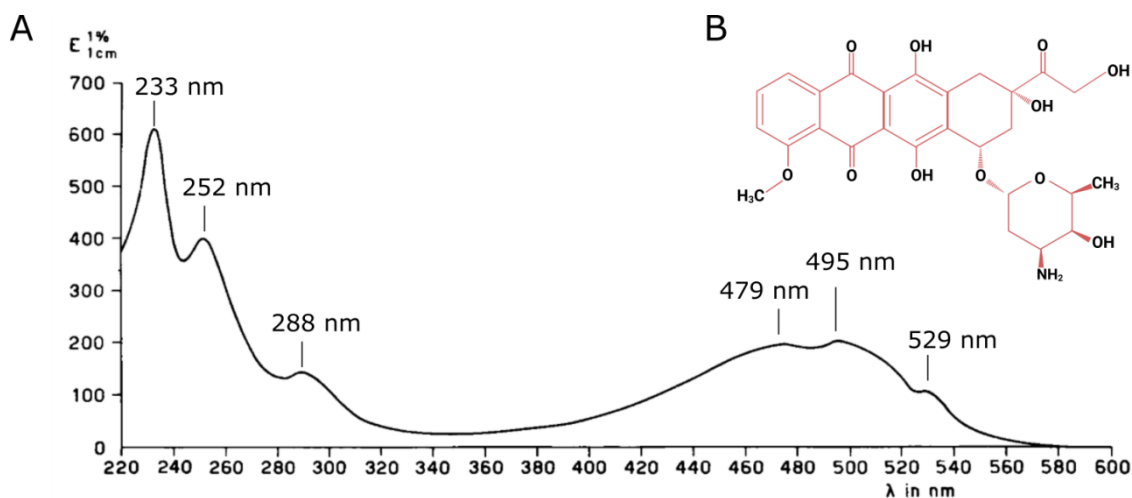


Figure 1: A: Ultraviolet and visible spectrum of Doxorubicin hydrochloride in methanol. The absorption maxima are at 233 nm, 252 nm, 288 nm, 479 nm, 495 nm and 529 nm, figure redrawn from ref. [15]. B: Chemical structure of doxorubicin (DOX) which is composed by a tetrahydroxy-anthraquinone and a six-member dianosamine sugar with a glycosyl moiety

1.2.2 Mechanism of activity

DOX enters the cancer cells by permeating the phospholipid bilayer membrane via passive diffusion [12]. In the cells, it unfolds its toxic effects through several independent mechanisms. One major source of cell death is based on the intercalation

of DOX into the DNA helices and its covalent binding to proteins involved in DNA replication and transcription, which leads to the inhibition of DNA, RNA and protein synthesis, resulting in cell death [16]. More specifically, after entering the cells, DOX binds with high affinity to the 20S subunit of the proteasome, thereby forming a DOX-proteasome complex that translocates into the nucleus through the nuclear pores. Due to its higher affinity for DNA it then dissociates from the proteasome and binds to the double helix [17]. This inhibits the enzyme topoisomerase II from re-ligating cleaved DNA double-strands which induces cell apoptosis [18, 19]. Moreover, it was found that DOX works not only in nuclear DNA but also in mitochondrial DNA (mtDNA), interfering with normal mitochondrial functions, protein expression and lipid oxidation [20, 21].

In mitochondria, DOX is able to bind to cardiolipin, an inner mitochondrial membrane-specific phospholipid and thus blocking the binding of mitochondrial creatine kinase (MtCK) to mitochondrial membranes [22]. Meanwhile, with the accumulation of DOX in the mitochondria, DOX redox cycling by complex I of the mitochondrial respiratory chain causes the increased generation of reactive oxygen species (ROS) [23]. Specifically, DOX is converted to semiquinone which generates ROS by reacting with molecule oxygen, thereby causing free radical formation and oxidative stress. Moreover, DOX can also hyperactivate the nuclear enzyme poly adenosine diphosphate (ADP) ribose polymerase (RARP-1), thus consuming the cells adenosine triphosphate (ATP) leading to cells autophagy [12, 24, 25].

1.2.3 Doxorubicin in cancer therapy

DOX is widely applied in treating various tumors because of its remarkable efficacy, for example in acute leukemia, lymphomas, lung cancer, testicular cancer, ovarian cancer, and is also considered as first-line chemotherapy drug for breast cancer. It is utilized for cancer therapy since the 1960s and the Food and Drug Administration approved DOX and acknowledged it as one of the most efficient chemotherapeutic agents [11, 26, 27].

However, as a small molecular drug (<1000 g/mol), DOX does not selectively affect only tumor cells. Instead, with the unfavorable pharmacokinetics and suboptimal bio-distribution, the toxicity of DOX also appears in unwanted places such as the lung, liver, brain, kidneys and especially the heart. The cardiotoxicity of DOX was first described in the end of 1969 and beginning of 1970s when DOX was widely used clinically. The heart shows high sensitivity of DOX mediated toxicity, with the accumulation of DOX on the heart, eventually culminating in irreversible congestive heart failure and death [28, 29]. Meanwhile, the DOX induced toxicity in the brain adds another set of unwanted side effects. The term “Chemobrain” emerged in order to describe the decline of cognitive functioning associated with chemotherapy. Other clinical manifestations such as anxiety, depression, fatigues show up frequently alongside the DOX application [30]. The damage in the brain stems from elevated level of tumor necrosis factor- α (TNF- α) in the blood, since DOX cannot pass through blood brain barrier (BBB) itself [31, 32]. Similar to other cancer drugs targeting proliferating cells, significant gastrointestinal toxicity with nausea, vomiting, diarrhea appear fast after DOX application. Stomatitis also occurs within 7-10 days [14]. Myelosuppression, leukopenia and thrombocytopenia also occurs and in severe cases lead to neutropenic fever and sepsis [33]. Because of this long list of severe side effects on healthy tissue, the conventional clinical application DOX is limited.

1.3 Liposomes

1.3.1 Definition and structure

Liposomes are closed spherical vesicles composed of lipid bilayer membranes, that were first created in the middle of 1960s by Dr. Alec D. Bangham [34]. Dr. Bangham described first that dry amphiphilic lipids can spontaneously arrange into hollow spheres in aqueous media via hydrophobic and hydrophilic interactions between lipids and water [35]. During rehydration, the thin layer of lipids forms closes and entraps water in the inner core. By this discovery, Dr. Bangham furthered the study to various fields for the upcoming researchers especially in drug delivery systems [36].

Liposomes are able to be industrially manufactured in different sizes and compositions according to the application.

The size of liposomes ranges from 20nm to 2500nm in diameter, with a thickness of the membrane of around 4nm [37]. Based on their size and number of membrane bilayers, liposomes are categorized as follows (Figure 2):

A) Unilamellar vesicles

- a) Small unilamellar vesicles (SUV) are less than 300 nm in diameter.
- b) Large unilamellar vesicles (LUV) are between 300 and 1000 nm in diameter.
- c) Giant unilamellar vesicles (GUV) are greater than 1000 nm in diameters.

B) Multilamellar vesicles

- a) Oligolamellar vesicles (OLV) have 2-5 concentric bilayers.
- b) Multilamellar vesicles (MLV) comprised of more than 5 concentric bilayers.
- c) Multivesicular vesicles (MVV) encapsulate multiple non-concentric bilayer liposomes.

liposomes.

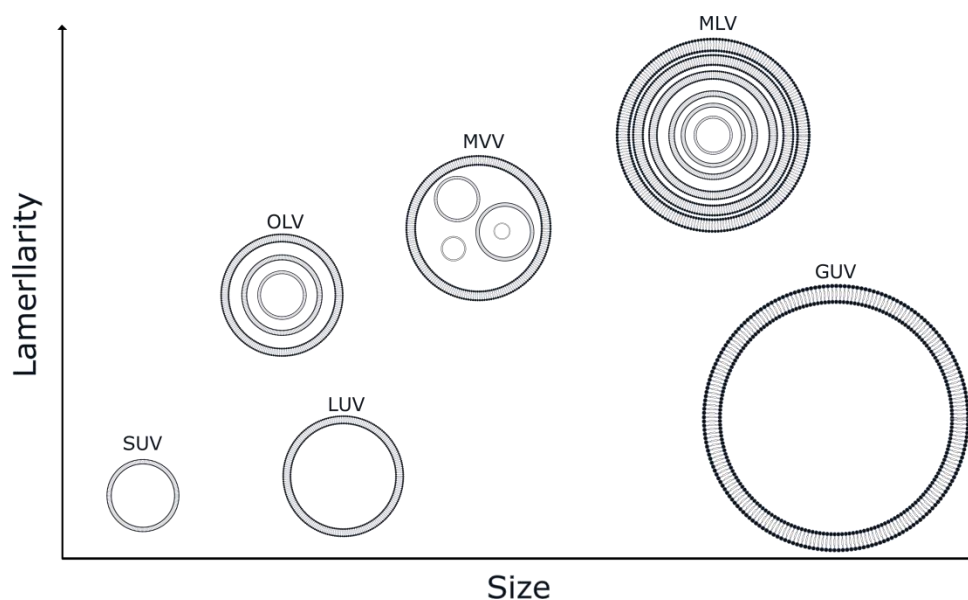


Figure 2: Classification of vesicle size and lamellarity. Small unilamellar vesicles (SUV) are less than 100 nm in diameter, large unilamellar vesicles (LUV) are between 100 and 1000 nm, and giant unilamellar vesicles (GUV) are larger than 1 μm . Oligolamellar vesicles (OLV) are comprised of two to five concentric bilayers. Multilamellar vesicles (MLV) contain more than five concentric bilayers. Multivesicular vesicles (MVV) contain non-concentric bilayer liposomes.

SUVs are the most utilized liposomes since they can be employed in many kinds of human tissues which have nanometric interstices. Thus the liposomes can accumulate and be taken up by cells.

Liposomes are predominantly made from amphiphilic phospholipids, which have both hydrophilic and hydrophobic groups. The hydrophilic part tends to be in contact with the surrounding water, whereas the hydrophobic part hides in the interior of the structure. This structure allows the phospholipids to form bilayer spherical vesicles with aqueous core and provide the capability of entrapping both hydrophilic reagents in the aqueous core and hydrophobic reagents in the liposomal membrane [38].

In clinical utilization, the liposomes are famous as drug delivery systems by their capacity of encapsulating and transporting the therapeutic agent in a non-toxic, biodegradable and stealthy way; meanwhile protecting the therapeutic compounds from cellular and tissue uptake [39]. This minimizes the side effect of the cytotoxic agents as long as the liposomes stay intact.

By decorating the liposome's surface with various materials their physiological behavior can be greatly varied. Based on their decoration liposomes can be categorized into four main types (Figure 3):

- A) Conventional liposomes that have no additional decoration on top of their phospholipid membranes.
- B) PEGylated liposomes that are covered with polyethylene glycol (PEG) which leads to increased half-life under physiological conditions.
- C) Ligand targeted liposomes that are decorated with target binding materials such as antibodies, aptamers and binding protein to enhance the selective drug delivery to the certain organs or tissues.
- D) Multifunctional liposomes that combine several of the aforementioned characteristics.

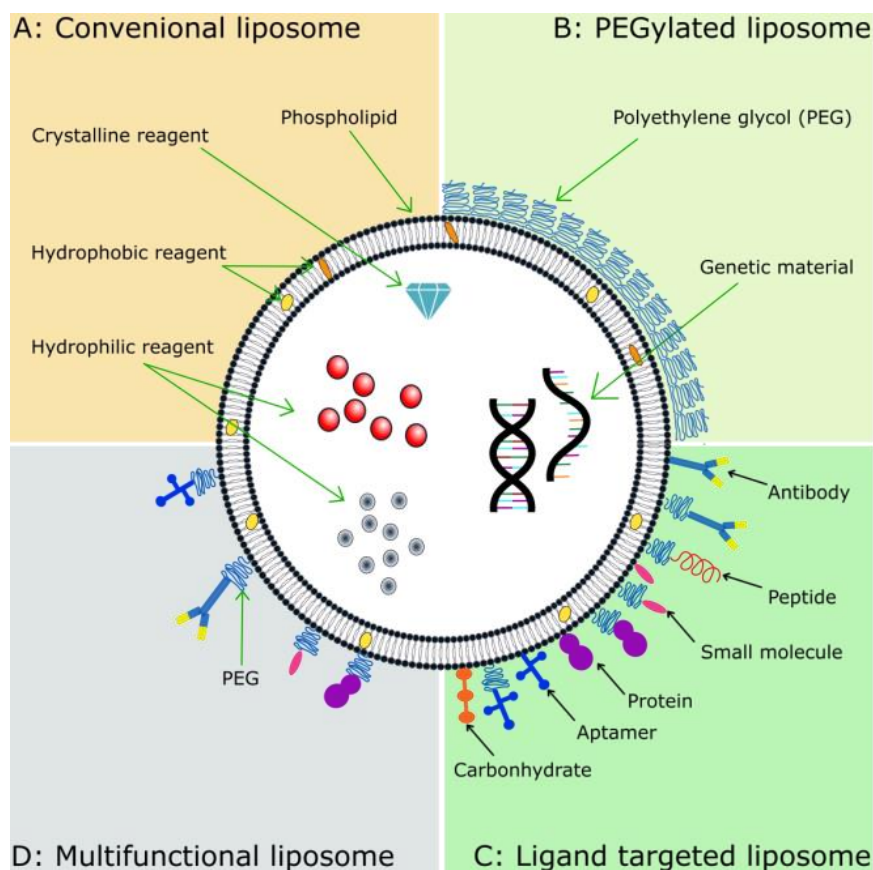


Figure 3: Overview of liposome structure classification. A) Conventional liposomes that have no additional decoration on top of their phospholipid membranes. B) PEGylated liposomes that are covered with polyethylene glycol (PEG) which leads to increased half-life under physiological conditions. C) Ligand targeted liposomes that are decorated with target binding materials such as antibodies, aptamers and binding protein to enhance the selective drug delivery to the certain organs or tissues. D) Multifunctional liposomes that combine several of the characteristics mentioned before.

1.3.2 PEGylated liposomes

Polyethylene glycol (PEG) is a hydrophilic polymer with a formula of $\text{HO}(\text{CH}_2\text{-CH}_2\text{-O})_n$ that is widely used in biomedical applications due to its biocompatibility, high solubility in aqueous and organic media, low toxicity and good excretion kinetics [40]. In drug delivery systems, PEG polymers are suitable to cover a carrier from immune system detection and thereby increasing its half-life. PEG can form in a thick and dynamic hydration shell on the surface of liposome due to its hydrophilicity and flexibility, which provides steric hindrance to protect the liposomes from protein corona formation and clearance by RES [41, 42]. The PEGylated liposomes can remain in blood circulation up to 7 days [33].

1.3.3 Lipid

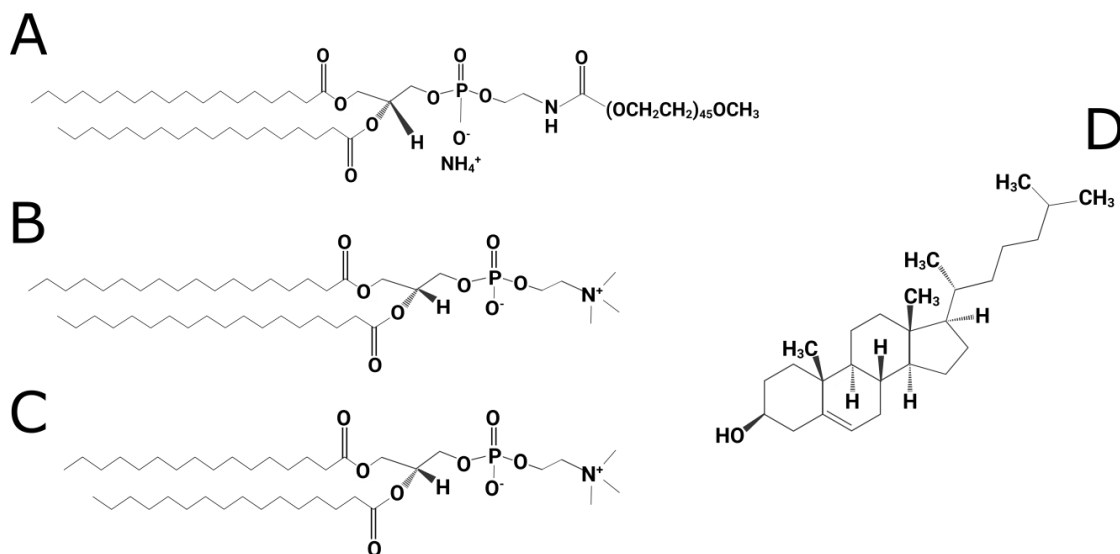


Figure 4: Chemical structure of the lipids used in liposomal formulations. A: DSPE-mPEG-2000; B: DSPC; C: DPPC; D: Cholesterol.

1.3.4.1 DPPC and DSPC

DPPC (1,2-Dipalmitoyl-sn-glycero-3-phosphocholine) is a phospholipid with a polar phosphate head group and a nonpolar fatty acid chain (Figure 4C). The molecular weight is 734.039 g/mol and it has a phase transition temperature of 41 °C. DPPC can form spherical vesicles due to its polar and non-polar interactions [43].

DPPC is the most commonly used lipid in liposomal formulations especially TSLs, in part because its T_m lies at physiological fever range. However, DPPC liposome alone would be very leaky at the body temperature. To reduce the premature leakage of the encapsulated drug, DPPC is often combined with a small amount of other lipids, for example DSPC (1,2-Distearoyl-sn-glycero-3-phosphocholine) (Figure 4B) which has a T_m of 55 °C and molecular weight of 790.145 g/mol. DSPC is a phosphatidylcholine with alkyl chains comprising 18 carbons, it is also an amphipathic lipid as DPPC [55, 56].

1.3.4.2 DSPE-mPEG-2000

DSPE-mPEG-2000(1,2-Distearoyl-sn-glycerol-3-phosphoethanolamine-N-[methoxy(polyethyleneglycol)-2000] ammonium salt) (Figure 4A) is a modified lipid that is

commonly added into liposomal formulations to provide the steric coating and improved half-life as discussed in section PEGylated liposomes.

1.3.4.3 Cholesterol

Cholesterol is a hydrophobic steroid molecule with a single polar hydroxyl group that naturally exists in the blood (Figure 4D). In 1995, Gaber *et al.* found that in combination with small amounts of cholesterol, the liposomal lipid bilayer is strengthened and stabilized. Cholesterol prevents vesicle aggregation and effects the T_m of the liposomes by making the phospholipid bilayer thicker and less permeable [44].

1.3.4 Doxorubicin remote loading

One of the most important considerations of the pharmaceutical application of liposomes is the efficiency and stability of loading drugs and/or other bioactive agents [46]. Four main strategies for efficient drug loading are driven by the use of pH-, sulfate-, manganese- or citrate-gradients. The ammonium sulfate loading method for DOX, that was used in this work, was first described Bahrenholz [46]. Drug loading according to this method, is facilitated by pH- and sulfate-gradients between the inside and the outside of the liposomes (Figure 5). The gradient is achieved by forming the liposomes in ammonium sulfate solution (pH 5.4) and later diluting the outside medium with PBS buffer (pH 7.4) and DOX. Ammonium sulfate has a low permeability coefficient so that the liposomes retain the gradient having $[(\text{NH}_4)_2\text{SO}_4]_{\text{inside}} \gg [(\text{NH}_4)_2\text{SO}_4]_{\text{outside}}$. The doxorubicin hydrochloride (DOX-NH₃Cl) in PBS dissociates into H⁺, Cl⁻ and deprotonated DOX-NH complex (DOX-NH₂). The now amphipathic DOX-NH₂ can diffuse into the aqueous core. In the acidic environment inside the liposomes, DOX-NH₂ gets protonated to DOX-NH₃⁺. In the presence of SO₄²⁻, the gel-like precipitate (DOX-NH₃)₂SO₄ is formed. Meanwhile the high permeability of NH₃ brings high efflux of the ammonia and drives more influx of DOX-NH₂. The (DOX-NH₃)₂SO₄ has low solubility in aqueous media, precipitates and prevents the re-permeation out of the liposomes.

The remote loading method is applicable for various amphipathic weak base drugs. It is fast, effective and not affected by the lipid composition and preparation method of liposomes. By this method drug encapsulated liposomes remain stable at the storage condition up to two years [47].

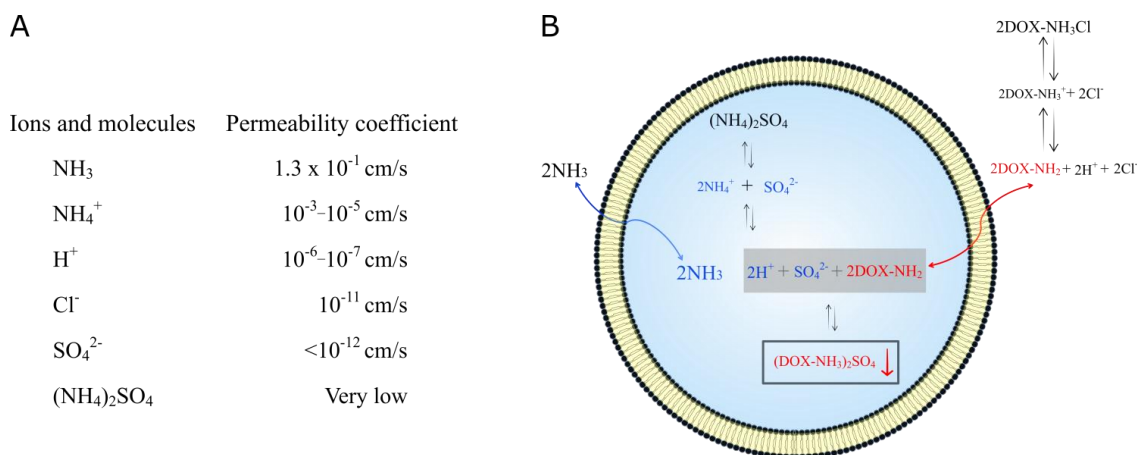


Figure 5: Schematic illustration of the doxorubicin remote loading by using trans-membrane ammonium sulfate gradient: A: The permeability coefficients (P) of the relevant ions and molecules in ammonium sulfate remote loading reaction [46]. B: The deprotonated DOX-NH₂ crosses the liposomal membrane from outside. Inside the liposome, it reacts with H⁺ and SO₄²⁻, and form (DOX-NH₃)₂SO₄ which precipitate and encapsulated inside the liposome. The NH₃ crosses the membrane.

1.3.5 Thermosensitive liposomes and triggered release

Thermosensitive liposomes (TSLs) are targeted drug delivery systems that release the encapsulated drug when heated to fever temperature (40–42 °C). By applying hyperthermia at the target region, TSLs can precisely release the drug by reaching the phase transition temperature (T_m) of the formulation [22–26]. Here the T_m represents the required temperature that the liposomes transfer from liquid condensed phase to the liquid expanded phase. In 1978, the first thermosensitive liposomes were described by Yatvin *et al.* as to remain intact at physiological temperatures (~37 °C) and to release the encapsulated drug when the external hyperthermia was applied [48]. The exact T_m of TSLs varies depending on many conditions, such as lipid composition, encapsulated components, size of the TSLs, and the presence of serum components. Further research confirmed that the drug cellular uptake is higher and the tumor growth is slower compared with classic free drug application [49].

Others stimuli-responsive liposomes for example temperature-, pH-, light- and ultrasound- sensitive liposomes also exist [50].

1.3.6 Thermotropic behavior of the phospholipid bilayer

The essential principle of drug release from TSLs is the phase transition of lipid membranes. When the temperature reaches the T_m , the lipid membranes transfer from liquid condensed phase (gel-phase, L_β) to liquid expanded phase (liquid-phase, L_α) (Figure 6).

In the liquid condensed phase, liposomes' phospholipid bilayer forms stable and compact structures with a minimum mobility of the fatty acid chains. In liquid expanded phase, the lipid membrane shows higher permeability and allows the encapsulated drugs to be released from the liposomes. [38].

Above the T_m , the phospholipid bilayer can transfer to the gel-liquid transition phase, which can be detected by differential scanning calorimetry (DSC), which is one of the most main method that measure endothermic and exothermic responses within a material [51]. The liquid expanded phase is characterized by the fatty acid chains changing their configuration from all-trans to all-gauche, which leads to the spatial structure becoming less compact.

The T_m of different lipids depends on the their chemical characteristics, such as the length of their hydrocarbon chain, degree of saturation of the fatty acid, the nature of the polar head, and the surrounding medium. It is related positively with the length of the hydrocarbon chains and negatively with the unsaturation of the fatty acids. For saturated lipids with long fatty acid chains, the polar heads of lipid starts changing the distance between each other at a specific temperature, which is named the pre-transition temperature.

When the pre-transition temperature is reached, the phospholipid configuration and membrane curvature simultaneously change and bring periodic ripples of the lipid bilayer which is called ripple phase. Acyl chains between C10 and C13 pass directly

through a gel-liquid transition without the ripple phase [51, 52]

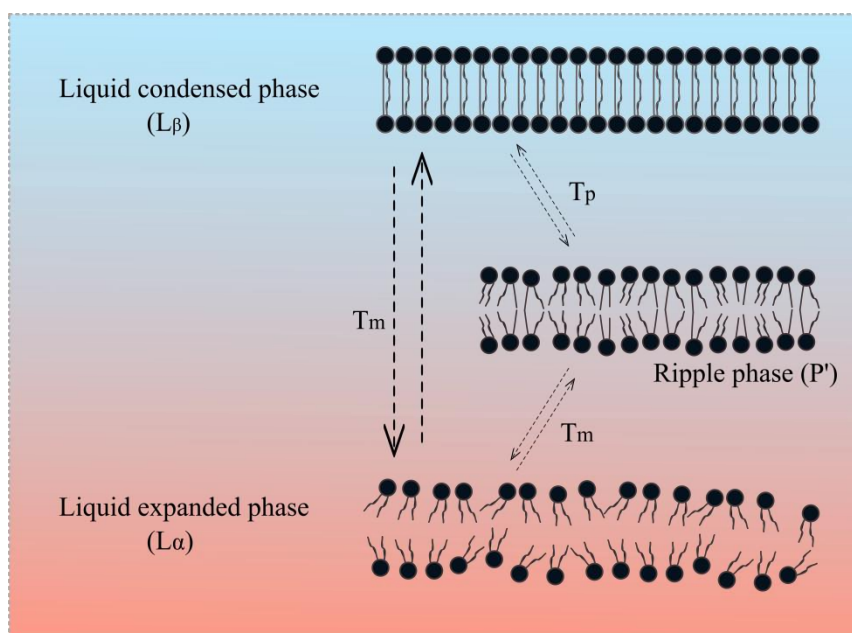


Figure 6: Schematic representation of the phase transition behavior of TSL. When the lipid membrane is heated above the transition temperature, the bilayer permeability increases, while below that temperature, lipid membranes exist in solid-phase only and therefore no drug release is expected.

1.4 EPR effect

Most nanoscale cancer medicines are intravenously applied and transported to tumors. The main method of liposomal formulation targeting is using the enhanced permeability and retention (EPR) effect to infiltrate the tumor site. This preferential tumor accumulation of the nano-carriers relies on the inflammation characteristics of tumor tissue, which enhances the extravasation and retention of the nano-carriers at pathological sites [53]. Most of the solid tumors have chaotic vasculature and tumor microenvironment. This consists in general of the high level of vascular growth factors and vascular permeability enhancing factors, the lack of functional lymphatic drainage, the elevated interstitial fluid pressure and deregulated stromal compartment such as fibroblasts, smooth muscle cells and macrophages [54]. The angiogenesis on the inflamed tumor tissue shows pathological changes in the blood vessels, the endothelial line of the new blood vessels. These allow the liposome extravasation, whereas healthy vessels cannot be penetrated through the compact and continuously endothelial lining. This means that due to the pathological changes in the ongoing

angiogenesis, the solid tumor endothelial lining of blood vessels is more permeable than in healthy tissue. Additionally the usual lack of lymphatic drainage supports the accumulation of the liposomes at the tumor site as shown in the Figure 7 [55,56].

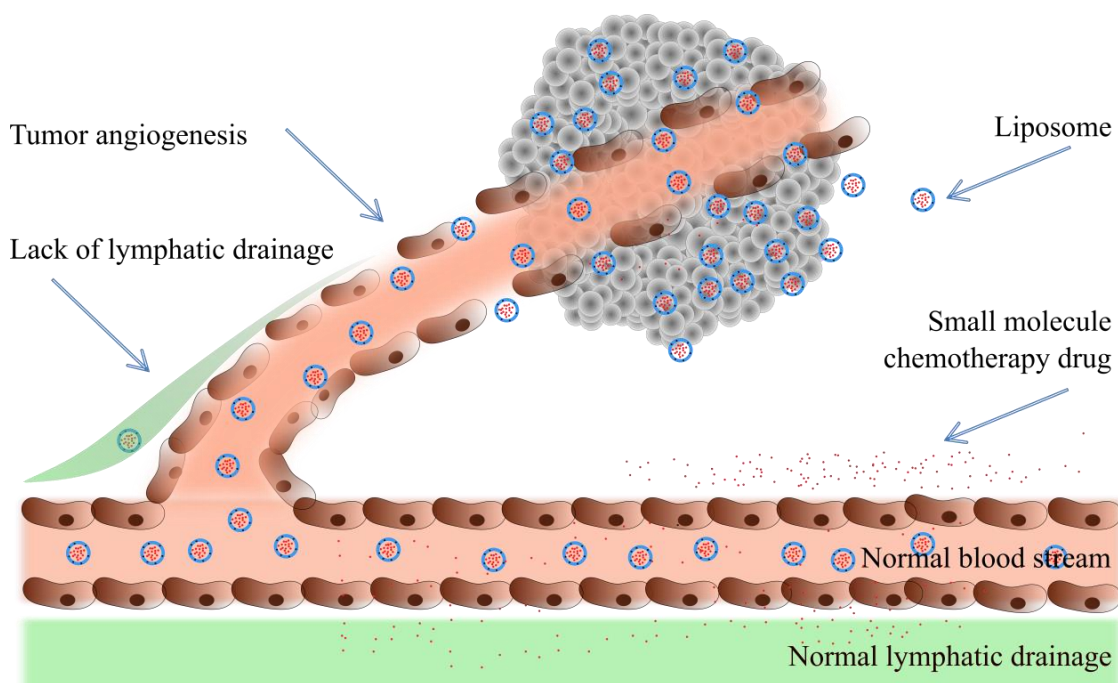


Figure 7: Schematic representation of tumor targeting via enhanced permeability and retention (EPR) effect. Liposomes injected into the blood stream can passively target the tumor with the tumor angiogenesis and the lack of lymphatic drainage which provide high permeability of liposomes to tumor site and low lymphatic clearance. Contrary, conventional small molecule chemotherapeutic drug show high off-target accumulation in healthy tissues and low accumulation at tumor site.

Due to this phenomenon, nano-scale drug carriers like liposomes have a wider path to enter the tumor site.

The gap size of the discontinuous vessels defines the optimal size of the nanocarrier is normally below 200 nm [57]. For this reason usually liposomes with an average size of 50 -150 nm diameter are selected as the drug delivery systems [53]. However, this accumulation takes about 1-2 days and the accumulated drugs are not available while they are still encapsulated inside the liposomes [50].

When the liposomes are intravenously injected, they go through three distinct stages, called circulation stage, extracellular matrix diffusion stage and cellular uptake stage. However, not all the liposomes can reach the cellular uptake stage, since many would be taken up by the reticuloendothelial system (RES) instead. The RES, also known as

mononuclear phagocyte system (MPS), is a part of the immune system with phagocytic cells in reticular connective tissue. The Kupffer cells of the liver and histiocytes can detect liposomes as foreign substances and then degrade and eliminate them. During the circulation stage liposomes can be adsorbed with some serum proteins in the blood stream. These proteins can form a protein corona on the surface of the liposomes, thereby act as opsonins and initiate phagocytosis, which leads to the clearance of the liposomes [58, 59]. In order to prolong the half-life of the liposomes, the surface can be PEGylated which prevents opsonization and fast clearance by the RES [60]. The prolonged circulation time is decisive for the accumulation in the tumor tissue via EPR. However, the absolute accumulation depends on the blood/tissue distribution coefficient.

1.5 Hyperthermia in cancer therapy

Hyperthermia in therapeutic setting refers to the artificial increase of tissue temperature via various methods. First reports of Hyperthermia treatment for various solid tumors reach as far back as ancient Egypt, specifically to Edwin Smith's Surgical Papyrus, which was dated to have originated between 3000 BC - 2500 BC. One document describe the practice of using so-called "fire-drill", which a stick that was rapidly rotated by hand and pressed against breast tumor tissue. It can be seen as the first reported ablation [61, 62].

In difference to fever, therapeutic hyperthermia can be controlled very precisely and utilized both internally or externally, regionally or systemically. The application of hyperthermia does not change the body's set point temperature [63].

Regional hyperthermia can be obtained by applying photon radiation at radiofrequency, microwave or ultrasound, which enables a high degree of control of the thermal dose application [64]. Radiofrequency waves at 0.3-30 MHz with the inserted electrodes in tumor that expel an alternating electrical current with agitates the ions in tissue, resulting the heat generation by friction [65, 66]. Microwaves generate heat by the same energy as radiofrequency but at a higher range of

frequencies (915-2450 MHz). When the frequencies was applied, the already placed antennas in the tumor induce the vibrations in the water molecules in tissues, and subsequently covert to heat [67, 68]. Ultrasound for clinical thermal application was first reported in 1940s and the high intensity focused ultrasound (HIFU) was widely researched in 1990s. Ultrasound waves at 0.5-3.5 MHz produce compression and rarefaction pressures on the target tissue medium, thus elevate the local tmeperature [69, 70].

Furthermore, nanotechnology has been introduced into the biomedical applications and has shown promising pre-clinical and clinical results [71]. The stimuli-responsive nanomaterials absorb energy from the external light or magnetic fields to enhance the effect of hyperthermia. Moreover, nanomaterials reverse the direction of heat loss. They focus the energy form the external source on the tumor site and generate the heat for localized thermal destruction, meanwhile reduce the adverse effect on the healthy neighbor tissues [71, 72].

Magnetic hyperthermia usually uses superparamagnetic nanoparticles that are stimulated by an alternating magnetic field, thus generate heat with the rapid changes on the nanoparticles polarity [73]. Heat can be also achieved by laser light in treatment, which is known as photothermal therapy (PTT). In laser hyperthermia, near-infrared (NIR) (780 nm-1350 nm) and visible light (380 nm-780 nm) are common used as the external source providing the light energy for the nanomaterials and thermal nanomaterials can absorb light to convert it into heat energy.

The thermal therapy covers a large range of temperature. It is mainly divided into two catalogs, hyperthermia and thermal ablation (Figure 8).

The temperature of hyperthermia is defined between 40 to 45 °C, and consists of mild hyperthermia (40-42 °C) and moderate hyperthermia (42-45 °C). Hyperthermia in this temperature range is used to activate or enhance the radiotherapeutic and/or chemotherapeutic effect in clinic whereas not efficacious as a monotherapy.

In vascularized tumors, the increase of blood perfusion occurs after 30-60 minutes in

mild hyperthermia. It facilitates the increase of drug accumulation and chemo-sensitization whereas no direct cytotoxicity occurs. In moderate hyperthermia, the irregular tumor vascular stasis was observed. Subsequently, hypoxia and acidosis appear. With moderate hyperthermia for 30-60 minutes, the inhibition of DNA repairs and cell apoptosis are induced. It leads to DNA damage and provide the sensitization of radiotherapy and chemotherapy.

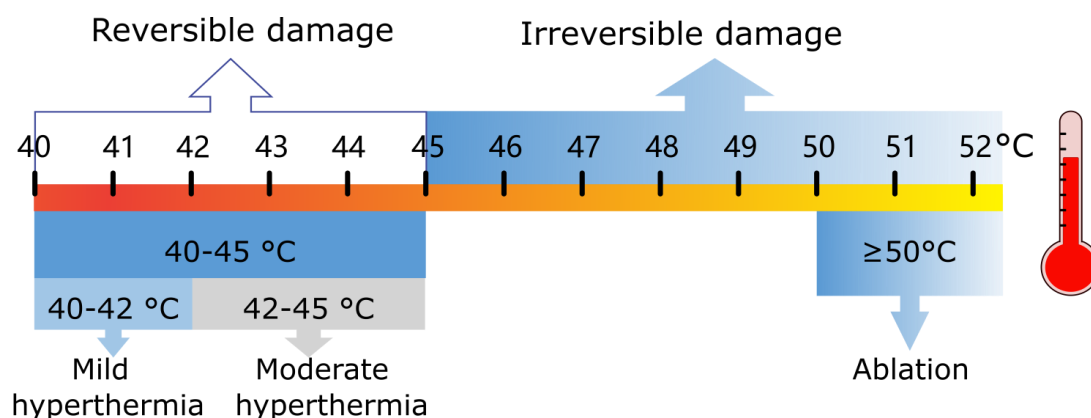


Figure 8: Temperature range of thermal treatment in cancer therapy. At mild hyperthermia (40-42 °C) and moderate hyperthermia (42-45 °C), the heat is utilized to active or enhance the radiotherapeutic and/or chemotherapeutic effects due to the increase of blood perfusion. Temperature below 42 °C does not bring any cell damage, while below 45 °C the damages of the tumor tissue is reversible. Thus hyperthermia below 45 °C is not efficacious as monotherapy. When temperature rises over 45 °C, the irreversible damage of the tumor tissue occurs and resulting cell necrosis. In order to ablate the tumor tissue efficiently, the higher temperature (≥ 50 °C) is usually employed.

When coming to the temperature over 45 °C, the irreversible damage occurs on tumor tissue and leads to cell necrosis over 30 minutes of heat. Additionally, strong vessel stasis induced hypoxia can trigger angiogenic response inducing angiogenesis, and thereby may increase the blood perfusion to the tumor and potentially facilitate the tumor growth. Besides, the remodeling of tumor extracellular matrix (ECM) relieve the pressure on tumor vessels therefore enhances the blood perfusion [74, 75]. Since the aim of thermal ablation is direct cell death via necrosis as monotherapy, the higher temperature is usually considered (≥ 50 °C). However, the risk of healthy tissue damage also occurs [76].

Blood supply is essential for tumors as it provides oxygen and nutrients and takes away the metabolic waste from the tumor. Additionally, it plays an important role in the distant metastasis. Thus the angiogenesis is decisive for tumor growth and expansion [77]. Since the angiogenesis rate is much higher than the normal physiological level, the new vessels are more permeable and less efficient at thermoregulation than healthy vessels [78]. This explains that the cancer cells are more sensitive to heat [79]. Due to the thermal sensitivity, the vascular stasis in tumors is induced at a lower temperature as compare to the healthy tissue. It is reported that at 42 °C for 30 minutes, the vessel stasis is induced efficiently in most cancer models, whereas in healthy tissue the temperature of 45 °C is required for the same effect [80]. In rabbit tumors, vascular stasis occurs after 60 minutes hyperthermia at 41-42 °C. While in healthy rabbit, taking the same time to achieve the same effect, the temperature of 47 °C is needed [81].

Moreover, a slightly high temperature (approximately 40 °C) can increase the blood perfusion in tumor. This increases the sensitivity to radiation and enables a larger concentration of drug to the tumor site. In radiotherapy, it is reported that the cervical cancer responds significantly well to the combination of mild hyperthermia (40 °C for one hour) and radiation [82].

Mild hyperthermia is widely used to target delivery and trigger release of the drug from thermosensitive carriers in drug delivery systems (DDS). Mild hyperthermia causes major increase in tumor perfusion and facilitates the accumulation of the drug carriers in the target site via EPR effect. Subsequently, mild hyperthermia triggers the drug release by reaching the T_m of the thermosensitive drug carriers [83]. Treatment at mild hyperthermia temperatures is toxic for cells in hypoxic and low pH environments, which are mostly found within solid tumor due to low blood perfusion. [83–85].

1.6 Indocyanine green (ICG)

1.6.1 History and structure

Indocyanine green (ICG, market name: Diagnogreen[®] or ICGreen[®]) is a nontoxic,

fluorescent, tricarbocyanine, near-infrared (NIR) dye. It was firstly developed for near-infrared photography by Kodak research laboratories and was later approved by the FDA for clinical application in the 1950s, including evaluation of cardiac output and hepatic function in patients. [86]. In 1970s, ICG was found to have a strong absorption in the near-infrared (NIR) spectra, making it suitable for bio-imaging applications [87]. NIR light carries a large penetration depth in tissue due to the long wavelength [88]. The radiation can be absorbed in the tissue by water, hemoglobin and melanin. However, the NIR light is weakly absorbed by these endogenous biomolecules and intracellular organelles [89]. Therefore, the NIR light can penetrate in deep target area without damaging the surrounding tissue [90]. Due to this phototherapeutic capability with NIR irradiation, ICG has attracted enormous attention in biomedical field.

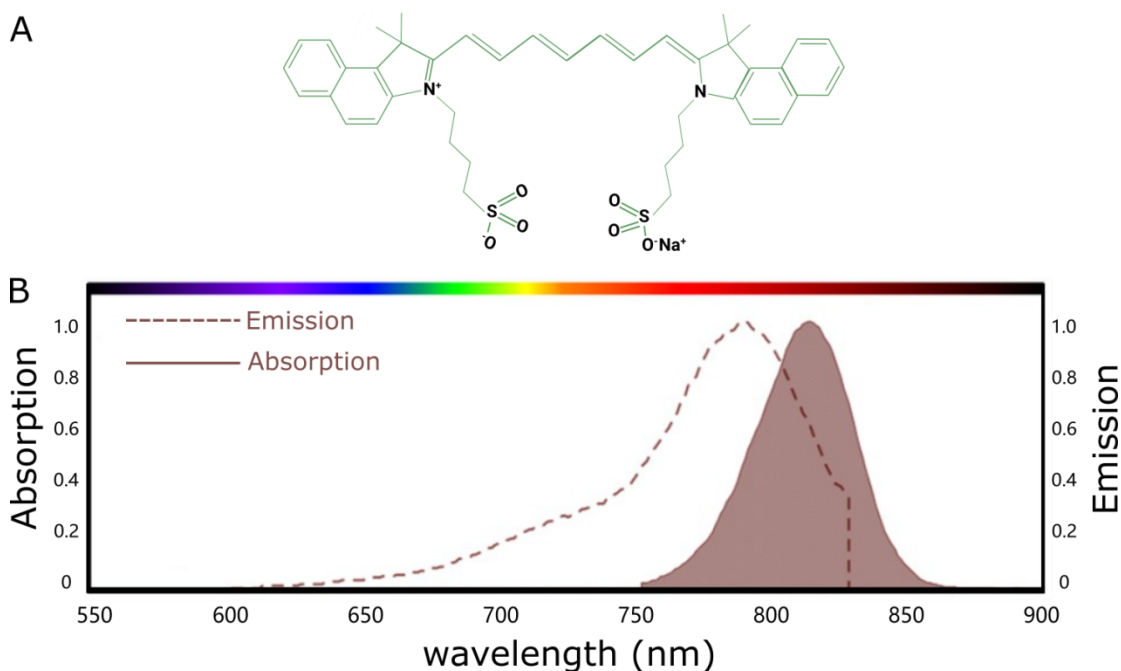


Figure 9: A: Chemical structure of Indocyanine Green (ICG) which is composed by a lipophilic polyaromatic polyene group and a hydrophilic sulfonate group. B: The absorption and emission fluorescence spectra of Indocyanine Green (ICG). (Spectrum courtesy of AAT Bioquest, Inc.)

ICG molecule (sodium 4-[(2Z)-2-[(2E,4E,6E)-7-[1,1-dimethyl-3-(4-sulfonatobutyl)benzo[e]indol-3-ium-2-yl]hepta-2,4,6-trienylidene]-1,1-dimethylbenzo[e]indol-3-yl]butane-1-sulfonate) is amphiphilic which contains a lipophilic polyaromatic polyene

group and a hydrophilic sulfonate group (Figure 9A). It is a zwitterion with a molecular weight of 774.96 g/mol and with negative charge [91].

It has an absorption maximum of 810 nm under most physiological conditions and in cell culture, and an emission wavelength of 760 nm [92, 93] (Figure 9B).

1.6.2 ICG in photodynamic therapy

Photodynamic therapy (PDT) was demonstrated in the beginning of the 20 century by Niels Ryberg Finsen winning of the Nobel Prize in Physiology/Medicine. He discovered the potential of treating different diseases using light alone or with chemicals [94]. PDT relies on three individual factor: photosensitizer, light and molecular oxygen [95]. Photosensitizer is a structure that transfer light energy through the photodynamic reaction. ICG as a photosensitizer can be excited by laser light at the wavelength of 808 nm [89]. The long wavelength is assumed to be capable of penetrating deeper into the tissue to treat more in-depth cancerous cells due to the lower absorption and scattering [88].

When the laser activate ICG, the ICG molecules are transferred from the ground state to and excited singlet state and then to a triplet excited state via the intersystem crossing [95]. In triplet excited state, ICG loses its energy in two ways (Figure 10):

A) Electron transfer reactions (Type I). In this reaction, ICG directly interacts with cell components forming anionic or cationic radicals that interact with molecular oxygen generating reactive oxygen species (ROS), such as singlet oxygen and superoxide, under the irradiation, which damage the cells [96–98].

B) Energy transfer reactions (Type II). ICG interacts with molecular oxygen producing the singlet oxygen ($^1\text{O}_2$), which is able to ablate tumors, bacteria fungus and viruses [99, 100].

The generated ROS, including $^1\text{O}_2$, H_2O_2 , O_2 , OH , induce cell apoptosis and/or necrosis though the irreversibly oxidation of the cellular and subcellular organelles and eventually lead to cell death [101]. Moreover, ROS can also induce autophagy lead to cytoprotective and cell killing responses [102].

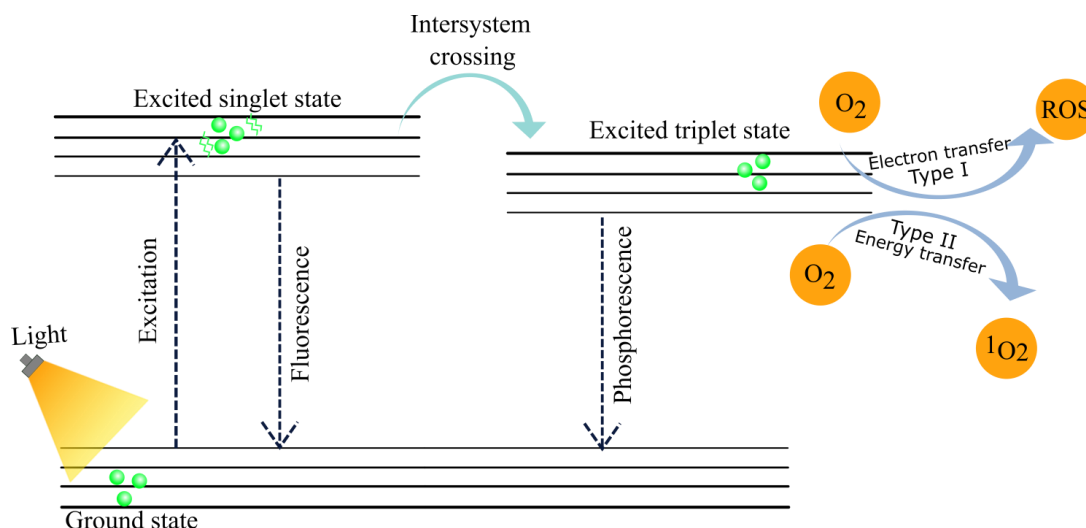


Figure 10: Representation of photodynamic therapy (PDT) mechanism of Type I and Type II reactions. Photosensitizer (in this case indocyanine green (ICG)) is activated by light (in this case NIR at 808nm), excited to singlet state and then to triplet excited state via intersystem crossing. In excited triplet state, by the electron transfer (Type I), the cytotoxic reactive oxygen species (ROS) are formed. In Type II, through energy transfer the singlet oxygen occurs.

1.6.3 ICG in photothermal therapy

Photothermal therapy (PTT) is a light-mediated therapeutic technique that is seen as one of the most promising therapies for oncology. It was first took place by Professor Manfred Baron von Ardenne in 1960s. He developed a systemic cancer multi-step therapy that the cancer and metastases are treated with glucose, oxygen and hyperthermia in combination with chemicals [103]. PTT transforms the photon's energy into heat at a target location thereby inducing necrosis with minimally invasive and side effects [104, 105]. To convert the absorbed light energy to cytotoxic heat, the photothermal agents, localized at the tumor site, can be triggered by electromagnetic radiation, such as near-infrared (NIR), visible light, radiofrequency or microwaves. This leads to the thermal ablation of the cells *i.e.* protein denaturation, cell membrane lysis and cytosol evaporation, which eventually leads to cell death [90]. The most common used irradiation source is NIR with the wavelength of 750-1350 nm. Since the cells and tissues barely absorb and scatter photons of this wavelength, NIR can penetrate into deeper tissue with less damage.

Unlike the photodynamic therapy (PDT), photothermal therapy (PTT) does not

require the present of oxygen in the tumor cells to generate cytotoxic effect, which increase the temperature in the target areas. Thus the PTT is more effective for the tumors in hypoxia condition.

Photothermal agents are the chemical substances that can trigger a photothermal effect in connection with exposure to light. They are characterized by their very high absorption of certain wavelengths of photons, which makes them suitable for heating target areas. There are inorganic and organic photothermal agents. The Prominent inorganic photothermal agents are gold-, silver- and other noble metal-based as well as more complex nanomaterials. They have been widely researched for cancer therapy due to the high photothermal conversion efficiency and tumor accumulation via EPR effects. However, the clinical application of these metallic nanomaterials remains limited due to issues with their long-term biosafety [105, 106].

In contrast, the organic photothermal agents including ICG have shown their advantages in stability, biocompatibility, and large molar absorption coefficient in NIR region. The most common mentioned downside of organic photothermal agents, especially cyanine dye, is the low solubility, photobleach and photodegradation in the serum. However, the small molecules like ICG can be encapsulated in nanoparticles such as liposomes to enhance their photostability. The mechanism by which ICG converts light energy into heat energy works through electron excitation and internal energy conversion. NIR radiation gets absorbed by the electrons in the ICG molecule which elevates them from their ground state energy into an excited state. In the excited state, the molecule gradually converts back to its lowest excited singlet state (S₁) via vibrational relaxation and internal conversion. The pathway back to the ground state leads through one of two competing mechanisms (Figure 11):

- A) Radiative transition in which a photon is emitted (fluorescence).
- B) Non-radiative transition in which the excitation energy is converted into several forms of kinetic energy (rotational energy, torsion energy, vibration) and therefore heat [106].

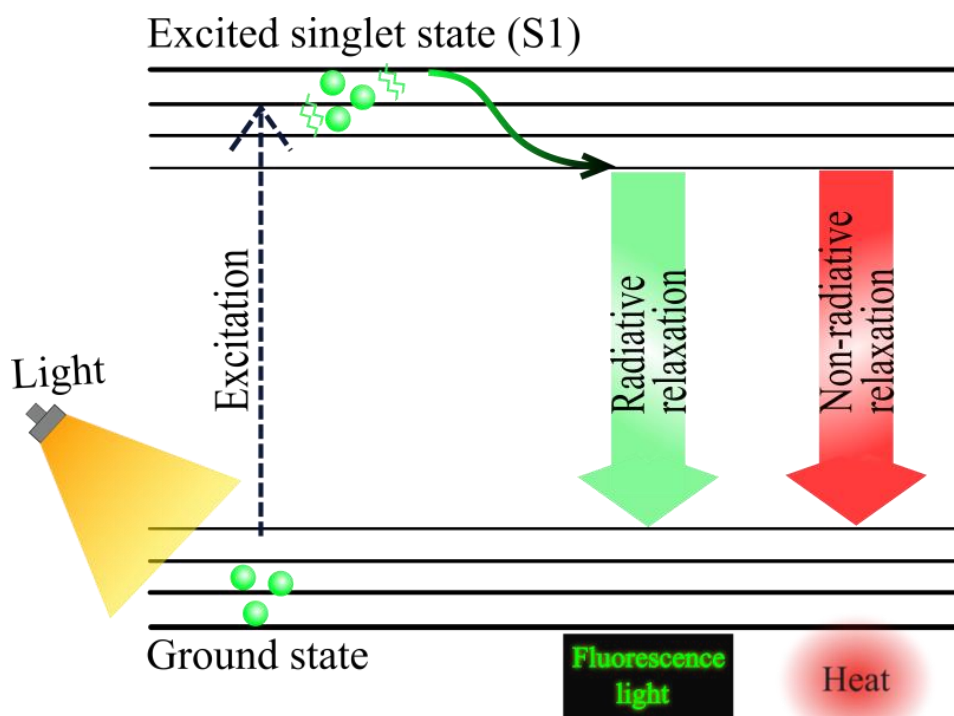


Figure 11: Mechanism of photothermal therapy (PTT). NIR radiation gets absorbed by the electrons in the photothermal agents (in this case indocyanine green (ICG)) molecule which elevates them from their ground state energy into an excited state. In the excited state, the molecule gradually converts back to its lowest excited singlet state (S1) via vibrational relaxation and internal conversion. The electrons then release energy and return to the ground state with either radiative relaxations (producing fluorescence light) or Non-radiative relaxation (generating heat).

1.6.4 Clinical usage of ICG

ICG has been applied as a fluorescence probe for clinical diagnose and therapeutic assistance. When injected intravenously, ICG binds with serum protein albumin and globulin, and can be rapidly distributed to the whole body through blood circulation. The most prominent use cases are angiography in ophthalmology, cerebrology and cardiology [107–109], monitoring circulatory function, liver function and splanchnic perfusion, as well as perfusion-related analysis of tissues and organs [92, 94–98]. Further use is made in sentinel lymph node biopsy and diagnosis of rheumatic diseases [112–117].

Moreover, ICG shows high levels of biosafety and stability in patients. When injected intravenously, ICG associates with plasma protein and does not leak from the blood circulation. From there it gets selectively taken up by the liver, and excreted to the

bile in its original form [92]. When injected extravascularly, ICG accumulates in the lymph, usually reaching the nearest draining lymph node within 15 minutes. After 1-2 hours it binds to the regional lymph nodes and deposits into macrophages [118].

The usual concentrations of ICG for different applications *in vivo* are in the range of 10–25 mg/mL for retinal and choroidal angiography, less than 2 mg/kg for cardiac output and blood volume monitoring and 0.5 mg/kg for hepatic functional observation, respectively [119]. None of them show any toxicity on patients. It is reported that with the high dose of 5 mg/kg is no toxicity was observed in human [92, 120].

1.6.5 Liposomal ICG formulation

Some of the clinical and diagnostic advantages of ICG are limiting factors for phototherapeutic applications. This includes especially its poor optical stability, weak photothermal capability and rapid hepatobiliary elimination as well as its plasma half-life of less than 5 minutes [121]. These challenges can be alleviated through nanoparticle drug delivery systems platform such as liposomes, which improve the blood retention and tumor delivery efficiency [87].

Liposomal ICG formulations can be produced comparatively simply through its mechanism of self-assembly in which the lipophilic part of the ICG molecule associates with the phospholipid bilayer whereas its hydrophilic part either in the aqueous core or on the surface of the liposome [105]. Multi-spectral optoacoustic tomography (MSOT) confirms the increased optical stability of liposomal ICG formulation *in vivo* [122].

Combining ICG with thermosensitive liposomes does not only increase its clinical viability under physiological conditions, but unlocks new options for targeted destruction of the TSLs in the body as well. In combination with anticancer drugs in TSLs, this opens up the possibility of targeted drug release inside the body [123, 124]. This targeted drug delivery can further be enhanced with functionalized liposomes, for example with antibodies, aptamers binding proteins and other legend targeting options [125, 126].

1.7 3D cell culture

1.7.1 Background and structure of 3D cell culture

3D cell culture encompasses all cell culturing techniques that let cells grow in a prominently three-dimensional environment, characterized by a domination of cell-cell contact over cell-surface contact [127]. This is believed to mimic biological conditions in actual organs and tissues closer than 2D cell culture. Because of this, it is used since the 1970s to study healthy and unhealthy tissues and organs *in vitro*, for example in the investigation of cell proliferation, apoptosis, differentiation, gene expression and metabolism in multicellular contexts [128]. In 1977, Hamburg and Salmon developed one of the earliest 3D cell culture models with the assistance of soft agar as extracellular matrix (ECM) [129].

One of the most utilized 3D cell culture methods is the generation of multicellular tumor spheroids (MCTS), which are able to self-assemble and to form compact micro-scale cellular aggregations.

Due to the absence of vessels, all medium components need to passively diffuse through the cell layers, where they form gradients, either from the outside to the inside (*i.e.* oxygen, nutrients, growth factors), or *vice versa* (*i.e.* CO₂, metabolic waste). This gets increasingly problematic with increasing size of the spheroids, especially at diameters over 400 μm . Spheroids typically form three distinct cell layers. From the outside to the center they are (Figure 12):

- A) Proliferation zone
- B) Quiescent zone
- C) Necrotic zone

The proliferation zone is characterized by high availability of oxygen and nutrients as well as low concentrations of metabolic waste. Here cells are able to divide and proliferate, which adds to the spheroids growth. In the quiescent zone cells are able to survive by decreasing their metabolic speed, however at increasing costs of their rate of proliferation. In contrast, the core of a spheroid becomes quickly depleted of

oxygen (hypoxia) and nutrients, which leads to the development of a necrotic zone, which is characterized by cell death and no proliferation activity. Furthermore, cancer cells under hypoxic conditions convert pyruvate to lactate in order to obtain energy according to the Warburg effect. The accumulated lactate causes the acidification of the interior of a spheroid (pH of 6.5-7.2) [130, 131].

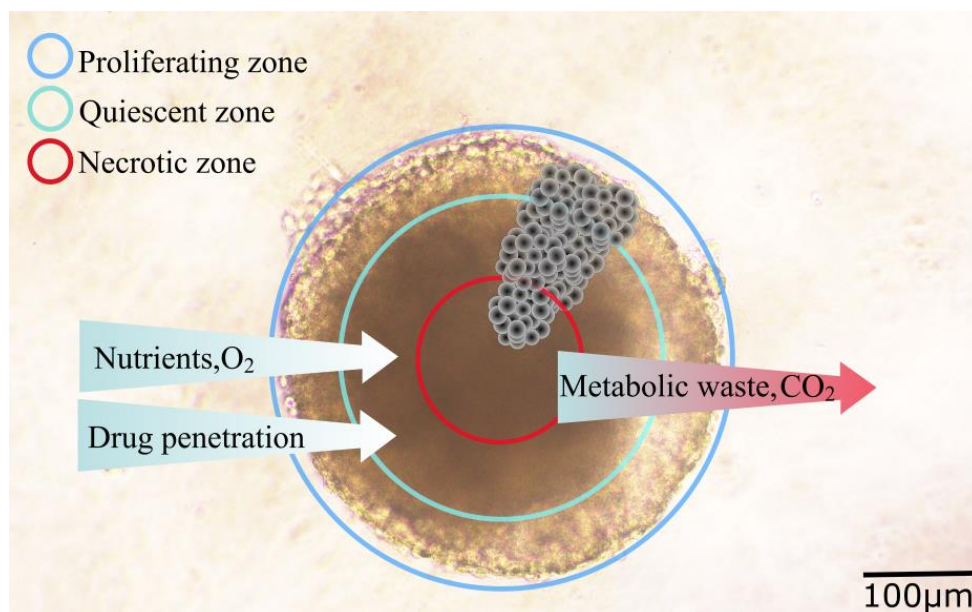


Figure 12: Schematic representation of spheroid structure. Big spheroid (over 400 μm diameter) is distinguished from outside to inside three sub-regions, i.e. Proliferating zone, quiescent zone and necrotic zone. Due to the passive diffusion of all medium components and metabolic wastes the inner cells tend to obtain less nutrients and retain more metabolic waste compare to the cells in the outer part of the spheroid. Spheroid was captured by fluorescence microscope at day 4 at seeding density of 5000 cells. The scale bar represents 100 μm .

1.7.2 Comparison of 2D and 3D cell culture

Despite the advantages of 3D cell cultures, most research is still performed using 2D cell cultures. This is due to easier handling, good reproducibility and established protocols to grow thousands of different cell lines, which leads to often times faster progress and cost effectiveness [95, 100]. However, 2D cell culture based cytotoxicity assays have shown many limitations due to the fact that cells in monolayer culture cannot mimic the morphological and interactional features of live tumor cells as they grow *in vivo* [133]. In the process of transferring tumor tissues into 2D conditions, their

cell morphology has changed and many essential characteristics of their phenotype are lost, which can interfere with several functions of the cells [102, 103]. These include cell-to-extracellular matrix (ECM) and cell-to-cell interactions [136]. This observation is used to explain the high rate of clinical trial failures in preclinical testing when core tests are performed on 2D cell cultures [105, 106]. For example many anti-cancer drugs that show high efficacy in 2D cell culture where ineffective against spheroids, due to the low permeability their cell layers, their hypoxic core and the presence of dormant, metabolic largely inactive cells [99, 107–109].

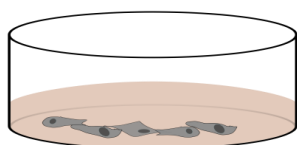
One of the main advantages of 3D cell culture is that tumor cells retain their general architecture and many morphological and physiological characteristics of their *in vivo* tumor counterparts [142]. The structure also maintains the biological and physiochemical features of solid tumor mass [102, 111]. Therefore, 3D cell culture is considered to be an improved model for the biological properties of micrometastases and vessel distal regions of tumors [144](Figure 13).

1.7.3 3D cell culture in modern drug development

Due to these advantages, 3D cell culture models are seen as a promising bridge to close the gap between conventional 2D *in vitro* testing and animal models [133], especially for high-throughput drug screening programs [143,145].

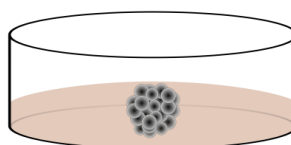
Spheroids are considered as the most suitable *in vitro* cell culture model for anticancer drug testing with the outstanding ability to display the *in vivo* solid tumor features like the cellular heterogeneity, cell to cell signaling, internal structure, ECM deposition, ECM-cell and cell-cell interactions, growth kinetics, gene expression and drug resistance [127]. For many cancer drug candidates 3D cell culture models allow for the performance of high throughput growth inhibition screening (HTS) [146].

2D Cell culture



- ✧ Monolayer growth
- ✧ Unnatural rapid proliferation
- ✧ Changed cell morphology and division
- ✧ Cell-to-cell interaction is limited
- ✧ All cells attach on the plate
- ✧ All cells have equal access to nutrients
- ✧ Metabolic waste gets disposed into the medium
- ✧ No drug diffusion gradient
- ✧ Gene and protein expression differs from *in vivo*
- ✧ No drug resistance
- ✧ Cheap, high reproducibility
- ✧ Quick cultivation
- ✧ More established analytic methods

3D Cell culture



- ✧ Multiple layer growth
- ✧ Natural proliferation
- ✧ Natural cell morphology and division
- ✧ Cell-to-cell interaction mimics *in vivo*
- ✧ Cells attach with extracellular matrix (ECM) and other cells only
- ✧ Cells access to nutrients depends on their location in the diffusion gradient
- ✧ Cells in the core cannot dispose waste efficiently
- ✧ Drug diffusion gradient mimics a physiological scenario
- ✧ Similar gene and protein expression levels to *in vivo*
- ✧ Some forms of drug resistance appear as *in vivo*
- ✧ More expensive, low reproducibility
- ✧ Time-consuming
- ✧ Fewer commercial available tests

Figure 13: Comparison of 2D cell culture and 3D cell culture

1.8 Aims and objectives

The purpose of this work is to develop a suitable liposomal drug delivery system for doxorubicin (DOX) and investigate the efficacy of the formulation on triple-negative breast cancer 3D cell culture models after controlled release. Furthermore, multifunctional liposomes are investigated. It is aim to combine phototherapy and chemotherapy by co-encapsulating indocyanine green (ICG) and DOX. The efficacy of multifunctional liposomes was assessed *in vitro*. The concrete implementation of this project is as follows:

- Prepare thermosensitive liposomes and encapsulate DOX via active remote loading method with the gradient of ammonium sulfate.
- Analyze the physicochemical characterization of thermosensitive liposome including the size, surface charge, drug loading efficiency, general stability and drug release.
- Investigate the morphological changes of thermosensitive liposomes under hyperthermia via AFM and TEM.
- Generate the multicellular tumor spheroids from triple-negative breast cancer cells under ultra-low attachment condition.
- Observe the spheroids growth curve under the microscope.
- Evaluate the cellular uptake and cytotoxicity of the DOX thermosensitive liposomes *in vitro* in multicellular tumor spheroids by CLSM and 3D cell viability assessment.
- Prepare thermosensitive liposomes encapsulated photothermal agent ICG for NIR triggered phototherapy.
- Analyze the physicochemical characterization of the ICG liposomes.
- Encapsulate DOX to ICG liposomes to prepare the multifunctional liposomes in combination with the photothermal therapy and chemotherapy.
- Analyze the physicochemical characterization of the multifunctional liposomes.

- Investigate the morphological changes of multifunctional liposomes under hyperthermia via AFM and TEM.
- Assess the multifunctional liposomes *in vitro* against triple negative breast cancer multicellular tumor spheroids via 3D cell viability and CLSM images.

2 Materials and methods

2.1 Materials and devices

2.1.1 List of materials and chemicals

Material Name	Company
Agarose	Carl Roth GmbH + Co.KG Karlsruhe, Germany
Ammonium sulfate	Sigma Aldrich Chemie GmbH, Taufkirchen, Germany
Calcein AM, ≥ 96 % (HPLC)	Biomol GmbH Hamburg, Germany
CellTiter-Glo® 3D Reagent	Sigma Aldrich Chemie GmbH Taufkirchen, Germany
Chloroform	Sigma Aldrich Chemie GmbH Taufkirchen, Germany
Chlorpromazine, ≥ 98 %	Sigma Aldrich Chemie GmbH Taufkirchen, Germany
Cholesterol, ≥ 99 %	Sigma Aldrich Chemie GmbH Taufkirchen, Germany
Collagen I, Rat Tail	Thermo Fischer Scientific GmbH Dreieich, Germany
Coverslips, \varnothing 15 mm	Gerhard Menzel B.V. & Co. KG Braunschweig, Germany
DAPI (4',6-Diamidin-2-phenylindol)	Sigma Aldrich Chemie GmbH Taufkirchen, Germany
DMSO; ≥ 99 %	Acros Organics B.V.B.A., Geel, Belgium
Doxorubicin hydrochloride	Abcr GmbH, Karlsruhe, Germany
DPPC (1,2-Dipalmitoyl-sn-glycero-3-phosphocholine)	Lipoid GmbH Ludwigshafen am Rhein, Germany
DSPC (1,2-Distearoyl-sn-glycero-3-phosphocholine)	Lipoid GmbH Ludwigshafen am Rhein, Germany
DSPE-PEG2000 (1,2-Distearoyl-sn-glycero-3-phosphoethanolamine-N-[methoxy(polyethyleneglycol)-2000] (ammonium salt))	Lipoid GmbH Ludwigshafen am Rhein, Germany
Dulbecco's Modified Eagle Medium (DMEM)	Capricorn Scientific GmbH Ebsdorfergrund, Germany

Dynamamin Inhibitor I, Dynasore	Sigma Aldrich Chemie GmbH Taufkirchen, Germany
Fetal Calb Serum (FCS)	PAA Laboratories, Cölbe, Germany
FluorSave™	Calbiochem Corporation La Jolla CA, USA
Indocyanine Green	Carl Roth GmbH + Co.KG Karlsruhe, Germany
Lint-free laboratory wipe, Kimtech precision wipes	Kimberly-Clark Irving TX, USA
Lysis-Reagent	Promega Corporation Madison WI, USA
Methanol	Sigma Aldrich Chemie GmbH Taufkirchen, Germany
Microscope slide, glass, 76 x 26 mm	Thermo Fischer Scientific GmbH Dreieich, Germany
Microtiterplates, 96-Well, F-Boden, Nunc™	Thermo Fischer Scientific GmbH Dreieich, Germany
Microtiterplates, 96-Well, opaque F-Boden, Nunc™	Thermo Fischer Scientific GmbH Dreieich, Germany
MTT (3-(4,5-Dimethylthiazol-2-yl)- 2,5- diphenyltetrazolium-bromid)	Sigma Aldrich Chemie GmbH Taufkirchen, Germany
Petri dishes, ø10cm, for adhesion cells	Sarstedt AG & Co. KG, Nümbrecht, Germany
PI (Propidium Iodide), ≥ 98 % (HPLC)	Sigma Aldrich Chemie GmbH Taufkirchen, Germany
Potassium chloride	Merck KGaA Darmstadt, Germany
Potassium dihydrogen phosphate	Merck KGaA Darmstadt, Germany
ROTI®Histofix, Formaldehyd 4 %, pH 7	Carl Roth GmbH + Co.KG Karlsruhe, Germany
Sephadex-G25 column, PD-10 Columns	GE Healthcare, Germany
Sodium chloride	Carl Roth GmbH + Co.KG Karlsruhe, Germany
Sodium phosphate	Sigma Aldrich Chemie GmbH Taufkirchen, Germany
Sterile Filters, 0.2 µm, Nylon & Cellulose acetate	VWR International Radnor PA, USA
TEM copper grids, 400 mesh	Plano GmbH Wetzlar, Germany

Titerplates 6, 12, 48-Well, NUNC™	Thermo Fischer Scientific GmbH Dreieich, Germany
Transferpipette® S, 20 µL, 200 µL, 1000 µL	BRAND GMBH + CO KG Wertheim, Germany
Triple-Negative Breast Cancer Cell line (MDA-MB-231)	ATCC® Manassas VA, USA
Triton™ X-100	Sigma Aldrich Chemie GmbH Taufkirchen, Germany
Trypsin-EDTA, (0.5 %) in DPBS (10x)	Capricorn Scientific GmbH Ebsdorfergrund, Germany
Tubes 1.5 - 50 mL	Sarstedt AG & Co. KG Nümbrecht, Germany
Ultra-low attachment U shape 96 well-plate	Thermo Fischer Scientific GmbH Dreieich, Germany

2.1.2 List of devices

Devices	Company
Analysis Balance, Explorer EX225D	Ohaus Corporation Parsippany NJ, USA
Atomic Force Microscopy (AFM)	JPK Instruments AG Berlin, Germany
Autoclave, Tuttnauer 3850 ELC	Tuttnauer GmbH, Netherlands
Cell counter, Olympus R1	Olympus Europa SE & Co KG Hamburg, Germany
Centrifuge, J2-21	Backmann coulter, München, Germany
Coagulometer, Coatron M1	Teco GmbH, Neufahrn, Germany
Confocal laser scanning microscope, LSM 700 Zeiss Axio Observer Z1	Carl Zeiss Microscopy GmbH, Jena, Germany
DSC 7	Perkin Elmer, Rodgau, Germany
Fluorimeter, FLUOstar® Optima	BMG Labtech, Ortenberg, Germany
Gefriertrockner, Christ Alpha 1-4 LSC	Martin Christ Gefriertrocknungsanlagen Oserode Harz, Germany
Heating stir plate, IKA-COMBIMAG RCT	IKA®-Werke GmbH & CO. KG Staufen, Germany
Incubation shaker, KS 4000 IC	IKA Werke GmbH & Co. KG Staufen, Germany
Incubator, CO₂, HeraCell	Heraeus GmbH & Co. KG. Germany
Incubator, In-VitroCell NU-5841 E	NuAire, Plymouth MN, USA
Inverted microscope, Olympus CKX53, cellSens Entry Software	Olympus Europa SE & Co.KG Hamburg, Germany
LaminarAir Flow (LAF), LabGard NU-437	NuAire Inc., Plymouth MN, USA
LaminarAir Flow (LAF), Labogene SCANLAF Mars	LaboGene A/S Allerød, Denmark
Microcentrifuge 5418	Eppendorf AG Hamburg, Germany
Microscope Digital Camera, Moticam 5.0 MP	Motic Germany GmbH Wetzlar, Germany
Near-infrared ($\lambda = 808$ nm, 500 mW)	Weber Medical Lauenförde, Germany
Peristaltic pump, PD5001	Heidolph Instruments Schwabach, Germany

Rotary Evaporator	Heidolph Instrumenst GmbH & Co. KG. Schwabach, Germany
Safety Bunsen Burner, Schuett phoenix II	Schuett-biotec GmbH Göttingen, Germany
Sonicator, Bandelin Sonorex RK 100H	Bandelin Electronic, Berlin, Germany
Sonicator, Elmasonic P	Elma Schmidbauer GmbH Singen, Germany
Stereomikroskop, Stemi 2000-C	Carl Zeiss Microscopy GmbH, Göttingen, Germany
Transmission electron microscope; JEM-3010	JEOL Ltd., Tokyo, Japan
Ultrapure water system, Purelab Flex 4	ELGA LabWater High Wycombe, UK
UV-Photometer, Multiskan GO	Thermo Fisher Scientific Waltham MA, USA
UV-Photometer, UV Mini 1240	Shimadzu Corp. Kyoto, Japan
Weberneedle® Endo Laser	Weber Medical Lauenförde, Germany
Zetasizer Nano ZS	Malvern Panalytica GmbH Kassel, Germany

2.2 Methods

2.2.1 Preparation of liposome

In this work, liposomal drug delivery systems were prepared by the thin-film hydration and active remote loading methods. The lipids and ICG are solved and stored in chloroform:methanol (2:1) v/v % and the DOX in 0.9% NaCl. Table 1 shows the lipid composition and drug encapsulation of each liposome.

Table 1: Lipid compositions of the prepared liposomes.

Name	Lipid composition	Drug	Mol [%]	Abbreviation
Blank thermosensitive liposome	DPPC/DSPC/ DSPE-mPEG-2000/ cholesterol	-	85:5:5:5	TSL
Doxorubicin thermosensitive liposome	DPPC/DSPC/ DSPE-mPEG-2000/ cholesterol	DOX	85:5:5:5	DOX-TSL
Blank multifunctional liposome	DPPC/DSPC/ DSPE-mPEG-2000/ cholesterol	-	75:15:5:5	mTSL
Indocyanine green multifunctional liposome	DPPC/DSPC/ DSPE-mPEG-2000/ cholesterol	ICG	75:15:5:5	ICG-mTSL
Indocyanine green and doxorubicin multifunctional liposome	DPPC/DSPC/ DSPE-mPEG-2000/ cholesterol	ICG DOX	75:15:5:5	ICG-DOX-mTSL

2.2.1.1 Thin-film hydration method

TSL and mTSL were prepared using the thin-film hydration method (Bangham method), which is one of the earliest methods described for liposome preparation [147] (Figure 13). Appropriate amounts of lipids depending on the chosen formulation were mixed in a round bottom flask. Organic solvents were removed by rotary evaporation (Heidolph Laborota 4000) at 40 °C and 200 rpm. The obtained lipid film was then rehydrated with 250 mM ammonium sulfate (pH 5.4) to achieve a lipid concentration of 50 mg/ml. After that, the colloidal solution was sonicated in the pre-warmed ultrasound bath sonicator (Elmasonic P) for 20 minutes above the phase transition

temperature, in this case between 55 °C to 60 °C. In this step, a mix of different types of vesicles including crude multilamellar vesicles (MLV) and large unilamellar vesicles (LUV) were formed. To homogenize the size of the liposomes the mixture was extruded using a mini-extruder (Avanti® Polar Lipids Inc, Alabaster, USA). The liposomes passed through each 400, 200 and 100 nm polycarbonate membranes 21 times at 60 °C in order to form the final small unilamellar vesicles (SUV). The liposomes were then stored at 4 °C for further use.

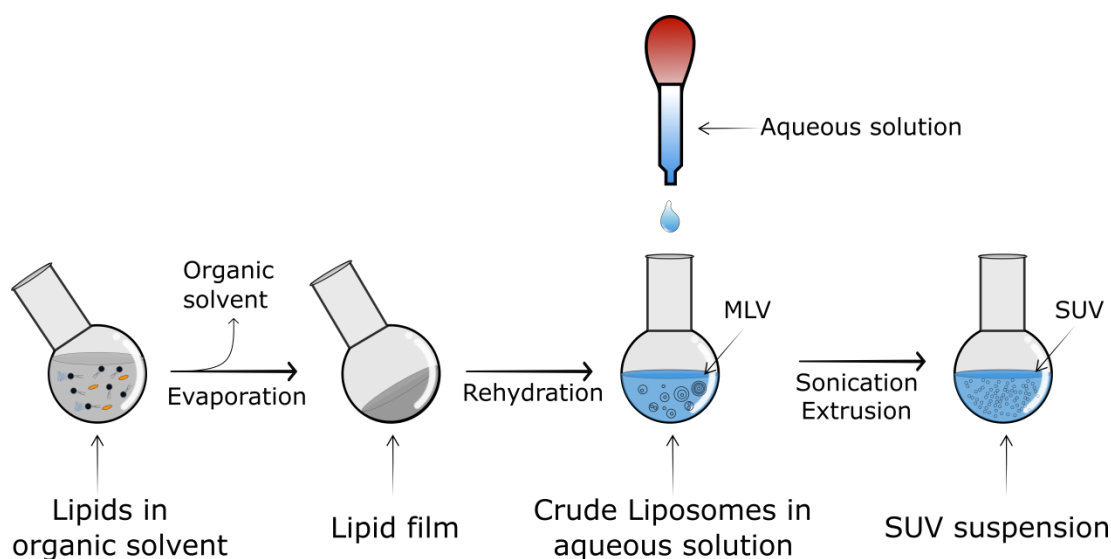


Figure 14: Schematic representation of the thin film hydration method for preparing liposomes. Lipids are added into the round bottom flask for evaporation. While the organic solvent evaporates a lipid film is formed. The lipid film gets rehydrated with an aqueous solution of ammonium sulfate, to form the crude liposomes. By using a sonicator and an extruder, the crude multilamellar vesicles (MLV) become homogenous small unilamellar vesicles (SUV).

2.2.1.2 Preparation of doxorubicin thermosensitive liposomes

(DOX-TSL)

50 mg/ml of empty TSLs were 1:20 diluted with PBS buffer (pH 7.4) to achieve both the transmembrane pH and ammonium sulfate gradients required for the DOX remote loading technique [47,148]. TSLs were then mixed with certain amount of DOX to reach the lipid: DOX ratio as 5:1 (w/w). The mixture was sonicated for 10 minutes and incubated in the water bath for another 50 minutes at 60 °C, the further loading kept going during the next 24 hours of incubation at 4 °C in dark [149].

The drug loading is always a mixture of encapsulated and unencapsulated drug

fractions. To separate the unencapsulated drugs from the liposomes is mandatory for the further experiments, for example the determination of encapsulation efficiency (EE %) and the cytotoxicity evaluation of the liposomal drug formulations [150]. The separation of remaining free DOX from the prepared liposomes was performed by ultracentrifugation method. It is based on the mechanism that liposomes sediment and forms a pellet during centrifugation whereas the free DOX stays solubilized in the PBS buffer. Unpurified liposomes were placed into Beckmann polycarbonate centrifuge tubes and centrifuged at 4 °C and 20,000 rpm for 2 hours. The supernatant was removed and the resulting pellet containing the liposomes at the bottom of the tube was resuspended in PBS as required concentration.

The final TSL and DOX-TSL were stored at concentration 5 mg/mL at cold dark conditions (4 °C) for the further experimental usage.

2.2.1.3 Preparation of multifunctional liposomes

(ICG-DOX-mTSL)

All experiments including ICG were performed in dark because of its photosensitivity. To prepare the ICG loaded liposomes, 3% ICG of the total lipid (w/w) was added into the round bottom flask with required lipids for evaporation as mentioned in the thin film hydration method. After evaporation the lipid film was rehydrated with 250 mM ammonium sulfate to 50 mg/ml colloidal solution. During the rehydration, ICG was directly encapsulated in the phospholipid bilayer with its amphiphilic characterization. Sonication and extrusion were performed to obtain the SUV of ICG-mTSL. The purification of free ICG from the prepared liposomes was performed by size exclusion chromatography (SEC) utilizing Sephadex-G25 column (PD-10 Columns, GE Healthcare, Germany). The sephadex column was washed with PBS and first added with a small amount of blank mTSL to reduce the loss of ICG-mTSL. After that ICG-mTSLs were added and eluted by PBS buffer. The eluent was collected for the further experiment steps. After purification the ICG-mTSLs were ready for loading the DOX via ammonium sulfate mediated active remote loading. Briefly, the

ICG-mTSLs were 20 times diluted with PBS and the DOX solution was added to achieve the ratio of lipid: DOX as 5:1 (w/w). The mixture was shaken for 10 minutes and incubated at 4 °C for 24 hours for remote loading. The separation of free DOX was performed after 24 hours by the ultracentrifugation at 4 °C and 20,000 rpm for 2 hours. The supernatant was removed and the resulting pellet containing the liposomes at the bottom of the tube was resuspended in PBS as required concentration.

The final ICG-mTSL and ICG-DOX-mTSL were stored at concentration 5mg/mL at cold dark conditions (4 °C) for the further experimental usage.

2.2.2 Light source

The irradiation experiment was performed with Weberneedle Endo laser (Weber medical GmbH), which was equipped with the laser module ($\lambda = 808$ nm, 500 mW) for irradiating the near-infrared dye (ICG).

2.2.3 Characterization of Liposomes

2.2.3.1 Dynamic light scattering (DLS)

The average size of different liposomal formulations were characterized by dynamic light scattering (DLS), also known as photon correlation spectroscopy (PCS). The hydrodynamic diameters of the liposomal formulations were measured by the Zetasizer Nano ZS (Malvern Panalytical, Herrenberg, Germany) and a DTS 1070 cuvette (Malvern Panalytical, Herrenberg, Germany). DLS is equipped with a 10 mW helium-neon laser at a wavelength of 633 nm at 20 °C. The light radiates into the sample at an angle of 173 °, follows by the scattering from the sample. The intensity of the scattered light is recorded and resulted as an average value with the standard deviation. The size distribution of the samples is shown as polydispersity index (PdI). Each sample was 100 times diluted in ultrapure water. The adjustment of attenuator was set to automatic mode. Each sample was measured with three replicate measurements and each measurement consists of 15 runs [151]. The results were presented as average value \pm standard deviation of three independent preparations for triplication. The samples were prepared right before the measurement in order to

retain its stability.

2.2.3.2 Laser Doppler velocimetry (LDV)

The zeta potential values were determined using Laser Doppler Velocimetry (LDV), where the scattered light is collected at an angle of 17° with Zetasizer Nano ZS (Malvern Panalytical, Herrenberg, Germany) [152]. The same dilutions of different formulations as for DLS measurements were used for the surface charge characterization. Each sample was measured with three replicate measurements and each measurement consists of 15-100 runs. The results were presented as average value \pm standard deviation of three independent preparations for triplication. The samples were prepared right before the measurement in order to retain its stability.

2.2.3.3 Atomic force microscopy (AFM)

The morphology of the liposomes were captured using the atomic force microscope (AFM), NanoWizard[®] 3 NanoScience AFM provided by JPK Instruments (Berlin, Germany). To assess the morphological changes of DOX-TSL and ICG-DOX-TSL before and after bursting, DOX-TSL was prepared at both 37°C and 40°C for the investigation. ICG-DOX-TSL was prepared before and after 15 minutes near-infrared irradiation. $20\ \mu\text{L}$ of each sample was diluted in ultrapure water (1:100) and then pipetted onto a silicon wafer. Liposomes were left for 5 minutes for sedimentation, the liquid was then aspirated and leaving a thin film of aligned vesicles on the wafer. The cantilevers used were of type HQ: NSC14 Al/BS with a length of $125\ \mu\text{m}$, a resonance frequency of $140\ \text{kHz}$ and a force constant of $5\ \text{N/m}$. All measurements were done in AC mode. The images were acquired with a size of $1\ \mu\text{m}^2$ at a scan speed of $1.5\ \text{Hz}$ [153].

2.2.3.4 Transmission electron microscopy (TEM)

The surface structure and morphology of the formulations were also investigated by transmission electron microscope (TEM) JEM-3010 (JEOL) with a retractable high-resolution slow-scan CCD-Camera (Gatan MegaScan 794). To assess the morphological changes of DOX-TSL and ICG-DOX-TSL before and after trigger

release. DOX-TSL was prepared at both 37 °C and 40 °C for the investigation. ICG-DOX-TSL was prepared before and after near-infrared irradiation. Liposomes were ten times diluted with PBS buffer (pH 7.4) and then stained with uranyl acetate (2%) for 30 minutes. Samples were pipetted onto 300 mesh formvar coated S160-3 copper grids (Plano GmbH Wetzlar, Germany). Equal parts of the sample and uranyl acetate were mixed and the grid was incubated for 5 min in this solution. The mixture was examined at an accelerating voltage of 300 kV and 110 µA emission current with current densities between 50-60 pA/cm².

2.2.3.5 Differential scanning calorimetry (DSC)

DSC-7 Perkin Elmer (Rodgau, Germany) was used to perform DSC for the determination of the phase transition temperature. Samples were measured in both PBS buffer and citrate buffer. The scanned temperature range was set from 5 °C to 90 °C, and the heating rate was 1 °C per minute. The reference cells were filled with PBS buffer or citrate buffer. The DSC data was analyzed by using Pyris software, and the peak maximum was set as the transition temperature (T_m) [147].

2.2.3.6 Encapsulation efficiency

Size exclusion chromatography (SEC) was utilized to separate the free ICG from the ICG-TSL. Before adding ICG-TSL, the Sephadex-G25 column (GE Healthcare) was saturated with blank TSL of the measured formulation to prevent any remarkable loss of the lipid material. The ICG-TSL eluent was 100 times diluted in methanol in order to lyse the liposome and release the encapsulated ICG, then the amount of ICG was calculated by the calibration curve of ICG in methanol measured by UV/Vis spectrophotometry (UV mini 1240, Shimadzu, Suzhou, China) [154]. The same dilution of blank TSL in methanol was used as control in the measurement. The encapsulation efficiency (EE %) of ICG was calculated according to the following equation (**Equation 1**) :

Equation 1

$$EE\% = \frac{\text{amount of ICG encapsulated in liposomes}}{\text{Initial amount of ICG}} \times 100\%$$

The separation of free DOX from DOX-TSL and ICG-DOX-TSL was performed by ultracentrifugation method. The encapsulation efficiency of DOX was calculated in an indirect method. After 2 hours of centrifugation the resulted supernatant were collected and 10 times diluted in PBS buffer (pH 7.4). The amount of DOX in the supernatant was measured by UV/Vis spectrophotometry (UV mini 1240, Shimadzu, Suzhou, China) and calculated by the calibration curve of DOX in PBS buffer (pH 7.4) [154]. The encapsulation efficiency (EE %) of DOX was calculated according to the following equation (**Equation 2**)

Equation 2

$$EE\% = \frac{\text{Initial amount of DOX} - \text{amount of unencapsulated DOX}}{\text{Initial amount of DOX}} \times 100\%$$

2.2.3.7 Liposomes stability

Colloidal stability of DOX-TSL and ICG-DOX-TSL was determined in terms of average size, polydispersity index (PDI) and zeta potential at storage condition, i.e. at 4 °C in dark. The measurement methods were described in section Dynamic light scattering (DLS) and Laser Doppler velocimetry (LDV). The stability of DOX-TSL was further evaluated at physiological conditions with a cell culture medium. 100 µl of liposomes were mixed with 900 µl DMEM medium supplemented with 10 % FCS and incubated at 37 °C for 24 h. Samples were collected at different time intervals to measure the size, PDI and zeta potential for stability studies. Results were calculated with data from three independent experiments.

2.2.3.8 Drug release

The DOX released from the liposomal system was determined by the cumulative release of DOX from the DOX-TSL was performed at 37 °C and 40 °C at different time intervals (up to 60 minutes). 1.5 mL of DOX-TSL (containing 1 mg DOX) were transferred into a dialysis bag (MWCO = 6,000-8,000) and incubated in 50 ml of PBS (pH 7.4) or citrate buffer (pH 5.5) pre-heated to the aforementioned temperatures with a stirring speed of 100 rpm. Then 1 mL from the dialysate was collected at selected time points (15 minutes, 30 minutes, 45 minutes, 1 hour, 2 hours, 3 hours and 4 hours) and

replaced with 1 ml of fresh PBS or citrate buffer to maintain the volume constant. To determine the amount of DOX released at different time points, collected samples were analyzed by UV/Vis spectrophotometry (UV mini 1240, Shimadzu, Suzhou, China) at wavelength of 485 nm. The release of DOX was calculated according to the following equation (Equation 3) using a calibration curve of DOX in PBS or citrate buffer

Equation 3

$$\text{Cumulative Dox release\%} = \frac{\text{Dox released}}{\text{initial amount of Dox}} \times 100\%$$

2.2.4 Cell culture experiments

2.2.4.1 Cell condition

The epithelial adenocarcinoma triple-negative breast cancer cells, MDA-MB-231 (ATTC) were used for the cell culture experiments in this work. The cells were cultivated in Dulbecco's Modified Eagle Medium (DMEM) (Capricorn Scientific) with the supplements of 10 % fetal calf serum (FCS) (PAA, Cöbe, Germany) and 1% non-essential amino acid (Biochrom, Berlin, Germany). The cells were incubated under the condition of 37 °C, 7% CO₂ and 90% relative humidity. The cells were regularly passaged when they are 80-90% confluent in the 10 cm diameter adherent petri dish (Sarstedt AG & Co. KG, Nümbrecht, Germany), in order to maintain sufficient growth ratios.

2.2.4.2 3D cell culture model (spheroids) formation

The concept of 3D cell culture is to grow cells in multilayers but not monolayer [134]. In this structure, multicellular tumor spheroid (MCTS) can mimic the physical and biochemical features of solid tumor mass. This requires the compact aggregation of cells in non-adherent culture conditions where the extracellular matrix (ECM) provides a condition for cellular to attach each other. Here we use agarose (NEEO Ultra-Quality Carl Roth, Karlsruhe, Germany) to coat through the surface in order to provide non-adherent culture condition [143]. 1% agarose (w/v %) was added in PBS without Ca²⁺/Mg²⁺ solution (Biochrom, Berlin, Germany). The mixture was then autoclaved for 20 minutes at 121 °C. The agarose solution stayed on a heating plate to prevent

solidification before use.

MDA-MB-231 cells were applied to establish a protocol for rapid spheroid generation in 96-well plate (NUNC™, Thermo Fisher Scientific, Dreieich, Germany). The wells in the outer rim were filled with 200 μL PBS without Ca^{2+} and Mg^{2+} providing a homogeneous humidity for each well of the plate. The inner wells were first coated with 50 μL agarose solution in each well and wait for the solidification (Figure 15).

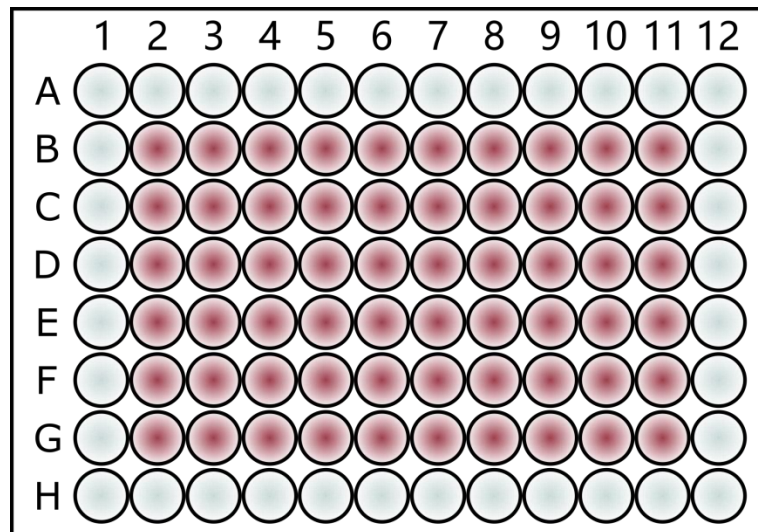


Figure 15: schematic representation of the seeding format on 96 well plate of spheroid generation. The outer wells (blue) are filled with 200 μL PBS buffer to provide a homogenous humidity of the whole well plate. The inner wells (red) are first coated with 1% agarose PBS solution, and then seeded with required amount of cells in cell culture medium supplied with 1% FCS and 3 $\mu\text{g}/\text{mL}$ collagen I.

After that 1000-6000 cells were seeded into each well with 3 $\mu\text{g}/\text{mL}$ collagen I, Rat Tail (Thermo Fisher Scientific GmbH, Dreieich, Germany) as extracellular matrix (ECM). Then the 96-well plates were centrifuged at room temperature for 3 minutes at 2300 rpm (Mikro 220R, Andreas Hettich GmbH & Co.KG). Cells were incubated at 37 $^{\circ}\text{C}$ and 7% CO_2 for spheroid generation. From the seeding day (Day 0) cells should not be disrupted for 3 days. The medium was not changed during spheroid generation. By Day 5 the spheroids were ready for the further experiments. The generation of spheroids in different seeding density on different days was captured by a fluorescence microscope CKX53 (Olympus Corp., Tokyo, Japan).

2.2.4.3 Cytotoxicity studies of DOX-TSL upon hyperthermia

Two plates of MDA-MB-231 spheroids were generated at a cell density of 1000

cells/well and incubated for 5 days till the necrotic zone is observed and the spheroid's diameter is over 400 μm . Then, the medium was replaced by 200 μL containing TSL, DOX-TSL, and free DOX with different concentrations of DOX (between 5–500 $\mu\text{g}/\text{mL}$).

Afterwards, one plate of spheroids was incubated for 4 hours at 37 $^{\circ}\text{C}$ representing the normal physiological condition; another plate for 3 hours at 37 $^{\circ}\text{C}$ and followed by 1 hour at 40 $^{\circ}\text{C}$ as mild hyperthermia treatment. After 4 hours incubation the spheroids were then incubated in fresh medium for another 24 or 48 hours.

To value the cytotoxicity at different temperature, spheroids were treated with free DOX or DOX-TSL at a final concentration of 250 $\mu\text{g}/\text{mL}$ of DOX and incubated for 3 hours at 37 $^{\circ}\text{C}$, followed by thermal treatment at 40, 41, 42 $^{\circ}\text{C}$ for 1 hour, respectively. The medium was replaced with fresh medium and spheroids were further incubated for 24 hours. Control untreated spheroids were incubated at the same temperatures and incubation times.

2.2.4.3.1 3D cell (spheroids) viability assay

Quantification of the cell viability in the spheroid is calculated by the measurement of the intracellular ATP content. The oxidation of luciferin by the luciferase enzymes presents intracellular ATP and emission of bioluminescence. After treatment, spheroids were washed and transferred to an opaque 96 well plate with 100 μL fresh medium. Subsequently, 100 μL of CellTiter Glo[®] 3D reagent (Sigma Aldrich Chemie GmbH) was added to each well. The blank samples were set as 100 μL medium with 100 μL 3D reagent. Subsequently, spheroids were mixed vigorously by using a plate shaker (KS4000 IC, IKA Werke, Staufen, Germany) for 15 minutes in order to induce cell lysis. Afterwards, the spheroids were incubated for 15 minutes at room temperature in dark. The spheroid viability was determined by luminescence measured by plate reader FLUOstar Optima (BMG). The untreated spheroids were used as negative control representing 100% viability, and TritonX[®] treated spheroids were used as a positive control. Each sample took three wells for the average result.

2.2.4.3.2 3D cell (spheroids) cellular uptake assay

To assess the cellular uptake of DOX-TSL on spheroid, spheroids were fixed with 4% formaldehyde for 10 minutes at room temperature after treatment. The cell nuclei were stained by nuclei dye DAPI (4',6-diamidino-2-phenylindole) at 0.1 µg/mL for 15 minutes [155]. The spheroids were 2 times washed with PBS buffer and transferred onto glass slides for observing by confocal laser scanning microscopy (CLSM) (Zeiss Axiovert LSM700, Carl Zeiss Microscopy, Jena, Germany).

2.2.4.3.3 3D cell (spheroids) live/dead staining assay

Live/dead staining assay can visualize the cell viability by staining the spheroids with the chosen dyes to distinguish viable and dead cells. In live cells, the non-fluorescent calcein AM can be converted to green fluorescent calcein with the present of esterase. Whereas the propidium iodide (PI), as a fluorescent DNA-binding dye, cannot pass through the living cell membrane, but the disordered dead cell membrane and intercalate with the DNA double helix.

The staining solution was freshly prepared before use, Calcein AM (5 µg/mL) and PI (20 µg/mL) were diluted in DMEM without FCS.

After treatment the medium of spheroids was removed, 200 µL of the staining solution was added to each well. Spheroids were incubated in dark at room temperature for 15 minutes. After that the spheroids were washed with PBS buffer, and transferred onto glass slides for imaging with confocal laser scanning microscopy (CLSM) (Zeiss Axiovert LSM700, Carl Zeiss Microscopy, Jena, Germany).

3 Results and discussion

3.1 Doxorubicin encapsulated thermosensitive liposomes (DOX-TSL): characterization and visualization

3.1.1 Physicochemical characterization of liposomes

Liposome-based formulation was designed in order to improve the chemotherapeutic efficacy and reduce the cytotoxicity of DOX. Thermosensitive doxorubicin liposome (DOX-TSL) was prepared and systematically characterized. Remote loading of DOX was achieved using an ammonium sulfate concentration gradient between the liposomal interior and the exterior environment [148, 156] (Figure 16).

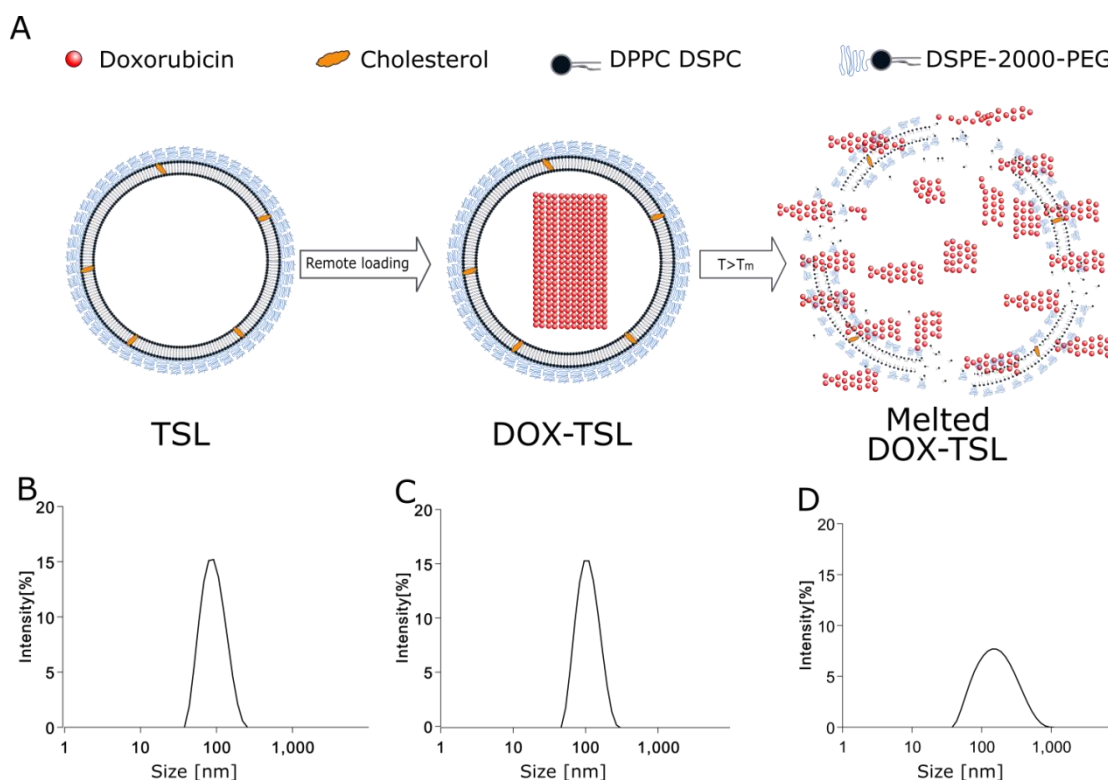


Figure 16: A: Schematic representation of DOX-TSL. TSL were prepared with thin film hydration method and homogenized by sonication and extrusion. DOX was encapsulated by remote loading method. Temperature was increased over the phase transition temperature (T_m) to control release the DOX from liposome. B: DLS size analysis of TSL. C: DLS size analysis of DOX-TSL. D: DLS size analysis of DOX-TSL after heating above $T > T_m$.

The hydrodynamic diameters of the formulations were determined by Dynamic light scattering (DLS). The obtained size in the case of TSL liposomes shows the mean diameter of 83.31 ± 2.70 nm. Meanwhile, the polydispersity index (PdI) < 0.2 indicates a narrow size distribution of the formulation. The particle size and PdI

increased upon the encapsulation of DOX (DOX-TSL) to 102.50 ± 13.13 nm and 0.22 ± 0.06 . As seen from Figure 16C and 16D, the intensity curve of the DOX-TSL became flat and moved to the right side, which means the increase of the liposomal average size and polydispersity index, indicating the deformation of the liposomes. The size of the DOX-TSL is in the range of the preferential tumor penetration via EPR effect due to its ability to distribute the liposomes between 50-150 nm diameters to the tumor site. The PEGylation of liposomes prevents opsonization and reduces the clearance of reticuloendothelial system (RES). Hence, the PEGylation prolongs the circulation time of the formulation [60]. The increase of the zeta potential from TSL (-21.20 ± 8.23 mV) to DOX-TSL (-8.18 ± 3.89 mV) is attributed to the positively charged DOX.

3.1.2 Encapsulation efficiency (EE%)

DOX was encapsulated into the liposomes via ammonium sulfate remote loading method with 5:1 (w/w) ratio of lipid: DOX. This method relied on the driving force of loading amphipathic weak alkaline drug such as DOX which was firstly reported by Bahrenholz [47]. As seen in Table 2, This formulation has achieved a high entrapment efficiency of DOX (89.90 ± 1.89 %), which is comparable to the result previously reported where the entrapment efficiency of 92.30% and 84.07% were obtained for DPPC based Doxorubicin thermosensitive liposomes of mean diameter 120.43 ± 1.91 nm [152].

Table 2: Physiochemical properties of TSL and DOX-TSL liposomes. Hydrodynamic diameter (Diameter), polydispersity index (PdI), zeta potential (zP), encapsulation efficiency (EE %). The hydrodynamic diameter is expressed as a measure of particle size distribution by intensity (mean \pm SD, n = 3).

	Diameter \pmSD [nm]	PdI \pmSD	zP \pmSD [mV]	EE \pmSD [%]
TSL	83.31 ± 2.70	0.15 ± 0.03	-21.20 ± 8.23	--
DOX-TSL	102.50 ± 13.13	0.22 ± 0.06	-8.18 ± 3.89	89.90 ± 1.89 DOX:lipid 1:5(w/w)

3.1.3 Differential scanning calorimetry (DSC)

DSC was performed to determine the temperature of transforming the lipid bilayer from gel phase to liquid crystalline phase. In order to control release drug at a mild hyperthermia range, the phase transition temperature (T_m) was desired at the range of 40-42 °C. TSL and mTSL liposomes were measured in both PBS buffer and citrate buffer. The lipid composition of DPPC: DSPC: DSPE-mPEG2000: cholesterol with the molar ratio present of 85: 5: 5: 5 and 75: 15: 5: 5, respectively. As shown in Figure 17, the thermosensitive properties of the formulations were first detected at around 38 °C, where the lipid bilayer started the gel to liquid transformation. The transition temperature (T_m) of TSL and mTSL were obtained at 41.2 °C in both buffer, suggesting the pH environment does not change the T_m of the formulation. After the encapsulation of DOX, the T_m was recorded at 39.8 °C. Based on these results, liposomes remain their integrity in the blood circulation and bust at the tumor site upon mild hyperthermia application [152]. Therefore, the targeted trigger release is achieved.

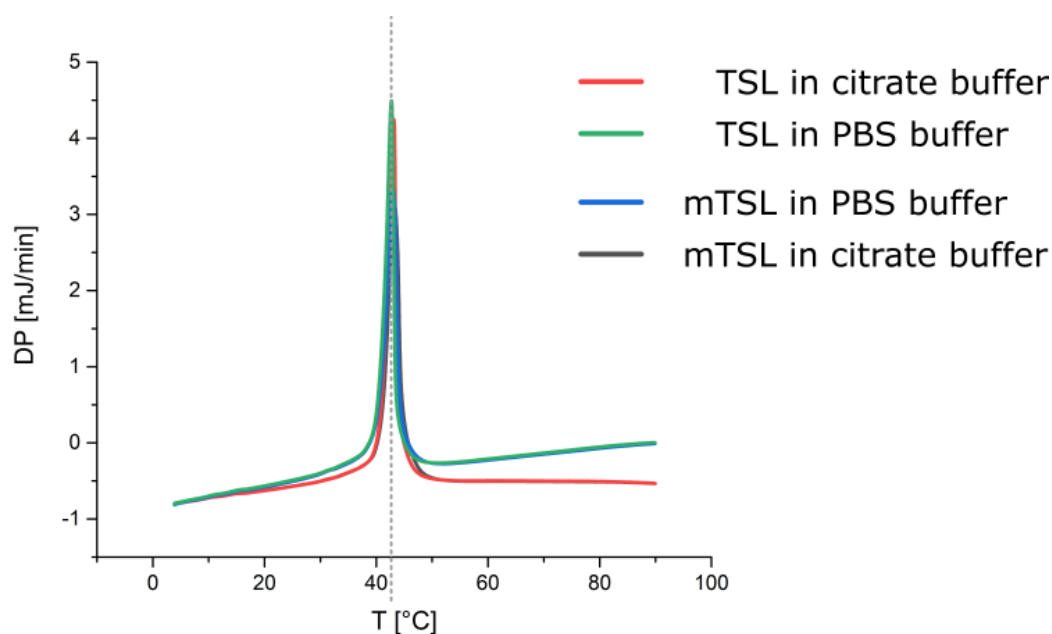


Figure 17: DSC thermogram of TSL (lipid composition DPPC: DSPC: DSPE-mPEG2000: cholesterol of 85: 5: 5: 5 (molar ratio)) and mTSL (lipid composition DPPC: DSPC: DSPE-mPEG2000: cholesterol of 75: 15: 5: 5 (molar ratio)) in PBS buffer or citrate buffer. The heating rate is 1 °C/ min, scanned temperature range was 5 to 90 °C.

3.1.4 Visualization of DOX-TSL

3.1.4.1 Atomic force microscopy (AFM)

Atomic force microscopy (AFM) was used to visualize the morphological aspects of TSL and DOX-TSL (Figure 18). Although the encapsulated drug was unable to be visualized, AFM provides additional information on the shape and surface features of liposomes which helps to better understand the liposomal characteristics and behavior. The diameter of TSL and DOX-TSL measured by AFM correspond well with the DLS results as mentioned previously.

The obtained size by AFM slightly increased compare to the DLS results due to the adhesion of the liposomes on the wafer surface. The size of DOX-TSL showed a slight increase compared to TSL, which is also corresponding with the DLS results. AFM images showed the liposomal vesicles segregated in round shape and well distributed without any aggregation or fusion at 37 °C. After one hour incubating at 40 °C, the temperature dependent deformation of liposomes was observed. When the incubation temperature is over T_m , the single round vesicular structures of liposomes were deformed. The size of the broken liposomes varied in both direction and the homogeneity of the liposomes was destroyed. This indicates that the integrity of the liposomes was destroyed so that the encapsulated drug is able to be released. As seen from Figure 18C, some aggregations of the broken liposomes were observed under AFM. They attached to each other instead of being segregated.

Additionally, the deformed liposomes lost the spherical shape and overlapped each other according to the cross sectional profile (Figure 18I). The highest measured nm in the liposomal formulation was between 9 to 15 nm at 37 °C, whereas after the hyperthermia application the height decreased to 4-5 nm. The height of DOX-TSL decreased about 50-60% after heating, which also indicates the destruction of the liposomal integrity.

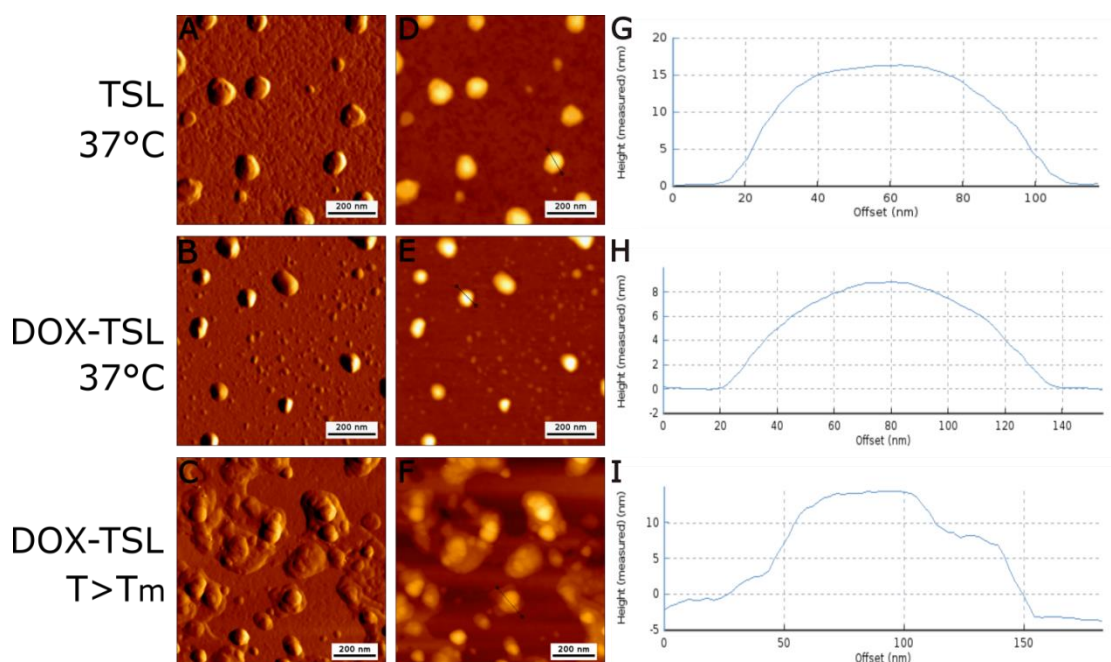


Figure 18: Atomic force microscopy (AFM) micrographs of TSL at 37 °C, DOX-TSL (before heating) and DOX-TSL (after heating). A, B, C show the morphological characteristics of three samples. D, E, F, show the cross-section of the samples in measured height trace with the identified lines. G, H, I show the height of the cross-sectional profile along the identified line. Scale bar represents 200 nm.

3.1.4.2 Transmission electron microscopy (TEM)

Transmission electron microscopy (TEM) was performed to further analysis the morphological characteristics. The TEM images provide the direct structural information of the samples. TSL and DOX-TSL under TEM showed round spherical vesicles at 37 °C, and the lipid bilayer showed integrated structure. The stability of the DOX-TSL was observed after hyperthermia application. After incubating the DOX-TSL at 40 °C for one hour, the lipid bilayer transformed from liquid condensed phase (L_{β}) to liquid expanded phase (L_{α}) as mentioned previously, so that the lipid bilayer started to break apart and the integrity of the liposomes was therefore destroyed. Under the TEM, the broken liposomes and the fragments of the lipid bilayer was observed (Figure 19).

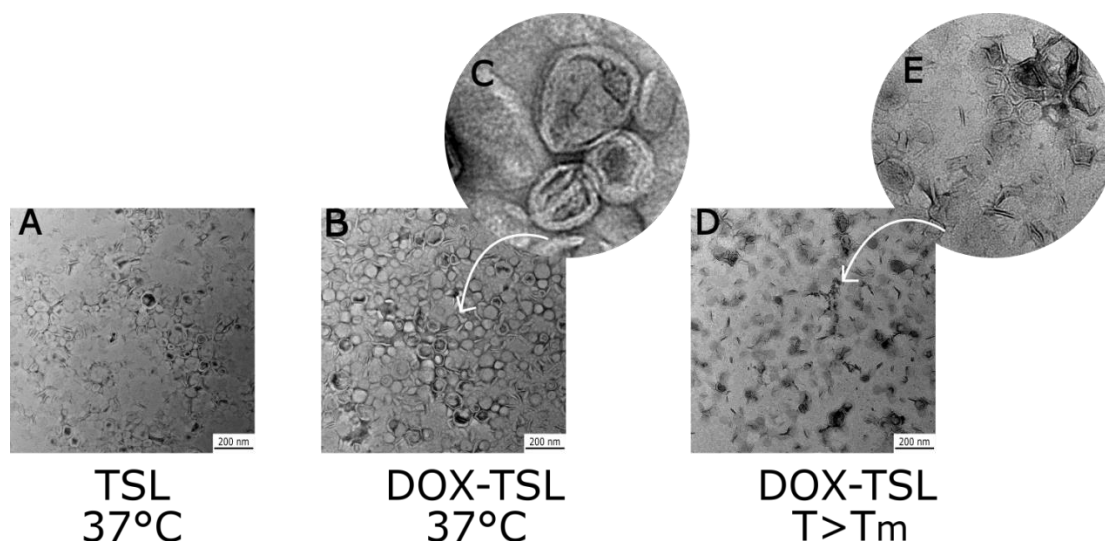


Figure 19: Transmission electron micrographs (TEM) of A: TSL at 37 °C; B and C: DOX-TSL before heating, D and E: DOX-TSL after heating over phase transition temperature (T_m). DOX-TSL after heating over the T_m , the integrity of the lipid membranes is destroyed, the fragment of the lipid bilayer was observed. Scale bar represents 200 nm.

3.1.5 Stability of DOX-TSL

3.1.5.1 Colloidal stability

The colloidal stability of DOX-TSL was investigated for 6 weeks storage in terms of size, PdI and zeta potential (Table 3).

DOX-TSL was stored in dark at 4 °C. The size of the DOX-TSL increased 10 nm (8%) in 6 weeks, which demonstrated that the formulation remained the initial particle size without any noticeable precipitation or aggregation. Meanwhile, PdI slightly increased from 0.22 ± 0.06 to 0.24 ± 0.04 , which indicate that the liposomes remained unimodal, homogeneous and stable during the storage. The negligible change of size and PdI indicates that the DOX-TSL formulation remains stable dispersion and excellent colloidal stability.

From the zeta potential perspective, the obtained value increased from -8.18 ± 3.89 mV to -10.30 ± 5.19 mV. This slight decrease of the zeta potential value represented a minor premature DOX leakage occurred during the storage. However, the changes in zeta potential values were not significant. To quantify the leakage of DOX, it can be further determined by weekly measuring the entrapment efficiency of DOX. However, in this project we didn't perform this experiment due to the minor change of the other

results.

Altogether with the above results, DOX-TSL remains physically and chemically stable at 4 °C in dark for 6 weeks.

Table 3: Colloidal stability of DOX-TSL for 6 weeks in dark at 4 °C. Hydrodynamic diameter (Diameter), polydispersity index (PdI), zeta potential (zP). The hydrodynamic diameter is expressed as a measure of particle size distribution by intensity (mean \pm SD, n = 3)

Time [weeks]	Diameter \pmSD [nm]	PdI \pmSD	zP \pmSD [mV]
1	102.50 \pm 13.13	0.22 \pm 0.06	-8.18 \pm 3.89
2	103.10 \pm 15.36	0.24 \pm 0.04	-7.23 \pm 4.10
3	105.10 \pm 9.63	0.21 \pm 0.08	-5.86 \pm 3.22
4	109.80 \pm 12.82	0.22 \pm 0.06	-7.26 \pm 3.06
5	105.60 \pm 4.44	0.22 \pm 0.06	-6.27 \pm 1.10
6	112.50 \pm 10.78	0.24 \pm 0.04	-10.30 \pm 5.19

3.1.5.2 Serum stability

To asserting the liposomal stability during cell culture experiments, the biological integrity of DOX-TSL was investigated in terms of size, PdI and zeta potential value while incubating the formulation with cell culture medium DMEM supplemented with 10% FCS at 37 °C.

Table 4 shows the results directly mix the formulation with medium at 37 °C and after 1, 4 and 24 hours. Based on the results obtained, a slight increase in the average size measurement was observed. However, the results remained within the same range as those recorded under storage conditions. The PdI values were obtained in the range of 0.3-0.4. This phenomenon can be attributed to the interference of protein particles in the medium that are over 2000 nm in size. The DLS size distribution graph indicated that the liposomal formulation remained its construal integrity within the initial range and there was no significant change observed (Figure 20). DOX-TSL remained stable in serum for 24 hours. It means DOX-TSL maintains its integrity during the incubation time of cell culture experiments, preventing encapsulated DOX from

leaking out and interfering with result.

Table 4: Serum stability of DOX-TSL incubated in DMEM (DMEM: liposomes 10:1 [v/v]). Hydrodynamic diameter (Diameter), polydispersity index (PDI), zeta potential (zP). The hydrodynamic diameter is expressed as a measure of particle size distribution by intensity (mean \pm SD, n = 3)

Time [h]	Diameter \pm SD [nm]	PDI \pm SD	zP \pm SD [mV]
0	101.1 \pm 8.42	0.413 \pm 0.05	-5.17 \pm 0.30
1	91.32 \pm 11.04	0.382 \pm 0.09	-4.41 \pm 0.61
4	111.6 \pm 18.96	0.330 \pm 0.09	-7.38 \pm 1.24
24	113.6 \pm 13.23	0.397 \pm 0.06	-8.39 \pm 0.87

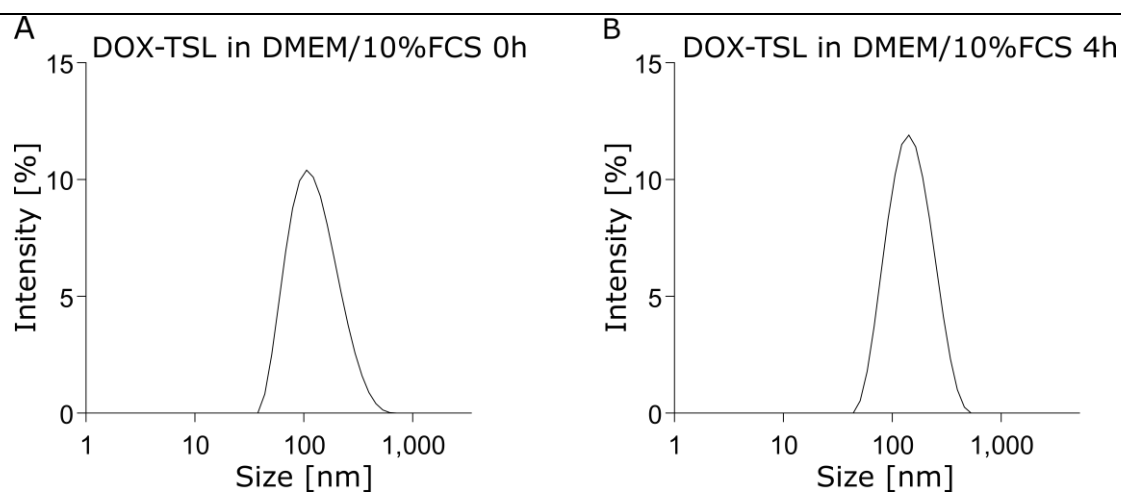


Figure 20: DLS Size analysis of DOX-TSL in DMEM/10% FCS (DMEM: liposomes 10:1[v/v]). A: DOX-TSL mix with DMEM/10% FCS. B: DOX-TSL incubated in DMEM/10%FCS after 4 hours.

Zeta potential remained the initial value which is attributed to the presence of PEG. When liposomes are administrated in cell culture experiments; they are exposed to various proteins in the medium. These proteins, especially opsonins (complement proteins and immunoglobulins) are able to adsorb and format protein corona on the liposomes' surface thus change diverse physicochemical properties of the liposome. The opsonins affect TSL by increasing the permeability of the lipid bilayer leads to the premature leakage of the drug [44]. However, grafting the liposomes with PEG can effectively prevent the adsorption of opsonins with the steric repulsion therefore avoid the protein corona formation of liposomes and the premature leakage in cell culture condition, furthermore, in clinical utilization [157,158].

3.1.6 Drug release assay

Temperature dependent drug release is one of the most important properties of thermosensitive liposomes. While heating the liposomes over their phase transition temperature (T_m), the liposome lipid bilayer transforms from liquid condensed phase to liquid expanded phase [159]. In Liquid expanded phase, the permeability of the lipid bilayer is increased therefore the encapsulated drug can be release consequently. As the microenvironment of the tumor tissue is acidic, the drug release was investigated in both PBS buffer (pH 7.4) and citrate buffer (pH 5.5).

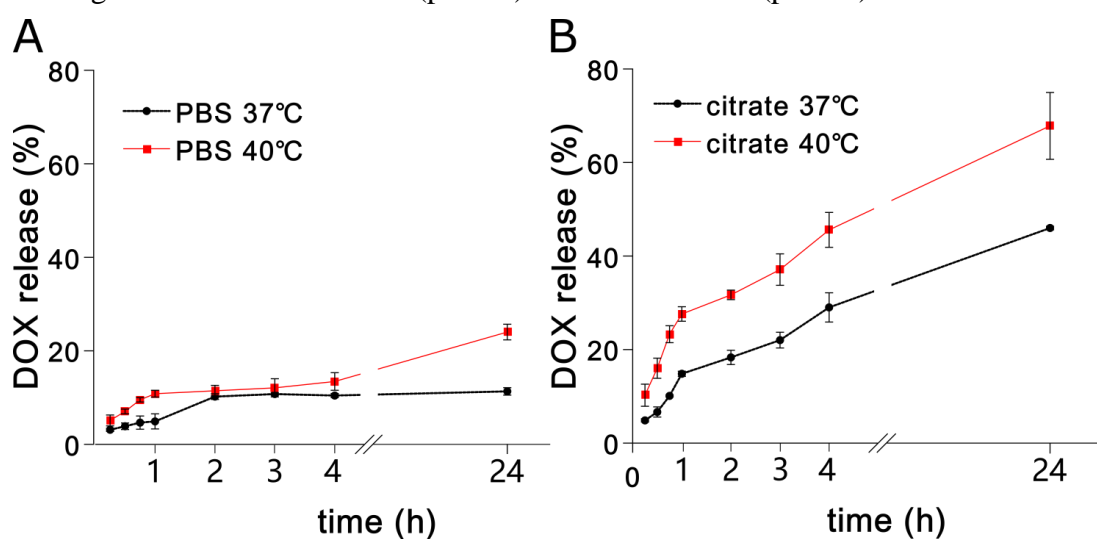


Figure 21: Cumulative release profile of DOX from DOX-TSL in PBS buffer (pH 7.4) (A) and citrate buffer (pH 5.5) (B) at 37 °C and 40 °C. DOX release was plotted as an average of percentages \pm SD of three independent experiments and the release of DOX within the first 24 hours was measured.

In PBS buffer (Figure 21A), the obtained release remained at 4.65 % in the first hour and reached 10% after 4 hours incubation, which indicated that there is no significant release; Meanwhile, the release of DOX in PBS at 40 °C was observed start from 30 minutes of the incubation and reached 7.05% and increased to 13.45% after 4 hours. The low drug release at 40 °C in PBS buffer is not as expected. According to the results, there is no significant difference of drug release between 37 °C and 40 °C. However, in citrate buffer (Figure 21B), a significant difference of drug release at different temperatures was observed. At 37 °C, DOX released 6.66% after 30 minutes incubation, and reached up to 29.02% after 4 hours at 37 °C. Whereas at 40 °C, DOX rapidly released 10.25% after 15 minutes, 27.61% in 1 hour, 45.60% after 4 hours and

67.83% after 24 hours.

According to this observation, it is speculated that DOX-TSL in citrate buffer (pH 5.5) shows more sensitivity of temperature dependent stimuli-control release. Due to the endogenous difference, the natural acidic tumor tissues show a preferable drug release of DOX-TSL under physiological condition (37 °C). Moreover, the exogenous hyperthermia application (40 °C) enhances the drug release on the tumor site and minimizes the drug release to the surrounding healthy tissue in a non-acidic environment.

3.2 Cell culture experiments

3.2.1 Spheroid generation

The concept of 3D cell culture is to grow cells in multilayers but not monolayer [134]. In this structure, multicellular tumor spheroid (MCTS) mimics the physical and biochemical features of solid tumor. This requires the compact aggregation of cells in non-adherent culture conditions where the extracellular matrix (ECM) provides a condition for cellular to attach each other. ECM has also been investigated generating biochemical signals thus influencing the intracellular signaling cascades, therefore interfere the microenvironment of mammary epithelial cells [160]. Collagen I from rat tail tendons was utilized as ECM for increasing the intercellular contact due to its biocompatibility and low antigenicity [128, 161].

In an ultra-low attachment U shape 96 well-plate, MDA-MB-231 cells were seeded with or without collagen I and incubated for 5 days without disturbing. The result is demonstrated by the microscope photos showing the different sizes and geometries of MDA-MB-231 cells cultured in the presence and absence of collagen I (Figure 22).

Cells with the presence of collagen I started to generate spheroid and form a compact structure after 2 days of seeding. Due to the absence of angiogenesis in the spheroid, cells in the inner layers have limit on reaching medium components and discarding metabolic waste. Therefore the volume of necrotic zone and quiescent zone get slowly increased along with the growth of the spheroid. The necrotic zone is usually

observed when the spheroid grows over 400 μm diameter, which is symbolic for big spheroid.

Cells without collagen only formed a loose cell aggregation by the natural gravity. Over time the cell cluster only grows big in size by cell proliferation but not become compact as spheroid. It is easy to be dispersed by additional force including pipetting and shaking which are not able to destroy spheroid.

Besides, there is no necrotic zone observed in the center of the cell cluster. It is because there is no gradient of nutrient or waste transport in the cell cluster as it occurs in spheroid. The homogeneous capacity of acquiring the nutrients in the medium and removing the metabolic wastes occur to all cells. This also explains that cells have higher rate of proliferation without collagen I than with it. The slight dark core of the cell cluster observed under the microscopy is caused by the overlap of the cells.

When we have a close look on the big spheroids (diameter over 400 μm), different layers are clearly observed. On Figure 23, two MDA-MB-231 spheroids clearly show the different layers of the spheroids. Figure 23A is a 5-day-old spheroid with 1000 cells seeding density whereas Figure 23B is a 3-day-old spheroid of 5000 cells seeding density.

Both spheroids show very dark core in the spheroids, representing the necrotic zone. In this area, cells can barely obtain the nutrients and oxygen, meanwhile the metabolic waste and CO_2 accumulate here due to the limitation of the transport. Thus cells rapidly deplete oxygen and nutrients therefore lead to cell death.

The most proliferating cells lay on the outermost layer of spheroids. Cells in this area not only obtain sufficient oxygen and nutrients from the medium, but facing no limitation of transporting metabolic waste and CO_2 as well. Thus they contribute the major growth of the spheroid with these benefits, hence this area is named proliferating zone.

Between the proliferating zone and the necrotic zone, a slight dark ring is observed.

Here cells keep quiescent due to the decrease of cell metabolism speed. Along with the spheroid growth, the decrease of cell metabolism is correlated with the increase of the distance from the cells to the spheroid periphery, and the quiescent zone progressively becomes necrotic.

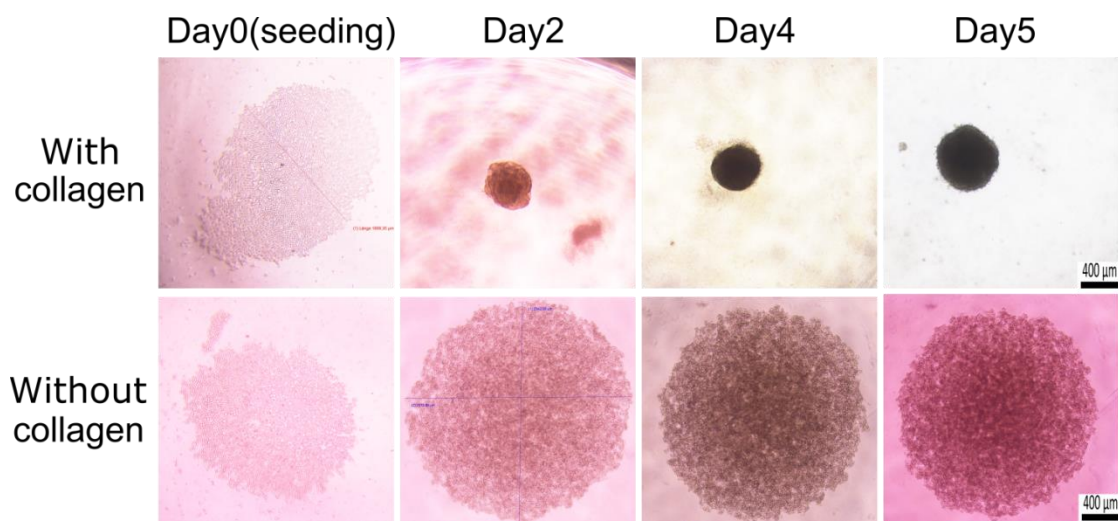


Figure 22: Size and geometry of MDA-MB-231 cells seeded on ultra-low attachment U shape 96 well plate for spheroid generation with and without collagen I (seeding density: 5000 cells/well). The images of spheroids (with collagen) and cell aggregates (without collagen) were captured by microscopy. Images on day 0 (seeding) was captured after 3 minutes centrifugation at 2300 rpm, room temperature. Scale bar represents 400 μm .

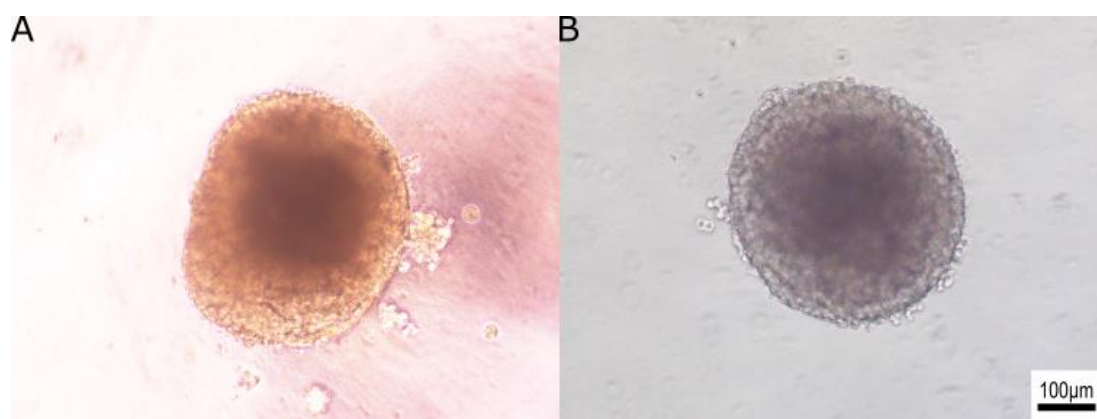


Figure 23: MDA-MB-231 spheroids represent the proliferating zone, quiescent zone and necrotic zone. A: Spheroid was seeded at a density of 1000 cells and incubated for 5 days. B: Spheroid was captured by fluorescence microscope at day 3 at seeding density of 5000 cells. Both spheroids show different layers of the spheroid structure. From external to internal they are proliferating zone, quiescent zone and necrotic zone. The scale bar represents 100 μm .

3.2.2 Spheroids growth curve

To further investigate the influence of seeding density to the proliferation, MDA-MB-231 cells were then seeded in different density on agarose coated 96 well plate. The agarose provides a non-adherent culture condition with a concave surface shape for spheroids generation [143]. Seeding densities were chosen from 1000 cells to 6000 cells in order to cover a big range. The spheroids were measured and taken image under the same condition every day. On morphological prospect, there are several changes observed during the spheroid generation. Initially, single cells aggregate and assemble to a cell cluster spontaneously. Individual cells are identifiable in this stage. Afterwards, the periphery of the cell cluster becomes smooth and continuous. The external cells are barely recognized and meanwhile, the internal cells strongly connect to each other and slowly form the quiescent zone and necrotic core. In this stage the single spheroid is formed from initial cells and the integrity of spheroid is not easy to be destroyed. At the final stage, spheroid becomes very compact and robust. The different layers in spheroid are easily observed. There are individual cells bulging on the periphery of the spheroid, representing the proliferation.

Figure 24A shows the growth curve of MDA-MB-231 spheroids by diameters at different seeding densities for 12 days. All spheroids initially grew rapidly and sequentially reached a plateau. The plateau appeared according to the seeding density, the higher the seeding density the faster the plateau appeared. Spheroids with high seeding density (6000 cells) reach the plateau after 5 days and with low density (1000 cells) on day 11.

Moreover, despite the different seeding densities, spheroids eventually stopped increasing the size at the diameters of 700 μm to 800 μm , suggesting the limitation of spheroid growth. This observation is also captured on other researches about the growth curve of spheroids [162, 163].

Afterward, all spheroids have a slight increase of the size after reaching the growth

limitation. It is because they lose the compact structure and integrity due to the lack of nutrient, therefore the disaggregation of spheroids appears. Without changing the medium, spheroids started disaggregating after 11 or 12 days. Instead, spheroids have longer living time with regular medium change [162].

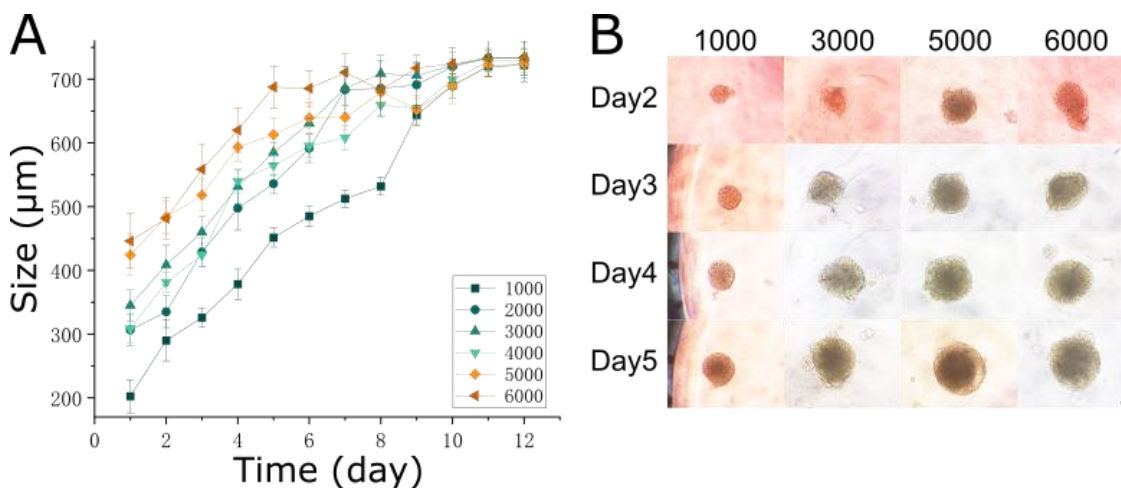


Figure 24: Proliferation of MDA-MB-231 spheroids in different seeding densities from 1000 to 6000 cells per well. A: spheroid growth curves in different seeding densities, all values were expressed as mean diameter \pm SD (n = 3). B: size and internal layered distribution of spheroids in different seeding densities on different day. Scale bar represents 100 μ m.

In addition, with the expansion of spheroid, the internal layered cell distribution started appearing when the diameter reached 400 μ m, which is correlated to the solid tumor *in vivo* [164]. High seeding density such as 5000 and 6000 cells generate big spheroids (diameter > 400 μ m) on the first day. However, the internal layered cell distribution was not observed on day 1 (Figure 24B). It is because the gradient of nutrients and waste accumulation is not yet generated. The different layered structure was observed on day 2 and day 3 on the spheroids at 5000 and 6000 seeding density, respectively. Spheroids with middle seeding density of 3000 and 4000 cells pass the diameter line of 400 μ m on day 3, the necrotic zone and quiescent zone occurs on the same day. Spheroids with a low seeding density from 1000 to 3000 cells reach the diameter of 400 μ m on day 5 and day 4, respectively. As illustrated on Figure 24B, the necrotic core in spheroid generated on day 5, which is corresponding to the increasing of the size. The spheroids reach the plateau at around 700 μ m diameter and stops visible growth on day 11 and 9, respectively.

Additional, it was observed that spheroids from day 5 to day 8 show slow and stable growth speed on both high seeding density (6000 cells) or low seeding density (1000 cells), this slow and stable generation speed provides a good platform for cell culture experiment. Therefore, the spheroids experiments in this study were performed on low seeding density (1000 cells) spheroids within these days.

3.2.3 Spheroids fusion experiment

Two 4-day-old spheroids at seeding density of 2000 cells were chosen to investigate the interaction between spheroids for 6 days (Figure 25). Both spheroids' diameters are over 400 μm and both contain necrotic zones.

In the 6 days observation, two spheroids fused from the first day and eventually became to one big spheroid.

On the first day, cells in the rim tend to process the first interaction of the two spheroids and the connection is limited in the proliferating zone. However, the shapes of both spheroids were clear and easily distinguished. On the next day, two spheroids merged deep from the proliferating zone to the quiescent zone. The periphery of two spheroids is well merged and formed a neck shape at the connection part. Pipetting was not able to separate them.

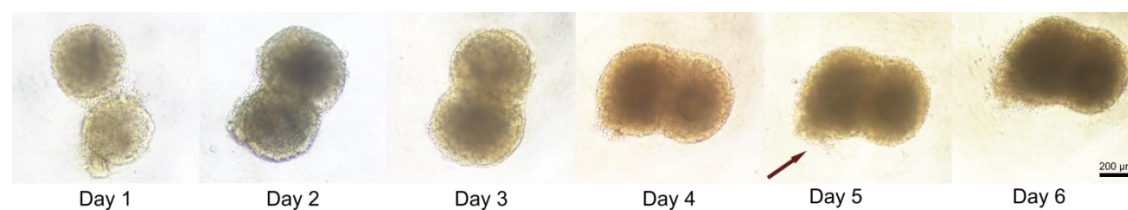


Figure 25: The fusion process of two MDA-MB-231 spheroids over 6 days. Two spheroids with seeding density of 2000 cells on day 4 were incubated together for the spheroids' fusion experiment. The spheroid started disaggregation on day 5 (arrow). Scale bar represents 200 μm .

The proliferating zones were completely merged on the third day, and the two spheroids formed an oval shape as one big spheroid with two necrotic zones on the fourth day. The sizes of the quiescent zone and the necrotic zone were increasing during the merging. After 5 days, the merged spheroid tends to disaggregate from the periphery due to the lack of the nutrient (Figure 25 arrow); cells in the proliferating zone tend to lose the connection with the spheroid, the shape of the cells is easily

recognized. It was observed on day 6 that the necrotic zones from the original spheroids fused together. The neck shape was barely seen, hence, the two spheroids eventually merged into one spheroid. The spheroid kept disaggregating and more cells disconnected with the spheroid are observed in the medium.

The spheroids fusion experiment opens a window of cell research. The fusion phenomenon is observed not only from the same cell line but also from different cell types [165, 166]. The fused spheroids from different cell types mimic the tissues *in vivo* which are composed of multiple cell types in multicellular organisms. It would be a great platform for the further research of reproduction of native tissue *in vitro*. The artificial reconstitution of native tissues can be precise controlled and built in healthy and disease state as desired.

Tumor spheroid can also be co-cultivated with other cell types, for example with the patient derived immune cells from peripheral blood. The additional immune cells bring the opportunity of further study about the interaction between two cell types and individual therapeutic approaches to intensify the antitumor immune response [167]. It is possible to mimic the tumor immune microenvironment (TIME) *in vivo* by adjusting the ratio of immune cells and tumor cells. Therefore the combination of chemotherapy and immunotherapy can be well investigated, which is great potential for improving personalized therapeutic strategies.

3.2.4 3D cell viability assay

3D cell viability assay is based on measuring the quantity of the present ATP, demonstrating the presence of metabolically active cells in the spheroid. The strong lytic capacity of the reagent provides high penetration into the spheroids, resulting cell lysis and luciferase reaction. The luminescent signal is generated proportional to the amount of ATP present, suggesting the cell viability of the spheroid.

3D cell viability of MDA-MB-231 spheroids after the treated with DOX-TSL was analyzed in order to evaluate the therapeutic efficiency. Spheroids were incubated with different concentrations of DOX-TSL for 4 hours at 37 °C or 3 hours at 37 °C

followed by 1 hour at 40 °C, representing at the normal physiological condition or the thermal therapeutic condition, respectively. After 24 hours or 48 hours further incubation in fresh DMEM/NEA medium at 37 °C, the 3D cell viability assay was performed.

As seen in Figure 26, the effectiveness of the DOX-TSL treatment under mild hyperthermia is time and dose dependent. At physiological condition, the half maximal inhibitory concentration (IC_{50}) was obtained at $171.07 \pm 26.58 \mu\text{g/mL}$ for 24 hours. With mild hyperthermia treatment at 40 °C, the IC_{50} of DOX-TSL dropped to $101.24 \pm 12.75 \mu\text{g/mL}$ after 24 hours and at $4.94 \pm 5.73 \mu\text{g/mL}$ after 48 hours. This observation demonstrates that the dose dependent effect is correlated with temperature and time. The IC_{50} value is correlated to the discovery of other researches of DOX formulation on spheroids [136].

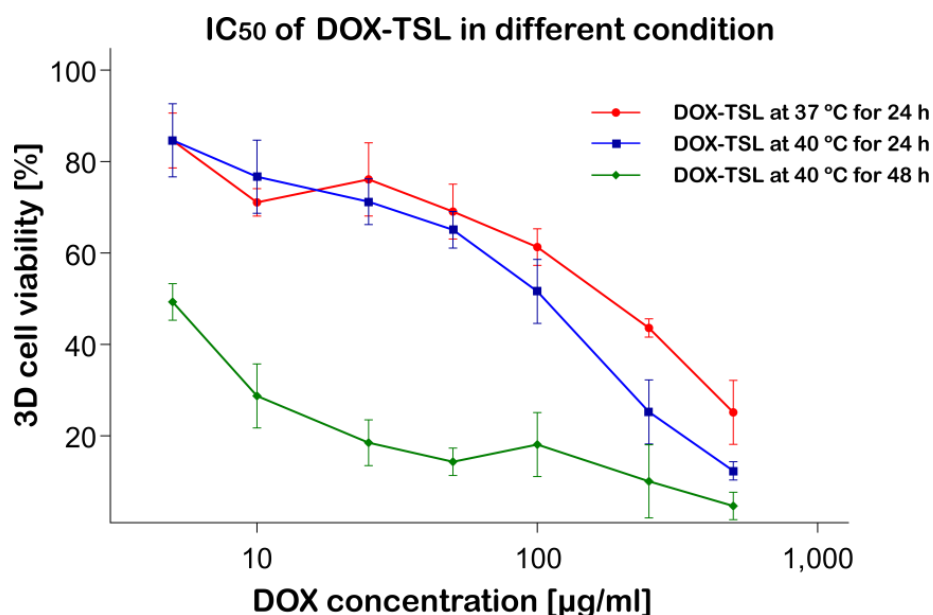


Figure 26: Relative 3D cell viability of MDA-MB-231 spheroids treated with DOX-TSL at 37 °C (red), at 40 °C for 24 hours (blue) and 48 hours (green) at different concentration of doxorubicin (DOX). All measurements were performed in triplicates and values were expressed as mean \pm SD ($n = 3$).

The IC_{50} of DOX on 3D cell culture is much higher than on 2D cell culture [168]. It is because of the nature layered structure of spheroid. Hypoxia and lactose accumulation occur inside of the spheroid due to the nutrient penetration and waste transport gradients, so that the spheroid's interior holds an oxygen-deficient acidic environment [169]. Generation of reactive oxygen species (ROS) is one of the main

activity mechanisms of DOX on tumor cells which requires the presence of molecule oxygen. Specifically, DOX is converted to semiquinone which generates ROS by reacting with molecule oxygen, thereby causing free radical formation and oxidative stress [12].

Therefore, the hypoxic condition would compromise the efficiency of DOX inside the spheroids.

However, the opposite situation appears in 2D cell culture. Cells without the oxygen gradient are all sufficiently oxygenated, which allows the rapid generation of ROS when exposed to DOX. Therefore, the IC_{50} of DOX-TSL on spheroids is much higher than on 2D cell culture.

Afterwards, we investigate the efficacy of 250 $\mu\text{g}/\text{mL}$ empty TSL, DOX-TSL and free DOX on spheroids at physiological condition (37 $^{\circ}\text{C}$) and mild hyperthermia (40 $^{\circ}\text{C}$, 41 $^{\circ}\text{C}$ or 42 $^{\circ}\text{C}$). Spheroids were incubated with different samples for 4 hours at 37 $^{\circ}\text{C}$ or 3 hours at 37 $^{\circ}\text{C}$ followed by thermal therapy for 1 hour. Afterwards the samples were replaced by fresh medium and incubated at 37 $^{\circ}\text{C}$ for another 24 hours.

As shown in Figure 27A, the spheroids remained over 95% cell viability at both 37 $^{\circ}\text{C}$ and 40 $^{\circ}\text{C}$ after the treatment with empty TSL. This result, as expected, illustrates that empty TSL does not have significant damage on spheroids.

With DOX-TSL, the result becomes temperature dependent. At 37 $^{\circ}\text{C}$ a 3D cell viability of 68.79% was observed, while it dropped to 32.27 % at 40 $^{\circ}\text{C}$. At 37 $^{\circ}\text{C}$, only small amount of DOX works on the spheroids, and most DOX-TSL remained the integrity, encapsulating DOX inside the DOX-TSL so that it does not bring damage to the spheroid. While at 40 $^{\circ}\text{C}$, DOX-TSL comes to an environment which is over its phase transition temperature. Here the lipid bilayer of DOX-TSL becomes more permeable since lipid membranes transfer from liquid condensed phase (L_{β}) to liquid expanded phase (liquid-phase, L_{α}). Hence, the encapsulated DOX can be released and reach the tumor cells, through several mechanism such as intercalate the helices and inhibit the synthesis of DNA, RNA and proteins, thus leads to cell death. Therefore,

tumor spheroids under mild hyperthermia received significant damage from DOX-TSL.

Spheroids treated with free DOX show low cell viability at both 37 °C (35.52%) and 40 °C (19.77%). Unlike DOX-TSL, free DOX as small molecule permeates the phospholipid bilayer membrane of cancer cells via passive diffusion with ease [12].

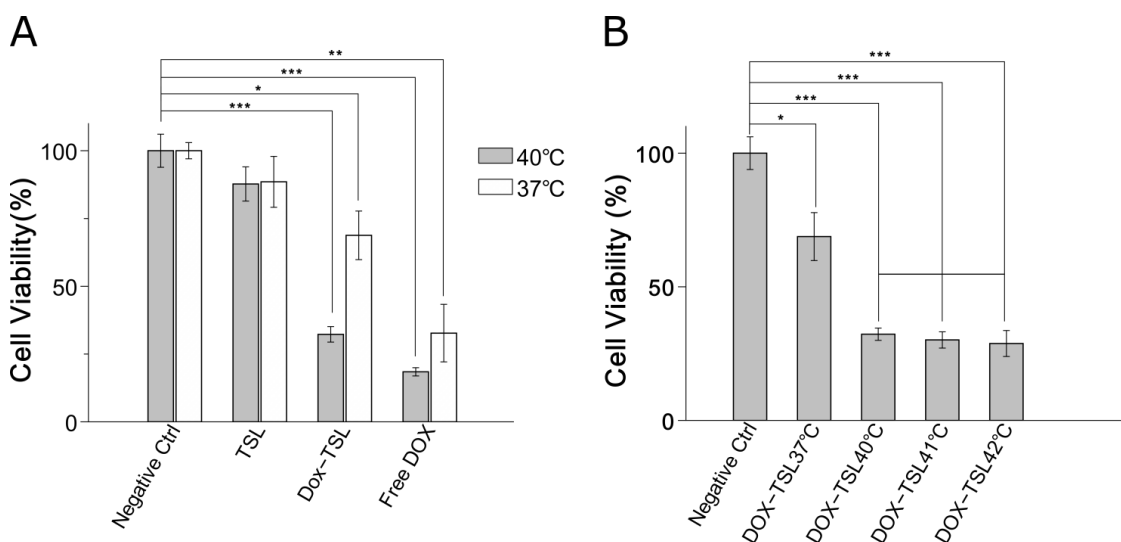


Figure 27: A: Relative 3D cell viability of MDA-MB-231 treated with TSL, DOX-TSL and free DOX at different temperature (37 °C and 40 °C). B: 3D cell viability of MDA-MB-231 treated with DOX-TSL at different temperature (37 °C, 40 °C, 41 °C and 42 °C). All measurements were performed in triplicates and values were expressed as mean \pm SD (n = 3). Statistical differences are denoted as [*] $p < 0.05$, [**] $p < 0.01$, [***] $p < 0.001$

However, the cytotoxicity of free DOX is slightly higher at 40 °C than at 37 °C, suggesting mild hyperthermia perhaps facilitates free DOX treatment on spheroids. The gradient of nutrient and drug penetration in spheroids is likely undergoing slight modifications at higher temperatures so that larger amount of free DOX could penetrate into the inner layer of spheroids. The influence of temperature on spheroid generation and function can be further investigated. Another possibility is that elevated temperature accelerates cell death of quiescent cells through apoptosis or necrosis.

Besides, the cell viability of free DOX at 37 °C and DOX-TSL at 40 °C show similar results, 35.52% and 32.27%. It suggests that most DOX-TSL has been trigger released at 40 °C and the released DOX were mostly taken up by the spheroids.

The 3D cell viability assay legibly explained the efficiency of DOX-TSL at different conditions. The integrity of the formulation remains intact at normal physiological temperature (37 °C) and gets destroyed at mild hyperthermia (over 40 °C).

To further investigate the cytotoxicity of DOX-TSL at different mild hyperthermia temperatures, the thermal treatment was performed at 40 °C, 41 °C and 42 °C. The 3D cell viability of 30.12% at 41 °C and 28.98% at 42 °C was observed, respectively (Figure 27B). There were slight but not significant differences of DOX-TSL efficiency at 40 °C, 41 °C and 42 °C thermal treatment. Thus 40 °C was chosen for the further experiments, which is friendly to patients' pain tolerance.

Furthermore, when 40 °C is applied on the targeted tumor site, the untargeted healthy adjacent tissue would not be over heated as if higher temperature is applied. So that the liposomes remain the intact structure thereby limiting the undesired side effects to patients.

3.2.5 Live/dead stain assay

Live/dead staining assay was performed to visualize the inner layered structure of the spheroid and the efficiency of DOX-TSL. Mature spheroids were stained by calcein AM and PI which show live and dead cells, respectively. PI as a nuclei staining dye, can reach the nucleus by passing through disordered areas of dead cell membranes, but cannot be able to reach the viable cell membrane. While in the live cells, the non-fluorescent calcein AM can be converted to green fluorescent calcein with the present of esterase, which is absent in dead cells.

As seen in Figure 28, a 5-day-old MDA-MB-231 spheroid with seeding density of 1000 cells was stained by calcein AM and propidium iodide (PI) representing live cells and dead cells, respectively. The images were captured by light-field microscopy and confocal laser scanning microscopy. PI signal (red) occurs mainly in the core of the spheroid, representing the necrotic zone. The green dye stained all over the proliferating zone, especially on the rim of the spheroid. Meanwhile, in quiescence zone, a weaker calcein fluorescence signal was observed. This is probably due to the

less amount of esterase in quiescence cells by the slow metabolic speed. The distribution of spheroid's inner layers is corresponding to the image of light field microscopy.

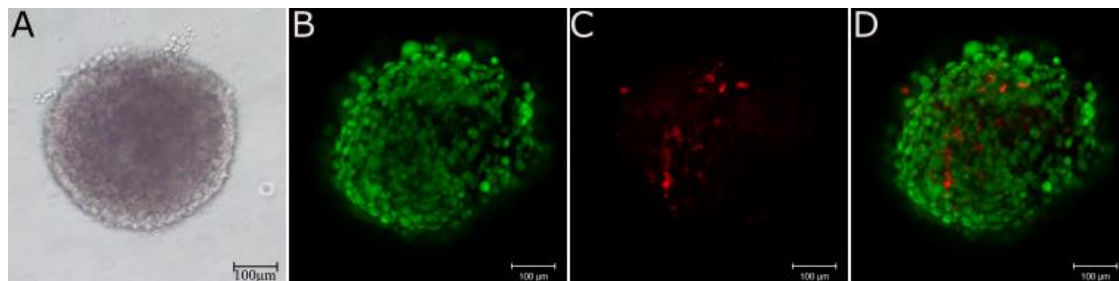


Figure 28: Structure of 1000 cells seeded MDA-MB-231 spheroid on day 5 under light-field microscopy (A). Calcein AM stained (B), propidium iodide (PI) stained (C) spheroid and merged (D) under the confocal laser scanning microscope. Green color indicates the live cells which were labeled by Calcein AM, and red indicates dead cells which were labeled by propidium iodide (PI). Scale bar represents 100 μm .

To visualize the efficiency of DOX-TSL after thermal treatment, after 24 hours the MDA-MB-231 spheroids were stained by calcein AM and PI. Images were captured by confocal laser scanning microscope (CLSM) (Figure 29). Spheroids treated with DOX-TSL showed temperature depended result as observed on 3D cell viability assay. At 37 $^{\circ}\text{C}$, sparse PI signal was captured on the spheroid. The increase of the PI signal compares to it on the controlled spheroid, suggesting some cytotoxicity from DOX-TSL treatment. As known from the drug release assay, DOX was released more under acidic condition than at pH 7.4 condition. This unexpected cytotoxicity from DOX-TSL is possibly due to the acidic environment in the spheroid. However, the major cytotoxicity of DOX-TSL does not occur at 37 $^{\circ}\text{C}$. Significant increase of PI signal and decrease of calcein AM signal was observed on the spheroid treated at 40 $^{\circ}\text{C}$ (Figure 29C), meaning more dead cells and less alive cells were captured after this treatment. This observation demonstrates that DOX-TSL treatment at 40 $^{\circ}\text{C}$ provides more cytotoxicity than at 37 $^{\circ}\text{C}$, which is corresponding to the result of 3D cell viability assay. When the temperature is beyond the T_m of DOX-TSL, the encapsulated DOX can be rapidly released and interact with the tumor spheroids. Furthermore, the primary increased PI-stained dead cells are located on the proliferating zone. This

demonstrates that cells in this area have the priority to take up DOX through passive diffusion principal of nutrients and drugs. Similarly, as the distance between cells and the periphery of spheroid increases, the diffusion of DOX gradually decreases. Thus on the CLSM images, the PI signal representing dead cells does not show significant increase in the inner layer as much as the outer layer of the spheroid.

Spheroids treated with free DOX at 37 °C and 40 °C were shown on Figure 29D and Figure 29E. Deeper PI signal was observed in the inner layer of spheroid treated at 40 °C compare to the spheroid treated at 37 °C. In quiescent zone the PI-stained dead cells were captured as well. This observation suggests that more cell death occurs in the inner layer of the spheroid at higher temperature, which is in line with the 3D cell viability result. Furthermore, it reflects from the side that mild hyperthermia facilitates the penetration of drugs into spheroid. This discovery also explains that in 3D cell viability assay, spheroids treated with DOX-TSL at 40 °C showed lower cell viability than treated with free DOX at 37 °C.

Additionally, spheroid treated at 40 °C with free DOX presented the weakest green calcein fluorescence signal, suggesting the same result as in 3D cell viability assay.

3.2.6 Cellular uptake assay

The cellular uptake studies of DOX-TSL and free DOX were performed on MDA-MB-231 spheroids and visualized under the confocal laser microscopy CLSM (Figure 30). To visualize the ability of the drug delivery system to load DOX and exert its cytotoxic effect DOX can be directly observed under the fluorescence microscopy by its fluorescence property. A blue-fluorescent DNA dye DAPI was utilized to stain the nuclei drawing the spheroid's outline.

After 24 hour treatment, spheroids were first fixed by 4% paraformaldehyde and then stained by DAPI. DAPI is an impermeant DNA dye at common experiment condition. However, the integrity of cell membrane is destroyed by paraformaldehyde, so that DAPI can penetrate into the cells and interact with DNA all over the spheroid. Therefore the DAPI fluorescence signal represents the outline of the spheroid.

As seen in Figure 30A, spheroid treated with DOX-TSL at 37 °C showed a very faded red fluorescence signal from DOX, representing a minor release of DOX in the physiological condition. In contrast, the spheroid emits relatively stronger DOX fluorescence signal after the thermal treatment at 40 °C than the spheroid stayed in the physiological condition (37 °C). This observed significant increase in cellular uptake of DOX at 40 °C is correlated to the enhanced DOX release as discussed previously (section 3.1.6 drug release assay). DOX-TSL was triggered release by temperature stimulation and taken up by the spheroids.

DOX signals mainly located in the proliferating zone and quiescent zone of the spheroid (Figure 30B). A vary faded red fluorescence signal was observed in the inner layer of the spheroid. The absence of DOX in the necrotic core of spheroids is due to the difficulty in transporting DOX via passive diffusion. As anticipated, the distribution of DOX in spheroid is correlated to the gradient of drugs and nutrients diffusion.

As shown on Figure 30B and Figure 30C, the spheroid treated with DOX-TSL at 40 °C and the spheroid treated with the same dose of free DOX at physiological condition showed similar cellular uptakes of DOX. It is suggesting that most of the encapsulated DOX are released from DOX-TSL at 40 °C and taken up by the spheroid in this treatment. However, the red signal from free DOX treated spheroid showed less gradient dependence as compare to the one treated with DOX-TSL. Due to the small molecule weight, DOX has a wider path to penetrate inside the spheroid whereas the diffusion of DOX-TSL in spheroid is much more gradient dependent.

Additionally, the cellular uptake of free DOX at different temperatures showed interesting result. From Figure 30C and Figure 30D we can see, free DOX treated spheroid at mild hyperthermia presented a significant enhancement of DOX signal as compare to the one treated at physiological temperature. The enhancement signal is manifested in both strength and the depth of penetration in spheroid. This observation reveals that, the cellular uptake of DOX on spheroid is increased at mild hyperthermia

temperature. Therefore, it is strongly considered that the application of mild hyperthermia on spheroid facilitates the penetration of DOX liposomal formulation into the spheroid.

The 3D cell viability assay and live/dead staining assay results demonstrated that more dead cells were observed on the spheroids treated with free DOX at 40 °C than at 37 °C. These results also confirmed our assumption. The correlation of temperature and the penetration capacity of DOX-TSL can be further investigated with different temperatures to get more detailed knowledge.

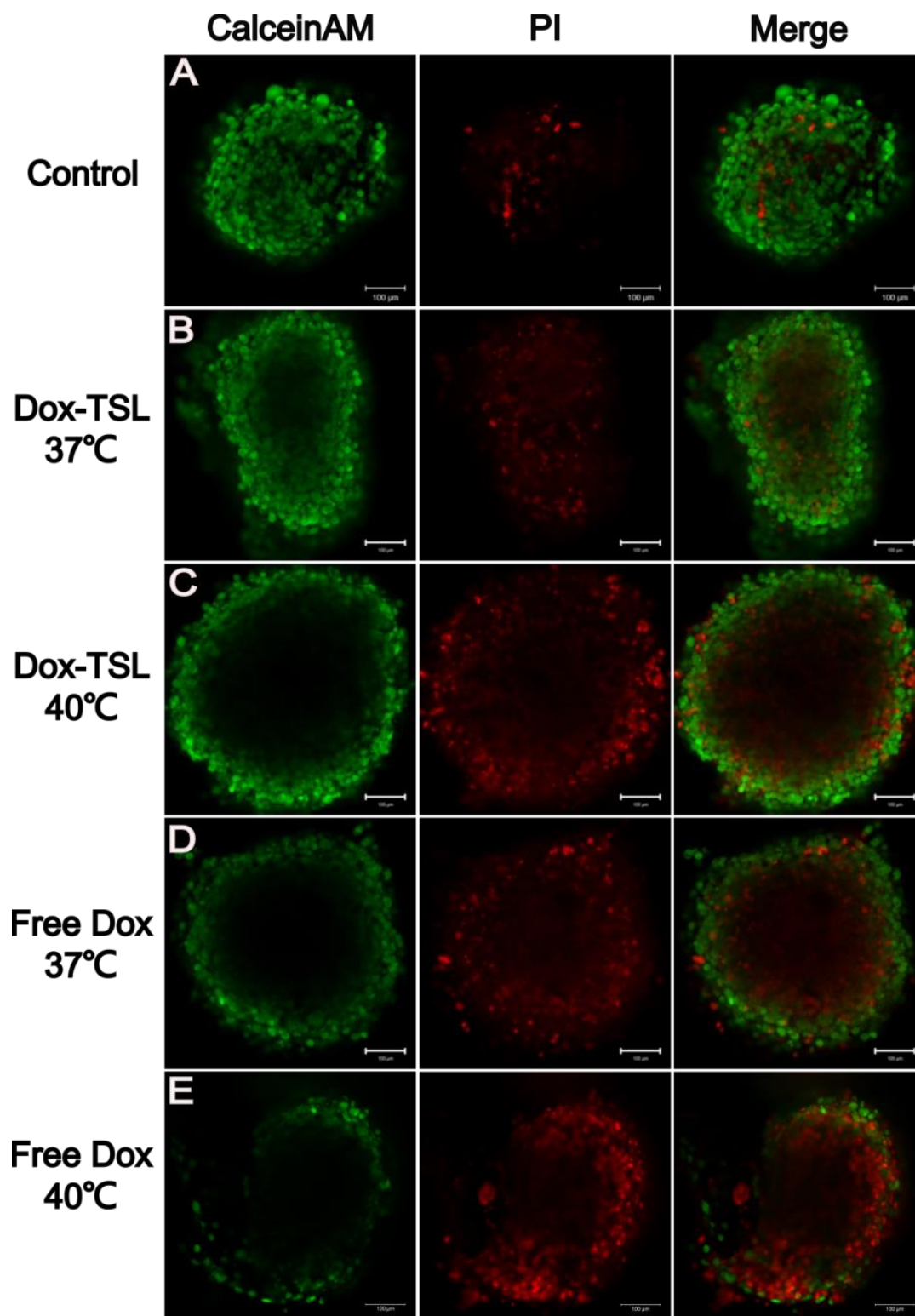


Figure 29: Confocal laser scanning acquisitions of MDA-MB-231 spheroids treated with DOX-TSL or free DOX. The image acquisitions of negative control (A); DOX-TSL for 4 h at 37 °C (B); DOX-TSL for 3 h at 37 °C followed by 1 h at 40 °C (C); free DOX for 4 h at 37 °C (D); and free DOX for 3 h at 37 °C followed by 1 h at 40 °C (E). Green color indicates the live cells which were labeled by Calcein AM, and red indicates dead cells which were labeled by propidium iodide (PI). Scale bar represents 100 µm.

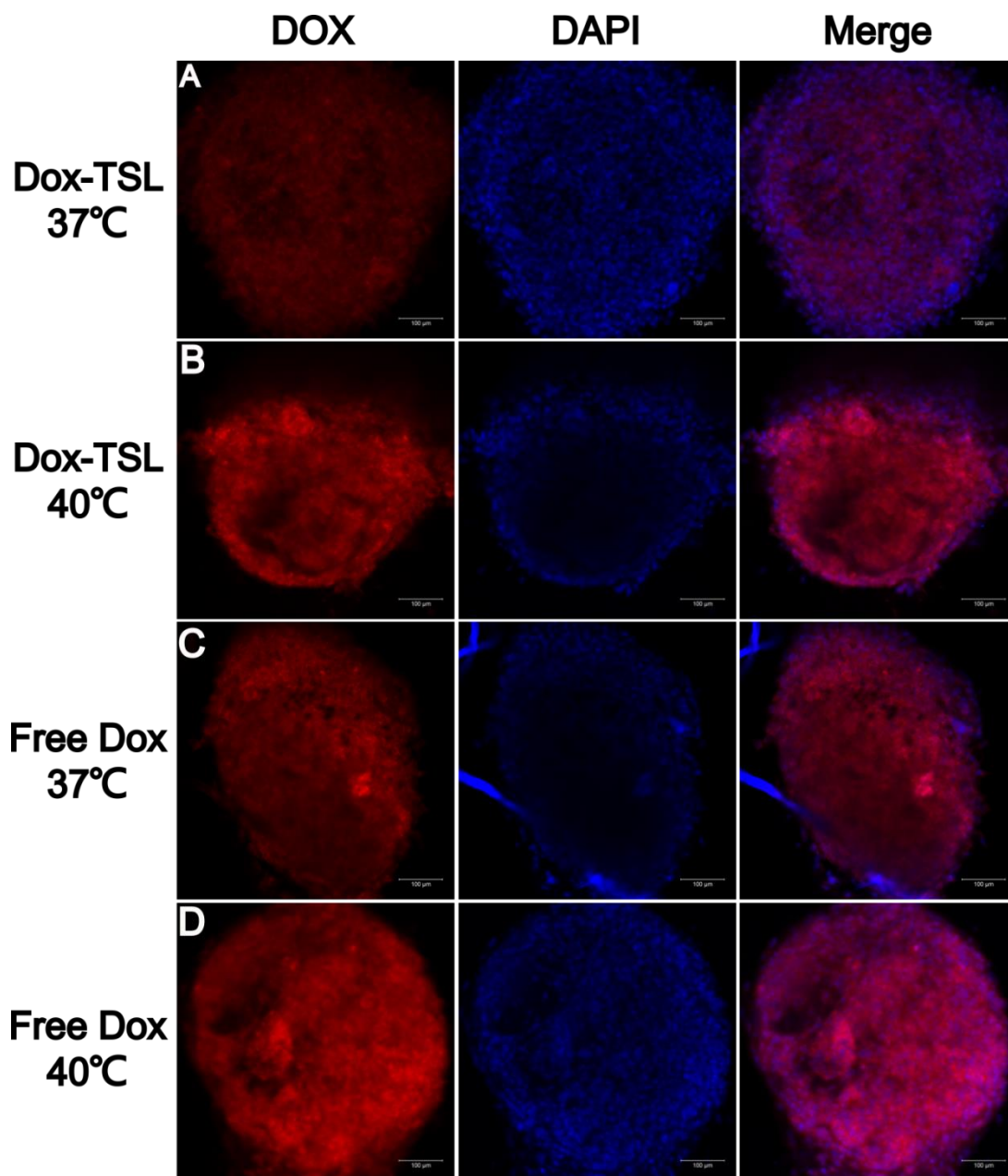


Figure 30: Temperature-dependent confocal laser scanning acquisitions of MDA-MB-231 spheroids treated with DOX-TSL or free DOX. The image acquisitions of DOX-TSL for 4 h at 37 °C (A); DOX-TSL 3 h at 37 °C followed by 1 h 40 °C (B); free DOX for 4 h at 37 °C (C) ; and Free DOX for 3 h at 37 °C followed by 1 h 40 °C (D). DAPI stained nuclei shown in blue, DOX fluorescence in red. Scale bar represents 100 μm .

3.3 Characterization of multifunctional liposome (ICG-DOX-mTSL)

3.3.1 Physicochemical characterization of liposomes

Chemo-photo therapy in cancer treatment has shown great potential in the past years. To combine the chemotherapy and phototherapy effect, a multifunctional liposomal based drug delivery system was designed. It co-encapsulates a NIR dye indocyanine green (ICG) and a first line chemotherapeutic drug doxorubicin (DOX). ICG can be encapsulated simply through the self-assemble mechanism of liposome. The lipophilic part of the ICG molecule associates with the phospholipid bilayer whereas the hydrophilic part either in the aqueous core or on the surface of the liposome [105]. The encapsulation of DOX was achieved by the remote loading via ammonium sulfate concentration gradient between the liposomal interior and the exterior environment as previously described [148,156] (Figure 31).

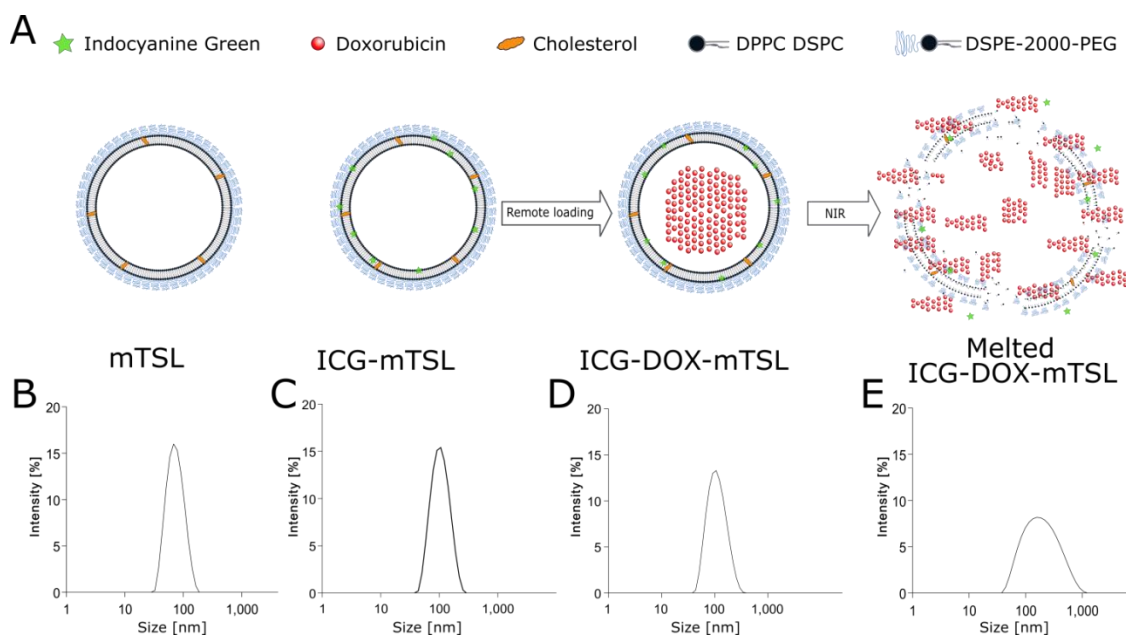


Figure 31: A: Schematic representation of ICG-DOX-mTSL. The mTSL and ICG-mTSL were prepared with thin film hydration method and homogenized by sonication and extrusion. ICG was encapsulated through self-assemble mechanism of liposomes. DOX was encapsulated by remote loading method. NIR irradiation was performed to elevate the temperature over the phase transition temperature (T_m) in order to control release the DOX from liposome. B: DLS size analysis of mTSL. C: DLS size analysis of ICG-mTSL. D: DLS size analysis of ICG-DOX-mTSL. E: DLS size analysis of ICG-DOX-mTSL

after NIR irradiation.

The hydrodynamic diameters of the formulations were determined by Dynamic light scattering (DLS). The obtained size of mTSL shows the mean diameter of 76.70 ± 3.99 nm. Meanwhile, the polydispersity index (PDI) < 0.2 indicates a narrow size distribution of the formulation. The particle size increased upon the encapsulation of ICG and DOX (ICG-mTSL and ICG-DOX-mTSL) to 109.00 ± 17.66 nm and 102.40 ± 11.65 nm, respectively. However, encapsulating ICG does not increase but even decrease the PDI value (0.19 to 0.12), suggesting that ICG encapsulated in the phosphobilayer enhances the homogeneity of the formulation. After encapsulating DOX, the PDI appears an increase, and reached 0.2 (Table 5).

As can be seen from Figure 31, B, C and D represent the DSL analysis of mTSL, ICG-mTSL and ICG-DOX-mTSL, respectively. A right shift of the intensity curve of ICG-mTSL and ICG-DOX-mTSL were observed, indicating the increase of the average size. However, the narrow size distribution indicates that drug encapsulation does not interrupt the homogeneity of the formulation. On Figure 31E, the flat and right shifted intensity curve showed the increase of polydispersity index and the average size of the sample, suggesting the deformation of the ICG-DOX-mTSL after irradiation. The size of the ICG-DOX-mTSL lies between 50-150 nm diameters. Liposomes in this range are able to preferentially penetrate into the tumor site via EPR effect. The liposomal opsonization and clearance of reticuloendothelial system (RES) is reduced by the PEGylation of the formulation. Therefore, the circulation time of the formulation is prolonged. The zeta potential decreased from mTSL (-28.30 ± 9.55 mV) to ICG-mTSL (-31.00 ± 2.76 mV) due to the negative charge carried by ICG. The increase of the zeta potential from ICG-mTSL (-31.00 ± 2.76 mV) to ICG-DOX-mTSL (-18.00 ± 8.12 mV) is attributed to the positively charged DOX (Table 5).

3.3.2 Encapsulate efficiency (EE %)

3% ICG (w/w) was loaded through self-assemble mechanism of the liposome. During

the evaporation of thin lipid film method, ICG located in the lipid bilayer of the liposomes by its amphiphilic characterization.

DOX was loaded into the liposomes by ammonium sulfate gradient remote loading method at the lipid: DOX ratio 5:1. This method relied on the driving force of loading amphipathic weak alkaline drug such as DOX which was firstly reported by Bahrenholz [47].

Table 5: Physiochemical properties of mTSL, ICG-mTSL and ICG-DOX-mTSL. Hydrodynamic diameter (Diameter), polydispersity index (PdI), zeta potential (zP), encapsulation efficiency (EE %). The hydrodynamic diameter is expressed as a measure of particle size distribution by intensity (mean \pm SD, n = 3).

	Diameter \pm SD [nm]	PdI \pm SD	zP \pm SD [mV]	EE \pm SD [%]
mTSL	76.70 \pm 3.99	0.19 \pm 0.03	-28.30 \pm 9.55	--
ICG-mTSL	109.00 \pm 17.66	0.12 \pm 0.02	-31.00 \pm 2.76	ICG: 65.90 \pm 1.89 (ICG:lipid 3:100) (w/w)
ICG-DOX-mTSL	102.40 \pm 11.65	0.20 \pm 0.04	-18.00 \pm 8.12	ICG: 63.50 \pm 5.43 (ICG:lipid 3:100) (w/w) DOX: 64.58 \pm 4.89 (DOX: lipid 1:5) (w/w)

The entrapment efficiency of ICG in ICG-mTSL reached 65.90 \pm 1.89 %. After the co-encapsulation of DOX, a slight decrease from 65.90 \pm 1.89% to 63.50 \pm 5.43% of ICG in ICG/DOX-mTSL was observed. It is assumed that a small amount of ICG was released during ammonium sulfate gradient remote loading of DOX. However, the change is not significant.

The entrapment efficiency of DOX achieved 64.58 \pm 4.89%, which is not as high as previous reports. It is due to a different ratio of DOX and lipid (1:5) was chosen for the remote loading instead of 1:8 or 1:10 in other researches. [170].

The size ranges of the drug-free mTSL and ICG-DOX-mTSL are different, it is assumed that passive loading of ICG and remote loading of DOX increased the size.

The entrapment efficiencies of ICG and DOX in the co-encapsulated liposomal formulation are at acceptable range.

3.3.3 Differential scanning calorimetry (DSC)

DSC was performed to determine the temperature of transforming the lipid bilayer from gel phase to liquid crystalline phase. In order to control release drug at a mild hyperthermia range, the phase transition temperature (T_m) was desired at the range of 40-42 °C. mTSL liposomes were measured in both PBS buffer and citrate buffer as mentioned in section 3.1.3. The lipid composition of DPPC: DSPC: DSPE-mPEG2000: cholesterol with the molar ratios of 75: 15: 5: 5. As shown in Figure 17, the thermosensitive properties of the formulations were first detected at around 38 °C, where the lipid bilayer started the gel to liquid transformation. The transition temperature (T_m) of mTSL was obtained at 41.2 °C in both buffer, suggesting the pH environment does not change the T_m . According to the photothermal property of ICG, 7 minutes of NIR radiation at 808 nm, 500 mW is able to lift the temperature up to 54.5 °C [171]. This high temperature over the T_m of the mTSL shows the ability to break liposomes' integrity, thereby releasing the encapsulated DOX.

3.3.4 Visualization of ICG-DOX-mTSL

Transmission electron microscopy (TEM) (Figure 18A, B, C, and D) and atomic force microscopy (AFM) (Figure 18E, F, G, and H) were chosen to visualize the morphological characteristics of mTSL and ICG-mTSL and ICG/DOX-mTSL.

All liposomes are in round shape and well segregated, which demonstrates homogeneous distribution of the formulations at 37 °C. The diameters of all samples measured by AFM and TEM correspond well with the results of average size by DLS measurements. The height of mTSL, ICG-mTSL and ICG/DOX-mTSL before irradiation was at the range of 9-14 nm. The smooth curves obtained from the cross-sectional profile demonstrate the well-rounded shapes of the plump spherical liposomes. The integrity of ICG/DOX-mTSL is well preserved at the physiological condition (Figure 18I, J, and K).

After irradiation with NIR at 808 nm for 15 min, the deformation of ICG/DOX-mTSL was captured by both AFM and TEM (Figure 18D, H, and L). The photothermal activity of NIR irradiation on ICG/DOX-mTSL allows the liposomal formulation passing through the phase transition temperature. Subsequently the lipid bilayer went through phase change therefore deformed from homogenous individual vesicles to unshaped particles.

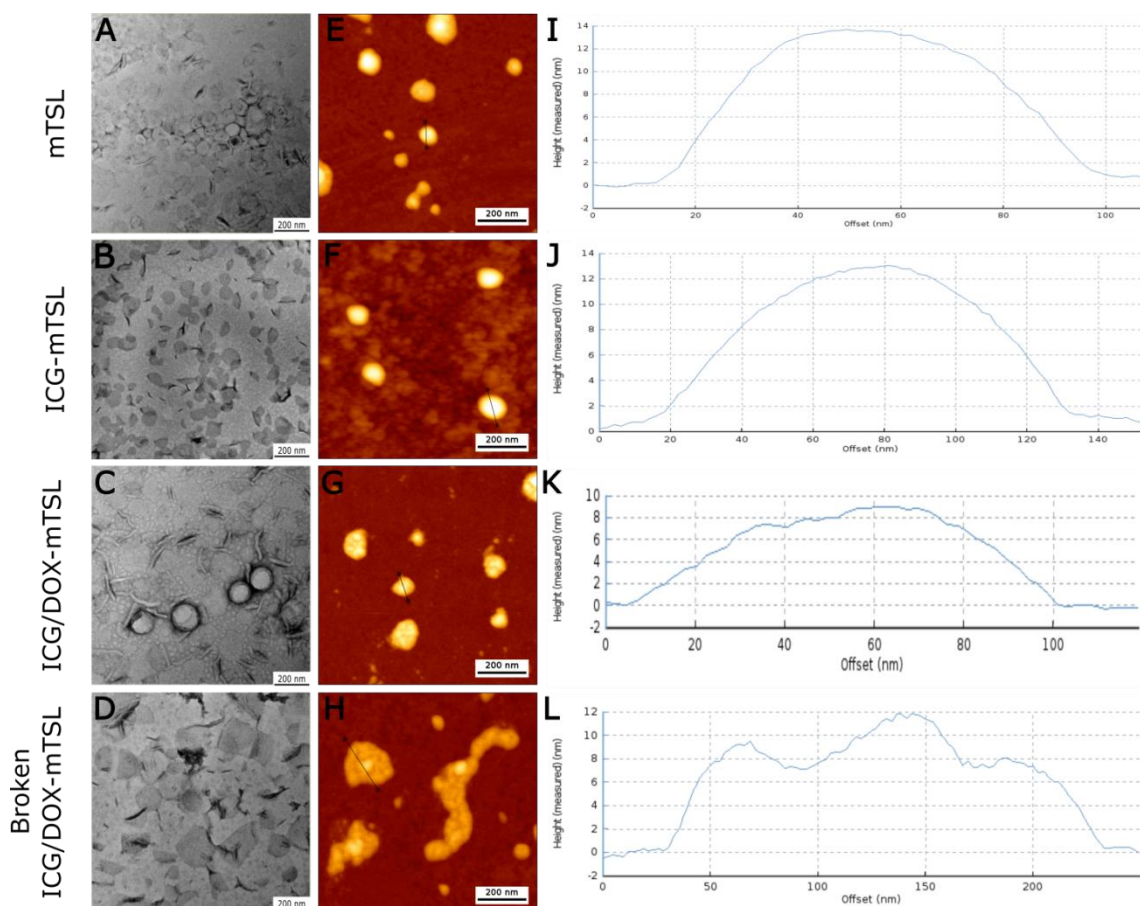


Figure 32: Transmission electron micrographs (TEM) (A, B, C, D) and Atomic force microscopy (AFM) (E, F, G, H) images of mTSL (first line), ICG-mTSL (second line) and ICG-DOX-mTSL before NIR irradiation (third line) and after (last line). I, J, K, and L show the height of the cross-sectional profile along the identified line. Scale bar represents 200 nm.

Furthermore, a significant increase in size of ICG/DOX-mTSL after NIR irradiation is observed by TEM and AFM. This observation also appears on DLS measurements as right shift and flat curve after NIR irradiation (Figure 31E). Liposomes pass through the T_m during the uprising temperature by NIR irradiation, inducing the destruction of its integrity. Whereas the temperature goes down, the lipids tend to restructure inhomogeneous entities.

Additionally, the height of ICG/DOX-mTSL unevenly decreases after NIR irradiation. The rough rugged line from the cross-sectional profile (Figure 18L) showed the uneven decrease of ICG/DOX-mTSL on height after NIR irradiation. Furthermore, some fragments of the phospholipid bilayer can be observed under the TEM (Figure 18D).

4 Summary and outlook

In this dissertation, thermosensitive liposome-based drug delivery systems for anti-cancer therapy were developed and examined on 3D cell culture models. In order to closely mimic solid tumor environments *in vivo*, multicellular tumor spheroids (MCTS) were generated. Spheroids cultivation shows many advantages over conventional 2D cell culture including the 3D architecture, more natural cell morphology, nutrient and drug diffusion gradients, cell-to-cell connections and cell-ECM interactions. It is a promising experimental model between conventional cell culture and animal study. Triple negative breast cancer (TNBC) cell line MDA-MB-231 was chosen for the generation of the spheroids in all experiments in this work. MDA-MB-231 spheroids were generated in agarose coated multi-well plates, and supplemented with collagen I. From internal to external, the spheroid is divided to three zones, i.e. proliferation zone, quiescence zone and necrotic zone.

The first project was concerned with creating thermosensitive liposomes (TSL) and loading them with the first line chemotherapeutic agent doxorubicin (DOX). DOX is one of the most common chemotherapeutic agents for various cancers in clinical therapy. However, pure drug application causes severe side effects, like cardio- and hepatotoxicity which could be reduced by using advanced, biocompatible drug delivery systems, which can deliver DOX directly to the tumor site. For this purpose, thermosensitive liposomes encapsulating DOX named DOX-TSL were produced and characterized. Empty liposomes were prepared by the conventional thin-film hydration method. Afterwards, DOX was encapsulated using the remote loading method which uses an ammonium sulfate gradient between the inside and outside of the liposome. The ultracentrifuge method was chosen for the purification of DOX-TSL.

The dynamic light scattering (DLS) measured the liposomes' hydrodynamic diameters and the zeta potential was determined by laser Doppler velocimetry (LDV). The phase transition temperature (T_m) of the thermosensitive liposomes were measured by differential scanning calorimetry (DSC). The encapsulation efficiency (EE %) of

DOX in the liposomal formulations is determined after purification of unencapsulated DOX using UV-VIS spectrophotometry. The long-term stability in an aqueous medium and short-term stability in a serum-supplemented cell culture medium of DOX-TSL were further analyzed by DLS and LDV to track particle size and zeta potential.

The morphological features of each DOX-TSL formulation were visualized using Atomic Force Microscopy (AFM) and Transmission Electron Microscopy (TEM) both before and after temperature elevation or drug release. The morphological investigations from AFM and TEM images demonstrated a well-separated spherical structure of DOX-TSL. AFM results were comparable to the size distribution obtained by DLS.

The results of DLS and LDV represented a uniform mono-disperse size distribution of DOX-TSL liposomes, which remained its integrity for six weeks in an aqueous storage and 24 hours in a serum-supplemented cell culture medium.

The phase transition temperature (T_m) of DOX-TSL was obtained by differential Scanning Calorimetry (DSC) at 39.8 °C. Therefore, a mild hyperthermia at 40 °C was chosen to trigger the release. Before the temperature elevation above T_m , DOX-TSL showed intact structures, whereas after heating, the integrity of DOX-TSL was destroyed leading to the release of encapsulated DOX, alongside the deformation of the liposome.

DOX-TSL was further applied on MDA-MB-231 spheroids in order to evaluate its efficacy in a 3D cell culture model. The efficacy of DOX-TSL was investigated at the initial temperature of 37 °C and with mild hyperthermia (37, 40, 41 and 42 °C). The quantification was performed using 3D cell viability assay, which was also confirmed and visualized by live/dead staining assay. The temperature-dependent cellular uptake was presented by confocal laser scanning microscopy (CLSM). The increased cytotoxicity of DOX-TSL on spheroids at the elevated temperatures (40, 41 and 42 °C) showed that the efficacy of DOX-TSL is significantly temperature-dependent. The

high viability of spheroids at 37 °C demonstrated the integrity of DOX-TSL under normal physiological conditions, where no DOX is released. Additionally, the cytotoxicity studies suggested that drug penetration on spheroids is temperature dependent. The elevated temperature (40 °C) facilitated the free DOX to penetrate deeper into the quiescence zone compared to 37 °C.

Currently established thermal treatment methods in human body are limited by imprecise heat delivery. Mild hyperthermia applied to the skin surface often cannot avoid temperature-induced cell degradation at the surface and temperature reduction at the tumor site due to heat conduction, especially for the therapy at deeper tumor sites. To overcome this obstacle, photothermal therapy has gained attention to improve the accuracy of the temperature elevation in local applications.

The second project focused on triggering the release the DOX of DOX-TSL using near infrared (NIR) irradiation. In order to make DOX-TSL sensitive to NIR, indocyanine green (ICG) was encapsulated into TSL together with DOX, combining photodynamic therapy (PDT) and chemotherapy. ICG is a nontoxic fluorescent NIR dye and a commonly used clinical agent. As a photosensitizer for (PDT), it can be excited by laser light at 808 nm, leading to the generation of reactive oxygen species (ROS) and thereby inducing cell apoptosis or necrosis. As a photothermal agent for photothermal therapy (PTT), ICG converts absorbed light energy into cytotoxic heat, thereby ablating cells. Due to its longer wavelength, NIR light is capable to achieving a greater penetration depth into the tissue.

The concept of this project is to co-encapsulate ICG and DOX into thermosensitive liposomes producing multifunctional liposome (ICG/DOX-mTSL). When the formulation accumulates in tumor cells, NIR laser irradiates the targeted region in order to activate the PDT and PTT from ICG. The generated heat can raise the temperature above the T_m , triggering the release of the encapsulated DOX at the tumor site. Since the heat is generated directly at the tumor site, the obstacles of accuracy and temperature degradation are overcome.

Due to its amphiphilic (ICG) and hydrophilic (DOX) characteristics, the compounds are encapsulated in the phospholipid bilayer (ICG) and the aqueous core (DOX) of the liposome, respectively. The multifunctional thermosensitive liposomes were produced by thin-film hydration method. ICG was encapsulated into the mTSL via self-assembly followed by purification using size exclusive chromatography. DOX was encapsulated using the “remote loading” method and purified through ultracentrifugation. The physicochemical characterization was again performed by DLS and LDV. The morphological characterization of ICG/DOX-TSL and their changes before and after NIR irradiation (808 nm for 15 minutes) were visualized using AFM and TEM.

ICG/DOX-mTSL exhibited a round and homogenous size distribution. High encapsulation efficiencies of ICG and DOX were obtained. AFM and TEM images showed the morphological changes after NIR irradiation, confirming that NIR irradiation was able to disrupt the integrity of ICG/DOX-mTSL and trigger the release of DOX at the tumor site.

In conclusion, the investigated DOX-containing thermosensitive liposomes showed high efficacy against 3D cell culture as a tumor model. Moreover, the spheroids exhibited their own characteristics regarding drug penetration behavior and temperature-dependent cytotoxicity when treated with DOX-TSL.

After the addition of ICG, the thermosensitive liposomal formulation still maintained its stability in terms of physicochemical properties. The novel drug delivery system with phototherapeutic properties, ICG/DOX-mTSL, is promising to enhance the accuracy of treatment at the target location, and further studies on its efficacy in 3D cell culture models are worthwhile.

To assay the toxicity of ICG/DOX-mTSL under more physiological conditions, future studies could employ the chorioallantoic membrane model (CAM). With the tumor angiogenesis and strong vascularization in CAM, spheroid behavior under *in vivo*-like nutrient and drug gradients could be investigated. Furthermore, parenteral application

via intravenous injection could be feasible, opening a new chapter of drug evaluation on 3D cell culture could be written.

5 Zusammenfassung und Ausblick

In dieser Dissertation wurden thermosensible liposomale Wirkstofffreisetzungssysteme für die Antikrebstherapie entwickelt und an 3D-Zellkulturmodellen untersucht. Um solide Tumorumgebungen *in vivo* möglichst genau zu imitieren, wurden multizelluläre Tumorsphäroide (MCTS) generiert. Die Sphäroidkultivierung bietet viele Vorteile gegenüber herkömmlichen 2D-Zellkulturen wie z.B. eine 3D Zell-Architektur vergleichbar dem eines Tumors, einer natürlicheren Zellmorphologie, Nährstoff- und Arzneimitteldiffusionsgradienten, Zell-Zell-Verbindungen und Zell-ECM-Interaktionen. Es handelt sich um ein vielversprechendes experimentelles Modell was zwischen herkömmlicher Zellkultur und Tierstudie einzuordnen ist. Als Modell wurde die TNBC-Zelllinie MDA-MB-231 für die Generierung der Sphäroide in allen Experimenten in dieser Arbeit ausgewählt. MDA-MB-231 Sphäroide wurden in agarosebeschichteten Mehrwellplatten erzeugt und mit Kollagen I ergänzt. Vom inneren zum äußeren Bereich ist das Sphäroid in drei Zonen unterteilt, nämlich die Proliferationszone, die Ruhezone und die Nekrosezone.

Das erste Projekt befasste sich mit der Erzeugung thermosensitiver Liposomen (TSL) und ihrer Beladung mit dem Chemotherapeutikum Doxorubicin (DOX), einem der am häufigsten verwendeten Chemotherapeutika für verschiedene Krebsarten in der klinischen Therapie. Die Anwendung von reinem DOX führt jedoch zu schweren Nebenwirkungen wie Kardio- und Hepatotoxizität, die durch fortschrittliche, biokompatible Wirkstofffreisetzungssysteme reduziert werden können, welche DOX direkt an den Wirkort-Tumor transportieren können. Zu diesem Zweck wurden thermosensible Liposomen hergestellt, welche DOX enthielten (DOX-TSL). Die Herstellung der leeren Liposomen erfolgte durch die konventionelle Dünnschicht-Hydratationsmethode. Anschließend wurde DOX unter Verwendung der „Remote-Loading“-Verfahrens inkorporiert, welches einen Ammoniumsulfatgradienten zwischen dem Inneren und dem Äußeren des Liposoms zur Realisierung der Beladung verwendet. Für die Abtrennung nicht verkapselten

DOX konnte zur Reinigung der DOX-TSL Liposomen die Ultrazentrifugenmethode verwendet werden.

Mit Hilfe der dynamischen Lichtstreuung (DLS) wurde der hydrodynamische Durchmesser der Liposomen, und das Zetapotential durch Laser-Doppler-Velozimetrie (LDV) bestimmt. Die Phasenübergangstemperatur (T_m) der thermosensiblen Liposomen wurde durch Differential-Scanning-Kalorimetrie (DSC) vermessen. Die Einschlusseffizienz (EE %) von DOX in den liposomalen Formulierungen wird nach der Reinigung von unverkapselten DOX mittels UV-VIS-Spektrophotometrie bestimmt. Die Langzeitlagerstabilität in einem wässrigen Medium und die Kurzzeitstabilität in einem Serum-ergänzten Zellkulturmedium von DOX-TSL wurden durch DLS und LDV durch Verfolgung der Teilchengröße und des Zetapotential weiter analysiert.

Die morphologischen Merkmale der einzelnen DOX-TSL Formulierungen konnten mittels Rasterkraftmikroskopie (AFM) und Transmissionselektronenmikroskopie sowohl vor als auch nach der Temperaturerhöhung bzw. der Wirkstofffreisetzung visualisiert werden. Diese morphologischen Untersuchungen aus AFM- und TEM-Bildern zeigten eine gut getrennte, kugelförmige Struktur von DOX-TSL. Die AFM-Ergebnisse waren vergleichbar mit der Größenverteilung, die mittels DLS erhalten wurde.

Die Ergebnisse der DLS und LDV Analytik zeigten eine einheitliche mono-disperse Größenverteilung von DOX-TSL Liposomen. Diese blieb für sechs Wochen in einer wässrigen Lagerlösung und für 24 Stunden in einer mit Serum angereicherten Zellkulturmedium erhalten.

Die Phasenübergangstemperatur T_m von DOX-TSL Liposomen wurde mittels DSC bei 39,8 °C bestimmt. Aus diesem Grund wurde eine leichte Hyperthermie bei 40 °C zur Auslösung der Freisetzung gewählt. Vor Erhöhung der Temperatur über T_m zeigte DOX-TSL intakte Strukturen, während nach Erwärmung die Integrität von DOX-TSL zerstört wurde. Zeitgleich mit der Verformung des Liposoms kam es zur Freisetzung

des eingekapselten DOX.

DOX-TSL wurde weiterhin auf MDA-MB-231 Sphäroiden angewendet, um deren Wirksamkeit in einem 3D-Zellkulturmodell zu bewerten. Die Effizienz der Formulierung auf die Modellzellkulturen ist bei Ausgangstemperatur 37 °C und mit leichter Hyperthermie (40, 41 und 42 °C) oberhalb der T_m untersucht worden. Die Quantifizierung erfolgte mittels 3D-Zellviabilitätstests, welche auch durch Live/Dead-Färbetest bestätigt und visualisiert wurde. Die temperaturabhängige zelluläre Aufnahme wurde durch konfokale Laserscanning-Mikroskopie (CLSM) dargestellt. Die erhöhte Zytotoxizität von DOX-TSL auf Sphäroide bei erhöhten Temperaturen (40, 41 und 42 °C) zeigte, dass die Wirksamkeit von DOX-TSL deutlich temperaturabhängig ist. Die hohe Lebensfähigkeit von Sphäroiden bei 37 °C zeigte die Integrität von DOX-TSL Liposomen unter normalen physiologischen Bedingungen, da hier kein DOX freigesetzt wird. Zusätzlich konnte aus den Zytotoxizitätsstudien geschlossen werden, dass die Penetrationsfähigkeit von Medikamenten auf Sphäroiden temperaturabhängig ist. Die erhöhte Temperatur (40 °C) ermöglichte es dem freiem DOX, tiefer in die Ruhezone einzudringen als bei 37 °C.

Derzeit etablierte thermische Behandlungsmethoden im menschlichen Körper sind durch ungenaue Wärmeabgabe begrenzt. Eine leichte Hyperthermie, welche auf der Haut angewendet wird, kann aufgrund von schlechten Wärmeleitung oft keine Temperatur bedingte Zelldegradation an der Oberfläche vermeiden, insbesondere bei intensiver Applikation zur Therapie tieferer Tumorstäten. Um dieses Hindernis zu überwinden, erhielt die photothermische Therapie Aufmerksamkeit, um die Genauigkeit der Temperaturerhöhung bei lokaler Anwendung zu verbessern.

Das zweite Projekt befasste sich mit der Auslösung der DOX-TSL-Medikamentenfreisetzung unter Verwendung von Nahinfrarot (NIR)-Bestrahlung. Um DOX-TSL Liposomen für NIR sensibel zu machen, wurde Indocyaningrün (ICG) zusammen mit DOX in die TSL eingeschlossen, was die

Phototherapie und die Chemotherapie kombiniert. ICG ist ein ungiftiger fluoreszierender NIR-Farbstoff und ein häufig verwendetes klinisches Diagnostikum. Als Photosensitizer für die photodynamische Therapie (PDT) kann er durch Laserlicht bei 808 nm angeregt werden, was zur Erzeugung reaktiver Sauerstoffspezies (ROS) und dadurch zur Zellapoptose oder -nekrose führt. Als photothermischer Wirkstoff für die photothermische Therapie (PTT) wandelt ICG die absorbierte Lichtenergie in zytotoxische Wärme um und zerstört dadurch Zellen. Das NIR-Licht ist aufgrund seiner langen Wellenlänge in der Lage, eine größere Eindringtiefe in das Gewebe zu erreichen.

Das Konzept dieses Projekts besteht daher darin, ICG und DOX in thermosensiblen Liposomen einzuschließen und so multifunktionale Liposomen (ICG/DOX-mTSL) herzustellen. Wenn die Formulierung in den Tumorzellen angesammelt wird, bestrahlt der NIR-Laser die Zielregion, um die PDT und PTT von ICG zu aktivieren. Die erzeugte Wärme kann die Temperatur über die T_m erhöhen und so die Freisetzung des eingeschlossenen DOX an der Tumorstelle auslösen. Da die Wärme direkt an der Tumorstelle erzeugt wird, werden die Hindernisse der Genauigkeit und Temperaturdegradation überwunden.

Aufgrund ihrer amphiphilen (ICG) und hydrophilen (DOX) Eigenschaften werden die Verbindungen in der Phospholipid-Doppelschicht (ICG) bzw. im wässrigen Kern (DOX) der Liposomen eingeschlossen. Die multifunktionalen thermosensitiven Liposomen wurden durch die Methode der Filmhydratisierung hergestellt. ICG wird dabei durch Selbstorganisation in die mTSL eingeschlossen, anschließend erfolgt die Reinigung mittels Größenausschlusschromatographie. DOX wurde später durch die Methode der „remote loading“ eingeschlossen, gefolgt von der Ultrazentrifugation zur Reinigung. Die physikochemische Charakterisierung wurde wiederum durch DLS und LDV durchgeführt. Die morphologische Charakterisierung und die Veränderungen von ICG/DOX-TSL wurden vor und nach NIR-Bestrahlung (808 nm für 15 Minuten) mit AFM und TEM visualisiert.

Die ICG/DOX-mTSL waren rund und homogen Größen verteilt. Es wurden gute Verkapselungseffizienzen von ICG und DOX erzielt. Die AFM- und TEM-Bilder zeigten die morphologischen Veränderungen nach NIR-Bestrahlung, die bestätigten, dass NIR-Bestrahlung in der Lage ist, die Integrität von ICG/DOX-mTSL zu zerstören und somit die Freisetzung von DOX am Tumorort auszulösen.

Zusammenfassend wurde dargelegt, dass die untersuchten thermosensitiven Liposomen mit DOX Einschluss, eine hohe Wirksamkeit gegenüber 3D-Zellkulturen als Tumormodell. Außerdem zeigten die verwendeten Sphäroide ihre eigenen Merkmale in Bezug auf das Eindringverhalten des Arzneimittels und die temperaturabhängige Zytotoxizität bei der Behandlung mit DOX-TSL.

Nach Zugabe von ICG waren die thermosensitiven liposomale Formulierungen immer noch stabil hinsichtlich ihrer physiochemischen Eigenschaften. Mit ihren phototherapeutischen Eigenschaften ist das neue Wirkstoffträgersystem ICG/DOX-mTSL vielversprechend, gerade um die Genauigkeit der Behandlung an der Zielstelle zu erhöhen, und es lohnt sich, weitere Studien zur Wirksamkeit an 3D-Zellkulturmodellen durchzuführen.

Um die Effizienz von ICG/DOX-mTSL unter physiologischeren Bedingungen zu testen, könnte zukünftig das Chorioallantoic-Membran-Modell (CAM) verwendet werden. Mit der Tumorangiogenese bzw. der starken Vaskularisierung im CAM könnte man die Sphäroide mit *in vivo* ähnlichen Nähr- und Arzneimittelgradienten untersuchen. Auch eine parenterale Applikation durch eine intravenöse Injektion wäre möglich und es könnte ein neues Kapitel der Arzneimittelbewertung in der 3D-Zellkultur geschrieben werden.

6 Appendix

6.1 References

- [1] N. Harbeck, F. Penault-Llorca, J. Cortes, M. Gnant, N. Houssami, P. Poortmans, K. Ruddy, J. Tsang, F. Cardoso, Breast cancer, *Nat. Rev. Dis. Prim.* 5 (2019) 66. <https://doi.org/10.1038/s41572-019-01111-2>.
- [2] F. Bray, J. Ferlay, R.L. Soerjomataram, Isabelle Siegel, L.A. Torre, A. Jema, Global cancer statistics 2018: GLOBOCAN estimates of incidence and mortality worldwide for 36 cancers in 185 countries, *CA. Cancer J. Clin.* 68 (2018) 394–424. <https://doi.org/10.3322/CAAC.21492>.
- [3] F. Derakhshan, J.S. Reis-Filho, Pathogenesis of triple-negative breast cancer, *Annu. Rev. Pathol. Mech. Dis.* 17 (2021) 181–204. <https://doi.org/10.1146/annurev-pathol-042420-093238>.
- [4] N. Eliyatkin, E. Yalçın, B. Zengel, S. Aktaş, E. Vardar, Molecular classification of breast carcinoma: From traditional, old-fashioned way to a new age, and a new way., *J. Breast Heal.* 11 (2015) 59–66. <https://doi.org/10.5152/tjbh.2015.1669>.
- [5] W.D. Foulkes, I.E. Smith, J.S. Reis-Filho, Triple-negative breast cancer, 2010.
- [6] K.A. Akshata Desai, Triple negative breast cancer – An overview, *Hered. Genet.* 2 (2012) 1. <https://doi.org/10.4172/2161-1041.s2-001>.
- [7] Y.-T. Chou, C.-Y. Lin, J.-W. Wen, L.-C. Hung, Y.-F. Chang, C.-M. Yang, L.-C. Wu, J.-A.A. Ho, Targeting triple-negative breast cancer with an aptamer-functionalized nanoformulation: a synergistic treatment that combines photodynamic and bioreductive therapies., *J. Nanobiotechnology.* 19 (2021) 89. <https://doi.org/10.1186/s12951-021-00786-8>.
- [8] Y.L. Franco, T.R. Vaidya, S. Ait-Oudhia, Anticancer and cardio-protective effects of liposomal doxorubicin in the treatment of breast cancer, *Breast Cancer Targets Ther.* 10 (2018) 131–141. <https://doi.org/10.2147/BCTT.S170239>.
- [9] G. V Echeverria, Z. Ge, S. Seth, X. Zhang, S. Jeter-Jones, X. Zhou, S. Cai, Y. Tu, A. McCoy, M. Peoples, Y. Sun, H. Qiu, Q. Chang, C. Bristow, A. Carugo, J.

- Shao, X. Ma, A. Harris, P. Mundi, R. Lau, V. Ramamoorthy, Y. Wu, M.J. Alvarez, A. Califano, S.L. Moulder, W.F. Symmans, J.R. Marszalek, T.P. Heffernan, J.T. Chang, H. Piwnica-Worms, Resistance to neoadjuvant chemotherapy in triple-negative breast cancer mediated by a reversible drug-tolerant state., *Sci. Transl. Med.* 11 (2019). <https://doi.org/10.1126/scitranslmed.aav0936>.
- [10] T. Safra, F. Muggia, S. Jeffers, D.D. Tsao-Wei, S. Groshen, O. Lyass, R. Henderson, G. Berry, A. Gabizon, Pegylated liposomal doxorubicin (doxil): Reduced clinical cardiotoxicity in patients reaching or exceeding cumulative doses of 500 mg/m², *Ann. Oncol.* 11 (2000) 1029–1033. <https://doi.org/10.1023/A:1008365716693>.
- [11] C. Carvalho, R. Santos, S. Cardoso, S. Correia, P. Oliveira, M. Santos, P. Moreira, Doxorubicin: The good, the bad and the ugly effect, *Curr. Med. Chem.* 16 (2009) 3267–3285. <https://doi.org/10.2174/092986709788803312>.
- [12] S.N. Hilmer, V.C. Cogger, M. Muller, D.G. Le Couteur, The hepatic pharmacokinetics of doxorubicin and liposomal doxorubicin, *Drug Metab. Dispos.* 32 (2004) 794 LP – 799. <https://doi.org/10.1124/dmd.32.8.794>.
- [13] M.M.L. Fiallo, A. Garnier-Suillerot, B. Matzanke, H. Kozlowski, How Fe³⁺ binds anthracycline antitumour compounds. The myth and the reality of a chemical sphinx, *J. Inorg. Biochem.* 75 (1999) 105–115. [https://doi.org/10.1016/S0162-0134\(99\)00040-9](https://doi.org/10.1016/S0162-0134(99)00040-9).
- [14] S.A. Abraham, D.N. Waterhouse, L.D. Mayer, P.R. Cullis, T.D. Madden, M.B. Bally, The liposomal formulation of doxorubicin, *Methods Enzymol.* 391 (2005) 71–97. [https://doi.org/10.1016/S0076-6879\(05\)91004-5](https://doi.org/10.1016/S0076-6879(05)91004-5).
- [15] A. Vigevani, M.J. Williamson, Doxorubicin, *Anal. Profiles Drug Subst. Excipients.* 9 (1981) 245–274. [https://doi.org/10.1016/S0099-5428\(08\)60143-4](https://doi.org/10.1016/S0099-5428(08)60143-4).
- [16] V.G.S. Box, The intercalation of DNA double helices with doxorubicin and nagalomycin, *J. Mol. Graph. Model.* 26 (2007) 14–19.

- <https://doi.org/10.1016/j.jmgm.2006.09.005>.
- [17] K.I. Kiyomiya, S. Matsuo, M. Kurebe, Mechanism of specific nuclear transport of adriamycin: The mode of nuclear translocation of adriamycin-proteasome complex, *Cancer Res.* 61 (2001) 2467–2471. <https://aacrjournals.org/cancerres/article/61/6/2467/508462/Mechanism-of-Specific-Nuclear-Transport-of> (accessed August 12, 2022).
- [18] L.F. Liu, T.C. Rowe, L. Yang, K.M. Tewey, G.L. Chen, Cleavage of DNA by mammalian DNA topoisomerase II, *J. Biol. Chem.* 258 (1983) 15365–15370. [https://doi.org/10.1016/s0021-9258\(17\)43815-4](https://doi.org/10.1016/s0021-9258(17)43815-4).
- [19] K.M. Tewey, T.C. Rowe, L. Yang, B.D. Halligan, L.F. Liu, Adriamycin-induced DNA damage mediated by mammalian DNA topoisomerase II, *Science* (80-.). 226 (1984) 466–468. <https://doi.org/10.1126/science.6093249>.
- [20] N. Ashley, J. Poulton, Mitochondrial DNA is a direct target of anti-cancer anthracycline drugs, *Biochem. Biophys. Res. Commun.* 378 (2009) 450–455. <https://doi.org/10.1016/j.bbrc.2008.11.059>.
- [21] A.R. Eder, E.A. Arriaga, Capillary electrophoresis monitors enhancement in subcellular reactive oxygen species production upon treatment with doxorubicin, *Chem. Res. Toxicol.* 19 (2006) 1151–1159. <https://doi.org/10.1021/tx060083i>.
- [22] M. Tokarska-Schlattner, M. Dolder, I. Gerber, O. Speer, T. Wallimann, U. Schlattner, Reduced creatine-stimulated respiration in doxorubicin challenged mitochondria: Particular sensitivity of the heart, *Biochim. Biophys. Acta - Bioenerg.* 1767 (2007) 1276–1284. <https://doi.org/10.1016/j.bbabi.2007.08.006>.
- [23] J.H. Doroshow, Anthracycline antibiotic-stimulated superoxide, hydrogen peroxide, and hydroxyl radical production by NADH dehydrogenase, *Cancer Res.* 43 (1983) 4543–4551. <http://aacrjournals.org/cancerres/article-pdf/43/10/4543/2413975/cr0430104543.pdf> (accessed August 12, 2022).

- [24] S. Wang, Y. Wang, Z. Zhang, Q. Liu, J. Gu, Cardioprotective effects of fibroblast growth factor 21 against doxorubicin-induced toxicity via the SIRT1/LKB1/AMPK pathway, *Cell Death Dis.* 8 (2017) e3018–e3018. <https://doi.org/10.1038/cddis.2017.410>.
- [25] O. Tacar, P. Sriamornsak, C.R. Dass, Doxorubicin: An update on anticancer molecular action, toxicity and novel drug delivery systems, *J. Pharm. Pharmacol.* 65 (2013) 157–170. <https://doi.org/10.1111/j.2042-7158.2012.01567.x>.
- [26] M.E.R. O'Brien, N. Wigler, M. Inbar, R. Rosso, E. Grischke, A. Santoro, R. Catane, D.G. Kieback, P. Tomczak, S.P. Ackland, F. Orlandi, L. Mellars, L. Alland, C. Tendler, Reduced cardiotoxicity and comparable efficacy in a phase III trial of pegylated liposomal doxorubicin HCl (CAELYXTM/Doxil[®]) versus conventional doxorubicin for first-line treatment of metastatic breast cancer, *Ann. Oncol.* 15 (2004) 440–449. <https://doi.org/10.1093/annonc/mdh097>.
- [27] L. Harris, G. Batist, R. Belt, D. Rovira, R. Navari, N. Azarnia, L. Welles, E. Winer, Liposome-encapsulated doxorubicin compared with conventional doxorubicin in a randomized multicenter trial as first-line therapy of metastatic breast carcinoma., *Cancer.* 94 (2002) 25–36. <https://doi.org/10.1002/cncr.10201>.
- [28] R.B. Weiss, The anthracyclines: Will we ever find a better doxorubicin?, *Semin. Oncol.* 19 (1992) 670–686. <https://europepmc.org/article/med/1462166> (accessed August 3, 2022).
- [29] F. Arcamone, G. Franceschi, S. Penco, A. Selva, Adriamycin (14-hydroxydaunomycin), a novel antitumor antibiotic, *Tetrahedron Lett.* 10 (1969) 1007–1010. [https://doi.org/10.1016/S0040-4039\(01\)97723-8](https://doi.org/10.1016/S0040-4039(01)97723-8).
- [30] J.S. Wefel, R. Lenzi, R. Theriault, A.U. Buzdar, S. Cruickshank, C.A. Meyers, “Chemobrain” in breast carcinoma? A prologue, *Cancer.* 101 (2004) 466–475. <https://doi.org/10.1002/cncr.20393>.
- [31] L. Bigotte, Y. Olsson, Cytofluorescence localization of adriamycin in the nervous system, *Acta Neuropathol.* 58 (1982) 193–202.

- <https://doi.org/10.1007/BF00690801>.
- [32] J. Tangpong, M.P. Cole, R. Sultana, G. Joshi, S. Estus, M. Vore, W. St. Clair, S. Ratanachaiyavong, D.K. St. Clair, D.A. Butterfield, Adriamycin-induced, TNF- α -mediated central nervous system toxicity, *Neurobiol. Dis.* 23 (2006) 127–139. <https://doi.org/10.1016/j.nbd.2006.02.013>.
- [33] A. Gabizon, R. Catane, B. Uziely, B. Kaufman, T. Safra, R. Cohen, F. Martin, A. Huang, Y. Barenholz, Prolonged circulation time and enhanced accumulation in malignant exudates of doxorubicin encapsulated in polyethylene-glycol coated liposomes, *Cancer Res.* 54 (1994) 987 LP – 992. <http://cancerres.aacrjournals.org/content/54/4/987.abstract>.
- [34] A.D. Bangham, M.M. Standish, J.C. Watkins, Diffusion of univalent ions across the lamellae of swollen phospholipids, *J. Mol. Biol.* 13 (1965) 238–252. [https://doi.org/10.1016/S0022-2836\(65\)80093-6](https://doi.org/10.1016/S0022-2836(65)80093-6).
- [35] C. Zylberberg, S. Matosevic, Pharmaceutical liposomal drug delivery: a review of new delivery systems and a look at the regulatory landscape, *Drug Deliv.* 23 (2016) 3319–3329. <https://doi.org/10.1080/10717544.2016.1177136>.
- [36] P. Trucillo, R. Campardelli, E. Reverchon, Liposomes: From bangham to supercritical fluids, *Processes.* 8 (2020) 1–15. <https://doi.org/10.3390/pr8091022>.
- [37] A. Akbarzadeh, R. Rezaei-Sadabady, S. Davaran, S.W. Joo, N. Zarghami, Y. Hanifehpour, M. Samiei, M. Kouhi, K. Nejati-Koshki, Liposome: Classification, preparation, and applications, *Nanoscale Res. Lett.* 8 (2013). <https://doi.org/10.1186/1556-276X-8-102>.
- [38] B. Kneidl, M. Peller, G. Winter, L.H. Lindner, M. Hossann, Thermosensitive liposomal drug delivery systems: state of the art review, *Int. J. Nanomedicine.* 9 (2014) 4387–4398. <https://doi.org/10.2147/IJN.S49297>.
- [39] A.L. Robson, P.C. Dastoor, J. Flynn, W. Palmer, A. Martin, D.W. Smith, A. Woldu, S. Hua, Advantages and limitations of current imaging techniques for

- characterizing liposome morphology, *Front. Pharmacol.* 9 (2018).
<https://doi.org/10.3389/fphar.2018.00080>.
- [40] S. Palchetti, V. Colapicchioni, L. Digiaco, G. Caracciolo, D. Pozzi, A.L. Capriotti, G. La Barbera, A. Laganà, The protein corona of circulating PEGylated liposomes, *Biochim. Biophys. Acta - Biomembr.* 1858 (2016) 189–196. <https://doi.org/10.1016/j.bbamem.2015.11.012>.
- [41] V.P. Torchilin, Immunoliposomes and PEGylated immunoliposomes: Possible use for targeted delivery of imaging agents, *Immunomethods.* 4 (1994) 244–258. <https://doi.org/10.1006/immu.1994.1027>.
- [42] X. Wang, Y. Song, Y. Su, Q. Tian, B. Li, J. Quan, Y. Deng, Are PEGylated liposomes better than conventional liposomes? A special case for vincristine, *Drug Deliv.* 23 (2016) 1092–1100. <https://doi.org/10.3109/10717544.2015.1027015>.
- [43] K.J. Klopfer, T.K. Vanderlick, Isotherms of dipalmitoylphosphatidylcholine (DPPC) monolayers: Features revealed and features obscured, *J. Colloid Interface Sci.* 182 (1996) 220–229. <https://doi.org/10.1006/jcis.1996.0454>.
- [44] M.H. Gaber, K. Hong, S.K. Huang, D. Papahadjopoulos, Thermosensitive sterically stabilized liposomes: formulation and in vitro studies on mechanism of doxorubicin release by bovine serum and human plasma, *Pharm. Res. An Off. J. Am. Assoc. Pharm. Sci.* 12 (1995) 1407–1416. <https://doi.org/10.1023/A:1016206631006>.
- [45] S. Mabrey, J.M. Sturtevant, Investigation of phase transitions of lipids and lipid mixtures by high sensitivity differential scanning calorimetry, *Proc. Natl. Acad. Sci. U. S. A.* 73 (1976) 3862–3866. <https://doi.org/10.1073/pnas.73.11.3862>.
- [46] E.M. Bolotin, R. Cohen, L.K. Bar, N. Emanuel, S. Ninio, Y. Barenholz, D.D. Lasic, Ammonium sulfate gradients for efficient and stable remote loading of amphipathic weak bases into liposomes and ligandoliposomes, *J. Liposome Res.* 4 (1994) 455–479. <https://doi.org/10.3109/08982109409037057>.

- [47] G. Haran, R. Cohen, L.K. Bar, Y. Barenholz, Transmembrane ammonium sulfate gradients in liposomes produce efficient and stable entrapment of amphipathic weak bases, *BBA - Biomembr.* 1151 (1993) 201–215. [https://doi.org/10.1016/0005-2736\(93\)90105-9](https://doi.org/10.1016/0005-2736(93)90105-9).
- [48] Y.M. B., W.J. N., D.W. H., B. Robert, Design of Liposomes for Enhanced Local Release of Drugs by Hyperthermia, *Science* (80-.). 202 (1978) 1290–1293. <https://doi.org/10.1126/science.364652>.
- [49] M.B. Yatvin, H. Mühlensiepen, W. Porschen, L.E. Feinendegen, J.N. Weinstein, Selective Delivery of Liposome-associated cis-Dichlorodiammineplatinum(II) by Heat and Its Influence on Tumor Drug Uptake and Growth, *Cancer Res.* 41 (1981) 1602–1607. <https://aacrjournals.org/cancerres/article/41/5/1602/485411/Selective-Delivery-of-Liposome-associated-cis> (accessed July 29, 2022).
- [50] M. Liu, H. Du, W. Zhang, G. Zhai, Internal stimuli-responsive nanocarriers for drug delivery: Design strategies and applications, *Mater. Sci. Eng. C.* 71 (2017) 1267–1280. <https://doi.org/10.1016/j.msec.2016.11.030>.
- [51] W. Chen, F. Duša, J. Witos, S.K. Ruukonen, S.K. Wiedmer, Determination of the main phase transition temperature of phospholipids by nanoplasmonic sensing, *Sci. Rep.* 8 (2018) 14815. <https://doi.org/10.1038/s41598-018-33107-5>.
- [52] S. Franz é F. Selmin, E. Samaritani, P. Minghetti, F. Cilurzo, Lyophilization of liposomal formulations: Still necessary, still challenging, *Pharmaceutics.* 10 (2018). <https://doi.org/10.3390/pharmaceutics10030139>.
- [53] S.K. Golombek, J.N. May, B. Theek, L. Appold, N. Drude, F. Kiessling, T. Lammers, Tumor targeting via EPR: Strategies to enhance patient responses, *Adv. Drug Deliv. Rev.* 130 (2018) 17–38. <https://doi.org/10.1016/j.addr.2018.07.007>.
- [54] Y. Zhou, J. Kopeček, Biological rationale for the design of polymeric anti-cancer nanomedicines,

- [Http://Dx.Doi.Org/10.3109/1061186X.2012.723213](http://Dx.Doi.Org/10.3109/1061186X.2012.723213). 21 (2013) 1–26.
<https://doi.org/10.3109/1061186X.2012.723213>.
- [55] S.K. Hobbs, W.L. Monsky, F. Yuan, W.G. Roberts, L. Griffith, V.P. Torchilin, R.K. Jain, Regulation of transport pathways in tumor vessels: Role of tumor type and microenvironment, *Proc. Natl. Acad. Sci. U. S. A.* 95 (1998) 4607–4612. <https://doi.org/10.1073/pnas.95.8.4607>.
- [56] F. Yuan, M. Dellian, D. Fukumura, M. Leunig, D.A. Berk, R.K. Jain, V.P. Torchilin, Vascular permeability in a human tumor xenograft: Molecular size dependence and cutoff size, *Cancer Res.* 55 (1995) 3752–3756.
- [57] K. Greish, Enhanced permeability and retention (EPR) effect for anticancer nanomedicine drug targeting., *Methods Mol. Biol.* 624 (2010) 25–37. https://doi.org/10.1007/978-1-60761-609-2_3.
- [58] G. Caracciolo, Liposome-protein corona in a physiological environment: Challenges and opportunities for targeted delivery of nanomedicines, *Nanomedicine Nanotechnology, Biol. Med.* 11 (2015) 543–557. <https://doi.org/10.1016/j.nano.2014.11.003>.
- [59] T.M. Allen, C. Hansen, J. Rutledge, Liposomes with prolonged circulation times: factors affecting uptake by reticuloendothelial and other tissues, *BBA - Biomembr.* 981 (1989) 27–35. [https://doi.org/10.1016/0005-2736\(89\)90078-3](https://doi.org/10.1016/0005-2736(89)90078-3).
- [60] D.D. Lasic, F.J. Martin, A. Gabizon, S.K. Huang, D. Papahadjopoulos, Sterically stabilized liposomes: a hypothesis on the molecular origin of the extended circulation times, *BBA - Biomembr.* 1070 (1991) 187–192. [https://doi.org/10.1016/0005-2736\(91\)90162-2](https://doi.org/10.1016/0005-2736(91)90162-2).
- [61] J.J. Van Middendorp, G.M. Sanchez, A.L. Burrige, The Edwin Smith papyrus: A clinical reappraisal of the oldest known document on spinal injuries, *Eur. Spine J.* 19 (2010) 1815–1823. <https://doi.org/10.1007/s00586-010-1523-6>.
- [62] R.P. Feldman, J.T. Goodrich, The Edwin Smith Surgical Papyrus, *Child’s Nerv. Syst.* 15 (1999) 281–284. <https://doi.org/10.1007/s003810050395>.

- [63] R. W.Y.Habash, D. Krewski, R. Bansal, H.T. Alhafid, Principles, applications, risks and benefits of therapeutic hyperthermia, 2011.
- [64] Z. Behrouzki, Z. Joveini, B. Keshavarzi, N. Eyvazzadeh, R.Z. Aghdam, Hyperthermia: How can it be used?, *Oman Med. J.* 31 (2016) 89–97. <https://doi.org/10.5001/omj.2016.19>.
- [65] G.S. Gazelle, S.N. Goldberg, L. Solbiati, T. Livraghi, Tumor ablation with radio-frequency energy, *Radiology.* 217 (2000) 633–646. <https://doi.org/10.1148/radiology.217.3.r00dc26633>.
- [66] B. Prasad, S. Kim, W. Cho, J.K. Kim, Y.A. Kim, S. Kim, H.G. Wu, Quantitative Estimation of the Equivalent Radiation Dose Escalation using Radiofrequency Hyperthermia in Mouse Xenograft Models of Human Lung Cancer, *Sci. Rep.* 9 (2019). <https://doi.org/10.1038/s41598-019-40595-6>.
- [67] N. Siauve, C. Lormel, Interstitial microwave hyperthermia treatment investigations, in: *J. Phys. Conf. Ser.*, IOP Publishing, 2012: p. 012001. <https://doi.org/10.1088/1742-6596/395/1/012001>.
- [68] T.P. Ryan, C.L. Brace, Interstitial microwave treatment for cancer: historical basis and current techniques in antenna design and performance, *Int. J. Hyperth.* 33 (2017) 3–14. <https://doi.org/10.1080/02656736.2016.1214884>.
- [69] P. Gupta, A. Srivastava, Numerical analysis of thermal response of tissues subjected to high intensity focused ultrasound, *Int. J. Hyperth.* 35 (2018) 419–434. <https://doi.org/10.1080/02656736.2018.1506166>.
- [70] L. Zhu, M.B. Altman, A. Laszlo, W. Straube, I. Zoberi, D.E. Hallahan, H. Chen, Ultrasound Hyperthermia Technology for Radiosensitization, *Ultrasound Med. Biol.* 45 (2019) 1025–1043. <https://doi.org/10.1016/j.ultrasmedbio.2018.12.007>.
- [71] S.K. Sharma, N. Shrivastava, F. Rossi, L.D. Tung, N.T.K. Thanh, Nanoparticles-based magnetic and photo induced hyperthermia for cancer treatment, *Nano Today.* 29 (2019) 100795. <https://doi.org/10.1016/j.nantod.2019.100795>.

- [72] J. Beik, Z. Abed, F.S. Ghoreishi, S. Hosseini-Nami, S. Mehrzadi, A. Shakeri-Zadeh, S.K. Kamrava, Nanotechnology in hyperthermia cancer therapy: From fundamental principles to advanced applications, *J. Control. Release.* 235 (2016) 205–221. <https://doi.org/10.1016/j.jconrel.2016.05.062>.
- [73] S. Ota, Y. Takemura, Characterization of Néel and Brownian Relaxations Isolated from Complex Dynamics Influenced by Dipole Interactions in Magnetic Nanoparticles, *J. Phys. Chem. C.* 123 (2019) 28859–28866. <https://doi.org/10.1021/acs.jpcc.9b06790>.
- [74] S. Hallasch, S. Frick, M. Jung, I. Hilger, How gastrin-releasing peptide receptor (GRPR) and $\alpha\beta3$ integrin expression reflect reorganization features of tumors after hyperthermia treatments, *Sci. Rep.* 7 (2017). <https://doi.org/10.1038/s41598-017-06100-7>.
- [75] E.J. Moon, P. Sonveaux, P.E. Porporato, P. Danhier, B. Gallez, I. Batinic-Haberle, Y.C. Nien, T. Schroeder, M.W. Dewhirst, NADPH oxidase-mediated reactive oxygen species production activates hypoxia-inducible factor-1 (HIF-1) via the ERK pathway after hyperthermia treatment, *Proc. Natl. Acad. Sci. U. S. A.* 107 (2010) 20477–20482. <https://doi.org/10.1073/pnas.1006646107>.
- [76] K.F. Chu, D.E. Dupuy, Thermal ablation of tumours: Biological mechanisms and advances in therapy, *Nat. Rev. Cancer.* 14 (2014) 199–208. <https://doi.org/10.1038/nrc3672>.
- [77] R. Lugano, M. Ramachandran, A. Dimberg, Tumor angiogenesis: causes, consequences, challenges and opportunities, *Cell. Mol. Life Sci.* 77 (2020) 1745–1770. <https://doi.org/10.1007/s00018-019-03351-7>.
- [78] M.R. Horsman, Tissue physiology and the response to heat, in: *Int. J. Hyperth.*, Taylor & Francis, 2006: pp. 197–203. <https://doi.org/10.1080/02656730600689066>.
- [79] C. Viallard, B. Larrivé, Tumor angiogenesis and vascular normalization:

- alternative therapeutic targets, *Angiogenesis*. 20 (2017) 409–426.
<https://doi.org/10.1007/s10456-017-9562-9>.
- [80] H.S. Reinhold, B. Endrich, Tumour microcirculation as a target for hyperthermia, *Int. J. Hyperth.* 2 (1986) 111–137. <https://doi.org/10.3109/02656738609012389>.
- [81] G. Hannon, F.L. Tansi, I. Hilger, A. Prina-Mello, The Effects of Localized Heat on the Hallmarks of Cancer, *Adv. Ther.* 4 (2021).
<https://doi.org/10.1002/adtp.202000267>.
- [82] S.Y. Lee, J.H. Kim, Y.H. Han, D.H. Cho, The effect of modulated electro-hyperthermia on temperature and blood flow in human cervical carcinoma, *Int. J. Hyperth.* 34 (2018) 953–960.
<https://doi.org/10.1080/02656736.2018.1423709>.
- [83] G.A. Koning, A.M.M. Eggermont, L.H. Lindner, T.L.M. Ten Hagen, Hyperthermia and thermosensitive liposomes for improved delivery of chemotherapeutic drugs to solid tumors, *Pharm. Res.* 27 (2010) 1750–1754.
<https://doi.org/10.1007/s11095-010-0154-2>.
- [84] A.S. Mikhail, A. Partanen, P. Yarmolenko, A.M. Venkatesan, B.J. Wood, Magnetic resonance-Guided drug delivery, *Magn. Reson. Imaging Clin. N. Am.* 23 (2015) 643–655. <https://doi.org/10.1016/j.mric.2015.05.012>.
- [85] P. Gabriele, R. Orecchia, R. Ragona, V. Tseroni, G.L. Sannazzari, Hyperthermia alone in the treatment of recurrences of malignant tumors, *Cancer*. 66 (1990) 2191–2195.
[https://doi.org/10.1002/1097-0142\(19901115\)66:10<2191::AID-CNCR2820661025>3.0.CO;2-8](https://doi.org/10.1002/1097-0142(19901115)66:10<2191::AID-CNCR2820661025>3.0.CO;2-8).
- [86] Ó.G. Björnsson, R. Murphy, V.S. Chadwick, Physicochemical studies of indocyanine green (ICG): absorbance/concentration relationship, pH tolerance and assay precision in various solvents, *Experientia*. 38 (1982) 1441–1442.
<https://doi.org/10.1007/BF01955757>.
- [87] H. Wang, X. Li, B.W.C. Tse, H. Yang, C.A. Thorling, Y. Liu, M. Touraud, J.B.

- Chouane, X. Liu, M.S. Roberts, X. Liang, Indocyanine green-incorporating nanoparticles for cancer theranostics, *Theranostics*. 8 (2018) 1227–1242. <https://doi.org/10.7150/thno.22872>.
- [88] S.A. Hilderbrand, R. Weissleder, Near-infrared fluorescence: application to in vivo molecular imaging, *Curr. Opin. Chem. Biol.* 14 (2010) 71–79. <https://doi.org/10.1016/j.cbpa.2009.09.029>.
- [89] C.S. Shemesh, C.W. Hardy, D.S. Yu, B. Fernandez, H. Zhang, Indocyanine green loaded liposome nanocarriers for photodynamic therapy using human triple negative breast cancer cells, *Photodiagnosis Photodyn. Ther.* 11 (2014) 193–203. <https://doi.org/10.1016/j.pdpdt.2014.02.001>.
- [90] E.A. Hussein, M.M. Zagho, G.K. Nasrallah, A.A. Elzatahry, Recent advances in functional nanostructures as cancer photothermal therapy, *Int. J. Nanomedicine*. 13 (2018) 2897–2906. <https://doi.org/10.2147/IJN.S161031>.
- [91] M. Ogawa, N. Kosaka, P.L. Choyke, H. Kobayashi, In vivo molecular imaging of cancer with a quenching near-infrared fluorescent probe using conjugates of monoclonal antibodies and indocyanine green, *Cancer Res.* 69 (2009) 1268–1272. <https://doi.org/10.1158/0008-5472.CAN-08-3116>.
- [92] J.T. Alander, I. Kaartinen, A. Laakso, T. Pääliä, T. Spillmann, V. V. Tuchin, M. Venermo, P. Väisänen, A Review of indocyanine green fluorescent imaging in surgery, *Int. J. Biomed. Imaging*. 2012 (2012). <https://doi.org/10.1155/2012/940585>.
- [93] S. Fickweiler, R.M. Szeimies, W. Bäumler, P. Steinbach, S. Karrer, A.E. Goetz, C. Abels, F. Hofstädter, M. Landthaler, Indocyanine green: Intracellular uptake and phototherapeutic effects in vitro, *J. Photochem. Photobiol. B Biol.* 38 (1997) 178–183. [https://doi.org/10.1016/S1011-1344\(96\)07453-2](https://doi.org/10.1016/S1011-1344(96)07453-2).
- [94] J. Kou, D. Dou, L. Yang, Porphyrin photosensitizers in photodynamic therapy and its applications, *Oncotarget*. 8 (2017) 81591–81603. <https://doi.org/10.18632/oncotarget.20189>.

- [95] S.A. Fahmy, H.M.E.S. Azzazy, J. Schaefer, Liposome photosensitizer formulations for effective cancer photodynamic therapy, *Pharmaceutics*. 13 (2021). <https://doi.org/10.3390/pharmaceutics13091345>.
- [96] M.T. Jarvi, M.J. Niedre, M.S. Patterson, B.C. Wilson, Singlet Oxygen Luminescence Dosimetry (SOLD) for Photodynamic Therapy: Current Status, Challenges and Future Prospects, *Photochem. Photobiol.* 82 (2006) 1198. <https://doi.org/10.1562/2006-05-03-ir-891>.
- [97] D.E.J.G.J. Dolmans, D. Fukumura, R.K. Jain, Photodynamic therapy for cancer, *Nat. Rev. Cancer*. 3 (2003) 380–387. <https://doi.org/10.1038/nrc1071>.
- [98] W.S. Kuo, Y.T. Chang, K.C. Cho, K.C. Chiu, C.H. Lien, C.S. Yeh, S.J. Chen, Gold nanomaterials conjugated with indocyanine green for dual-modality photodynamic and photothermal therapy, *Biomaterials*. 33 (2012) 3270–3278. <https://doi.org/10.1016/j.biomaterials.2012.01.035>.
- [99] T. Maisch, J. Baier, B. Franz, M. Maier, M. Landthaler, R.M. Szeimies, W. Bäumler, The role of singlet oxygen and oxygen concentration in photodynamic inactivation of bacteria, *Proc. Natl. Acad. Sci. U. S. A.* 104 (2007) 7223–7228. <https://doi.org/10.1073/pnas.0611328104>.
- [100] K.R. Weishaupt, C.J. Gomer, T.J. Dougherty, Identification of Singlet Oxygen as the Cytotoxic Agent in Photo-inactivation of a Murine Tumor, *Cancer Res.* 36 (1976) 2326–2329.
- [101] H. Sun, M. Feng, S. Chen, R. Wang, Y. Luo, B. Yin, J. Li, X. Wang, Near-infrared photothermal liposomal nanoantagonists for amplified cancer photodynamic therapy, *J. Mater. Chem. B.* 8 (2020) 7149–7159. <https://doi.org/10.1039/d0tb01437k>.
- [102] M.B. Azad, Y. Chen, S.B. Gibson, Regulation of autophagy by reactive oxygen species (ROS): Implications for cancer progression and treatment, *Antioxidants Redox Signal.* 11 (2009) 777–790. <https://doi.org/10.1089/ars.2008.2270>.
- [103] G. Barkleit, *Krebsforschung: Scheitern eines innovativen Ansatzes* Manfred von

- Ardenne und die Krebs-Mehrschritt-Therapie, *Dtsch. Arztebl.* 102 (2005) A344–A348.
- [104] D. Zhi, T. Yang, J. O'Hagan, S. Zhang, R.F. Donnelly, Photothermal therapy, *J. Control. Release.* 325 (2020) 52–71. <https://doi.org/10.1016/j.jconrel.2020.06.032>.
- [105] H.J. Yoon, H.S. Lee, J.Y. Lim, J.H. Park, Liposomal indocyanine green for enhanced photothermal therapy, *ACS Appl. Mater. Interfaces.* 9 (2017) 5683–5691. <https://doi.org/10.1021/acsami.6b16801>.
- [106] J. Li, W. Zhang, W. Ji, J. Wang, N. Wang, W. Wu, Q. Wu, X. Hou, W. Hu, L. Li, Near infrared photothermal conversion materials: mechanism, preparation, and photothermal cancer therapy applications, *J. Mater. Chem. B.* 9 (2021) 7909–7926. <https://doi.org/10.1039/d1tb01310f>.
- [107] Z. Su, P. Ye, Y. Teng, L. Zhang, X. Shu, Adverse reaction in patients with drug allergy history after simultaneous intravenous fundus fluorescein angiography and indocyanine green angiography, *J. Ocul. Pharmacol. Ther.* 28 (2012) 410–413. <https://doi.org/10.1089/jop.2011.0221>.
- [108] N. Bouchenaki, C.P. Herbort, Indocyanine green angiography guided management of vogt-koyanagi-harada disease, *J. Ophthalmic Vis. Res.* 6 (2011) 241–248.
- [109] Z. Jing, S. Ou, Y. Ban, Z. Tong, Y. Wang, Intraoperative assessment of anterior circulation aneurysms using the indocyanine green video angiography technique, *J. Clin. Neurosci.* 17 (2010) 26–28. <https://doi.org/10.1016/j.jocn.2009.03.034>.
- [110] A. Raabe, J. Beck, R. Gerlach, M. Zimmermann, V. Seifert, R.L. Macdonald, B. Meyer, W.R. Selman, Near-infrared indocyanine green video angiography: A new method for intraoperative assessment of vascular flow, *Neurosurgery.* 52 (2003) 132–139. <https://doi.org/10.1097/00006123-200301000-00017>.
- [111] K. Gotoh, T. Yamada, O. Ishikawa, H. Takahashi, H. Eguchi, M. Yano, H. Ohigashi, Y. Tomita, Y. Miyamoto, S. Imaoka, A novel image-guided surgery of

- hepatocellular carcinoma by indocyanine green fluorescence imaging navigation, *J. Surg. Oncol.* 100 (2009) 75–79. <https://doi.org/10.1002/jso.21272>.
- [112] S.G. Werner, H.E. Langer, S. Ohrndorf, M. Bahner, P. Schott, C. Schwenke, M. Schirner, H. Bastian, G. Lind-Albrecht, B. Kurtz, G.R. Burmester, M. Backhaus, Inflammation assessment in patients with arthritis using a novel in vivo fluorescence optical imaging technology, *Ann. Rheum. Dis.* 71 (2012) 504–510. <https://doi.org/10.1136/annrheumdis-2010-148288>.
- [113] A.M. Glimm, S.G. Werner, G.R. Burmester, M. Backhaus, S. Ohrndorf, Analysis of distribution and severity of inflammation in patients with osteoarthritis compared to rheumatoid arthritis by ICG-enhanced fluorescence optical imaging and musculoskeletal ultrasound: A pilot study, *Ann. Rheum. Dis.* 75 (2016) 566–570. <https://doi.org/10.1136/annrheumdis-2015-207345>.
- [114] D. Murawa, C. Hirche, S. Dresel, M. Hünerbein, Sentinel lymph node biopsy in breast cancer guided by indocyanine green fluorescence, *Br. J. Surg.* 96 (2009) 1289–1294. <https://doi.org/10.1002/bjs.6721>.
- [115] M. Fujiwara, T. Mizukami, A. Suzuki, H. Fukamizu, Sentinel lymph node detection in skin cancer patients using real-time fluorescence navigation with indocyanine green: preliminary experience, *J. Plast. Reconstr. Aesthetic Surg.* 62 (2009) e373–e378. <https://doi.org/10.1016/j.bjps.2007.12.074>.
- [116] T. Kitai, T. Inomoto, M. Miwa, T. Shikayama, Fluorescence navigation with indocyanine green for detecting sentinel lymph nodes in breast cancer, *Breast Cancer.* 12 (2005) 211–215. <https://doi.org/10.2325/jbcs.12.211>.
- [117] I. Miyashiro, N. Miyoshi, M. Hiratsuka, K. Kishi, T. Yamada, M. Ohue, H. Ohigashi, M. Yano, O. Ishikawa, S. Imaoka, Detection of sentinel node in gastric cancer surgery by indocyanine green fluorescence imaging: Comparison with infrared imaging, *Ann. Surg. Oncol.* 15 (2008) 1640–1643. <https://doi.org/10.1245/s10434-008-9872-7>.
- [118] E. Tanaka, H.S. Choi, H. Fujii, M.G. Bawendi, J. V. Frangioni, Image-guided

- oncologic surgery using invisible light: Completed pre-clinical development for sentinel lymph node mapping, *Ann. Surg. Oncol.* 13 (2006) 1671–1681. <https://doi.org/10.1245/s10434-006-9194-6>.
- [119] L.T. Hoekstra, W. De Graaf, G.A.A. Nibourg, M. Heger, R.J. Bennink, B. Stieger, T.M. Van Gulik, Physiological and biochemical basis of clinical liver function tests, *Ann. Surg.* 257 (2013) 27–36. <https://doi.org/10.1097/SLA.0b013e31825d5d47>.
- [120] M. Hope-Ross, L.A. Yannuzzi, E.S. Gragoudas, D.R. Guyer, J.S. Slakter, J.A. Sorenson, S. Krupsky, D.A. Orlock, C.A. Puliafito, Adverse reactions due to Indocyanine Green, *Ophthalmology.* 101 (1994) 529–533. [https://doi.org/10.1016/S0161-6420\(94\)31303-0](https://doi.org/10.1016/S0161-6420(94)31303-0).
- [121] X. Jiang, B. Du, Y. Huang, M. Yu, J. Zheng, Cancer Photothermal Therapy with ICG-Conjugated Gold Nanoclusters, *Bioconjug. Chem.* 31 (2020) 1522–1528. <https://doi.org/10.1021/acs.bioconjchem.0c00172>.
- [122] N. Beziere, N. Lozano, A. Nunes, J. Salichs, D. Queiros, K. Kostarelos, V. Ntziachristos, Dynamic imaging of PEGylated indocyanine green (ICG) liposomes within the tumor microenvironment using multi-spectral optoacoustic tomography (MSOT), *Biomaterials.* 37 (2015) 415–424. <https://doi.org/10.1016/j.biomaterials.2014.10.014>.
- [123] Z. Deng, Y. Xiao, M. Pan, F. Li, W. Duan, L. Meng, X. Liu, F. Yan, H. Zheng, Hyperthermia-triggered drug delivery from iRGD-modified temperature-sensitive liposomes enhances the anti-tumor efficacy using high intensity focused ultrasound, *J. Control. Release.* 243 (2016) 333–341. <https://doi.org/10.1016/j.jconrel.2016.10.030>.
- [124] K.M. Camacho, S. Menegatti, D.R. Vogus, A. Pusuluri, Z. Fuchs, M. Jarvis, M. Zakrewsky, M.A. Evans, R. Chen, S. Mitragotri, DAFODIL: A novel liposome-encapsulated synergistic combination of doxorubicin and 5FU for low dose chemotherapy, *J. Control. Release.* 229 (2016) 154–162.

- <https://doi.org/10.1016/j.jconrel.2016.03.027>.
- [125] T. Zheng, G.G. Li, F. Zhou, R. Wu, J.J. Zhu, H. Wang, Gold-nanosponge-based multistimuli-responsive drug vehicles for targeted chemo-photothermal therapy, *Adv. Mater.* 28 (2016) 8218–8226. <https://doi.org/10.1002/adma.201602486>.
- [126] H. Gao, Y. Bi, X. Wang, M. Wang, M. Zhou, H. Lu, J. Gao, J. Chen, Y. Hu, Near-Infrared guided thermal-responsive nanomedicine against orthotopic superficial bladder cancer, *ACS Biomater. Sci. Eng.* 3 (2017) 3628–3634. <https://doi.org/10.1021/acsbiomaterials.7b00405>.
- [127] E.C. Costa, A.F. Moreira, D. de Melo-Diogo, V.M. Gaspar, M.P. Carvalho, I.J. Correia, 3D tumor spheroids: An overview on the tools and techniques used for their analysis, *Biotechnol. Adv.* 34 (2016) 1427–1441. <https://doi.org/10.1016/j.biotechadv.2016.11.002>.
- [128] A. Ivascu, M. Kubbies, Rapid generation of single-tumor spheroids for high-throughput cell function and toxicity analysis, *J. Biomol. Screen.* 11 (2006) 922–932. <https://doi.org/10.1177/1087057106292763>.
- [129] A.W. Hamburger, S.E. Salmon, Primary bioassay of human tumor stem cells., *Science.* 197 (1977) 461–463. <https://doi.org/10.1126/science.560061>.
- [130] W.H. Koppenol, P.L. Bounds, C. V. Dang, Otto Warburg’s contributions to current concepts of cancer metabolism, *Nat. Rev. Cancer.* 11 (2011) 325–337. <https://doi.org/10.1038/nrc3038>.
- [131] O. Trédan, C.M. Galmarini, K. Patel, I.F. Tannock, Drug resistance and the solid tumor microenvironment, *J. Natl. Cancer Inst.* 99 (2007) 1441–1454. <https://doi.org/10.1093/jnci/djm135>.
- [132] S. Breslin, L. O’Driscoll, Three-dimensional cell culture: The missing link in drug discovery, *Drug Discov. Today.* 18 (2013) 240–249. <https://doi.org/10.1016/j.drudis.2012.10.003>.
- [133] F. Pampaloni, E.G. Reynaud, E.H.K. Stelzer, The third dimension bridges the gap between cell culture and live tissue., *Nat. Rev. Mol. Cell Biol.* 8 (2007) 839–

845. <https://doi.org/10.1038/nrm2236>.
- [134] M. Kapałczyńska, T. Kolenda, W. Przybyła, M. Zajączkowska, A. Teresiak, V. Filas, M. Ibbs, R. Bliźniak, Ł. Łuczewski, K. Lamperska, 2D and 3D cell cultures - a comparison of different types of cancer cell cultures., *Arch. Med. Sci.* 14 (2018) 910–919. <https://doi.org/10.5114/aoms.2016.63743>.
- [135] K.A. Kilian, B. Bugarija, B.T. Lahn, M. Mrksich, Geometric cues for directing the differentiation of mesenchymal stem cells., *Proc. Natl. Acad. Sci. U. S. A.* 107 (2010) 4872–4877. <https://doi.org/10.1073/pnas.0903269107>.
- [136] C.J. Lovitt, T.B. Shelper, V.M. Avery, Doxorubicin resistance in breast cancer cells is mediated by extracellular matrix proteins, *BMC Cancer.* 18 (2018) 1–11. <https://doi.org/10.1186/s12885-017-3953-6>.
- [137] F. Sams-Dodd, Target-based drug discovery: is something wrong?, *Drug Discov. Today.* 10 (2005) 139–147. [https://doi.org/10.1016/S1359-6446\(04\)03316-1](https://doi.org/10.1016/S1359-6446(04)03316-1).
- [138] A.M. Edwards, C.H. Arrowsmith, C. Bountra, M.E. Bunnage, M. Feldmann, J.C. Knight, D.D. Patel, P. Prinos, M.D. Taylor, M. Sundström, P. Barker, D. Barsyte, M.H. Bengtson, C. Bell, P. Bowness, K.M. Boycott, C. Buser-Doepner, C.L. Carpenter, A.J. Carr, K. Clark, A.M. Das, D. Dhanak, P. Dirks, J. Ellis, V.R. Fantin, C. Flores, E.A. Fon, D.E. Frail, O. Gileadi, R.C. O’Hagan, T. Howe, J.T.R. Isaac, N. Jabado, P.-J. Jakobsson, L. Klareskog, S. Knapp, W.H. Lee, E. Lima-Fernandes, I.E. Lundberg, J. Marshall, K.B. Massirer, A.E. MacKenzie, T. Maruyama, A. Mueller-Fahrnow, S. Muthuswamy, J. Nanchahal, C. O’Brien, U. Oppermann, N. Ostermann, K. Petrecca, B.G. Pollock, V. Poupon, R.K. Prinjha, S.H. Rosenberg, G. Rouleau, M. Skingle, A.S. Slutsky, G.A.M. Smith, D. Verhelle, H. Widmer, L.T. Young, Preclinical target validation using patient-derived cells, *Nat. Rev. Drug Discov.* 14 (2015) 149–150. <https://doi.org/10.1038/nrd4565>.
- [139] M. Wartenberg, F. DÖNmez, F. C. Ling, H. Acker, Jür. Hescheler, H. Sauer, Tumor-induced angiogenesis studied in confrontation cultures of multicellular

- tumor spheroids and embryoid bodies grown from pluripotent embryonic stem cells, *FASEB J.* 15 (2001) 995–1005. <https://doi.org/10.1096/fsb2fj000350com>.
- [140] M. Wartenberg, S. Gronczynska, M.M. Bekhite, T. Saric, W. Niedermeier, J. Hescheler, H. Sauer, Regulation of the multidrug resistance transporter P-glycoprotein in multicellular prostate tumor spheroids by hyperthermia and reactive oxygen species, *Int. J. Cancer.* 113 (2005) 229–240. <https://doi.org/10.1002/ijc.20596>.
- [141] P. Kovacic, J.A. Osuna, Mechanisms of anti-cancer agents: Emphasis on oxidative stress and electron transfer, 2000.
- [142] W. Mueller-Klieser, Tumor biology and experimental therapeutics, *Crit. Rev. Oncol. Hematol.* 36 (2000) 123–139. [https://doi.org/10.1016/s1040-8428\(00\)00082-2](https://doi.org/10.1016/s1040-8428(00)00082-2).
- [143] J. Friedrich, C. Seidel, R. Ebner, & Leoni, A. Kunz-Schughart, L.A. Kunz-Schughart, Spheroid-based drug screen: considerations and practical approach, *Nat. Protoc.* 4 (2009) 309–324. <https://doi.org/10.1038/nprot.2008.226>.
- [144] K.M. Yamada, E. Cukierman, Modeling tissue morphogenesis and cancer in 3D, *Cell.* 130 (2007) 601–610. <https://doi.org/https://doi.org/10.1016/j.cell.2007.08.006>.
- [145] H. Jaganathan, J. Gage, F. Leonard, S. Srinivasan, G.R. Souza, B. Dave, B. Godin, Three-Dimensional In Vitro Co-Culture Model of Breast Tumor using Magnetic Levitation, *Sci. Rep.* 4 (2014) 6468. <https://doi.org/10.1038/srep06468>.
- [146] S. Kessel, S. Cribbes, O. Déry, D. Kuksin, E. Sincoff, J. Qiu, L.L.Y. Chan, High-throughput 3D tumor spheroid screening method for cancer drug discovery using celigo image cytometry, *SLAS Technol.* 22 (2017) 454–465. <https://doi.org/10.1177/2211068216652846>.
- [147] A. Abu Dayyih, M. Alawak, A.M. Ayoub, M.U. Amin, W. Abu Dayyih, K.

- Engelhardt, L. Duse, E. Preis, J. Brüllner, U. Bakowsky, Thermosensitive liposomes encapsulating hypericin: Characterization and photodynamic efficiency, *Int. J. Pharm.* 609 (2021) 121195. <https://doi.org/10.1016/j.ijpharm.2021.121195>.
- [148] A. Fritze, F. Hens, A. Kimpfler, R. Schubert, R. Peschka-Süss, Remote loading of doxorubicin into liposomes driven by a transmembrane phosphate gradient, *Biochim. Biophys. Acta.* 1758 (2006) 1633–1640. <https://doi.org/10.1016/j.bbamem.2006.05.028>.
- [149] L.D. Mayer, L.C.L.L. Tai, M.B. Bally, G.N. Mitilenes, R.S. Ginsberg, P.R. Cullis, Characterization of liposomal systems containing doxorubicin entrapped in response to pH gradients, *BBA - Biomembr.* 1025 (1990) 143–151. [https://doi.org/10.1016/0005-2736\(90\)90091-2](https://doi.org/10.1016/0005-2736(90)90091-2).
- [150] M. Bakonyi, S. Berkó M. Budai-Szűcs, A. Kovács, E. Csányi, DSC for evaluating the encapsulation efficiency of lidocaine-loaded liposomes compared to the ultracentrifugation method, *J. Therm. Anal. Calorim.* 130 (2017) 1619–1625. <https://doi.org/10.1007/s10973-017-6394-1>.
- [151] J. Brüssler, E. Marxer, A. Becker, R. Schubert, J. Schümmelfeder, C. Nimsky, U. Bakowsky, Correlation of structure and echogenicity of nanoscaled ultrasound contrast agents in vitro., *Colloids Surf. B. Biointerfaces.* 117 (2014) 206–215. <https://doi.org/10.1016/j.colsurfb.2014.02.029>.
- [152] M. Alawak, G. Mahmoud, A.A. Dayyih, L. Duse, S.R. Pinnapireddy, K. Engelhardt, I. Awak, C. Wölk, A.M. König, J. Brüllner, U. Bakowsky, Magnetic resonance activatable thermosensitive liposomes for controlled doxorubicin delivery, *Mater. Sci. Eng. C.* 115 (2020) 111116. <https://doi.org/10.1016/j.msec.2020.111116>.
- [153] K.H. Engelhardt, S.R. Pinnapireddy, E. Baghdan, J. Jedelská U. Bakowsky, Transfection studies with colloidal systems containing highly purified bipolar tetraether lipids from *Sulfolobus acidocaldarius*, *Archaea.* 2017 (2017).

- <https://doi.org/10.1155/2017/8047149>.
- [154] N. Plenagl, L. Duse, B.S. Seitz, N. Goergen, S.R. Pinnapireddy, J. Jedelska, J. Brüller, U. Bakowsky, Photodynamic therapy - hypericin tetraether liposome conjugates and their antitumor and antiangiogenic activity., *Drug Deliv.* 26 (2019) 23–33. <https://doi.org/10.1080/10717544.2018.1531954>.
- [155] G. Mahmoud, J. Jedelska & B. Strehlow, S. Omar, M. Schneider, U. Bakowsky, Photo-responsive tetraether lipids based vesicles for porphyrin mediated vascular targeting and direct phototherapy, *Colloids Surfaces B Biointerfaces.* 159 (2017) 720–728. <https://doi.org/10.1016/j.colsurfb.2017.08.049>.
- [156] I. Levacheva, O. Samsonova, E. Tazina, M. Beck-Broichsitter, S. Levachev, B. Strehlow, M. Baryshnikova, N. Oborotova, A. Baryshnikov, U. Bakowsky, Optimized thermosensitive liposomes for selective doxorubicin delivery: Formulation development, quality analysis and bioactivity proof, *Colloids Surfaces B Biointerfaces.* 121 (2014) 248–256. <https://doi.org/10.1016/j.colsurfb.2014.02.028>.
- [157] C. Gunawan, M. Lim, C.P. Marquis, R. Amal, Nanoparticle-protein corona complexes govern the biological fates and functions of nanoparticles, *J. Mater. Chem. B.* 2 (2014) 2060–2083. <https://doi.org/10.1039/c3tb21526a>.
- [158] S.S. Raesch, S. Tenzer, W. Storck, A. Rurainski, D. Selzer, C.A. Ruge, J. Perez-Gil, U.F. Schaefer, C.M. Lehr, Proteomic and Lipidomic Analysis of Nanoparticle Corona upon Contact with Lung Surfactant Reveals Differences in Protein, but Not Lipid Composition, *ACS Nano.* 9 (2015) 11872–11885. <https://doi.org/10.1021/acsnano.5b04215>.
- [159] D. Papahadjopoulos, K. Jacobson, S. Nir, I. Isac, Phase transitions in phospholipid vesicles Fluorescence polarization and permeability measurements concerning the effect of temperature and cholesterol, *BBA - Biomembr.* 311 (1973) 330–348. [https://doi.org/10.1016/0005-2736\(73\)90314-3](https://doi.org/10.1016/0005-2736(73)90314-3).
- [160] B. Weigelt, A.T. Lo, C.C. Park, J.W. Gray, M.J. Bissell, HER2 signaling

- pathway activation and response of breast cancer cells to HER2-targeting agents is dependent strongly on the 3D microenvironment, *Breast Cancer Res. Treat.* 122 (2010) 35–43. <https://doi.org/10.1007/s10549-009-0502-2>.
- [161] V.M. Le, M.D. Lang, W. Bin Shi, J.W. Liu, A collagen-based multicellular tumor spheroid model for evaluation of the efficiency of nanoparticle drug delivery, *Artif. Cells, Nanomedicine Biotechnol.* 44 (2016) 540–544. <https://doi.org/10.3109/21691401.2014.968820>.
- [162] K.S. McMillan, A.G. McCluskey, A. Sorensen, M. Boyd, M. Zagnoni, Emulsion technologies for multicellular tumour spheroid radiation assays, *Analyst.* 141 (2016) 100–110. <https://doi.org/10.1039/c5an01382h>.
- [163] X. Gong, C. Lin, J. Cheng, J. Su, H. Zhao, T. Liu, X. Wen, P. Zhao, Generation of multicellular tumor spheroids with microwell-based agarose scaffolds for drug testing, *PLoS One.* 10 (2015) 1–18. <https://doi.org/10.1371/journal.pone.0130348>.
- [164] G. Lazzari, P. Couvreur, S. Mura, Multicellular tumor spheroids: A relevant 3D model for the: In vitro preclinical investigation of polymer nanomedicines, *Polym. Chem.* 8 (2017) 4947–4969. <https://doi.org/10.1039/c7py00559h>.
- [165] H. Cui, X. Wang, J. Wesslowski, T. Tronser, J. Rosenbauer, A. Schug, G. Davidson, A.A. Popova, P.A. Levkin, Assembly of Multi-Spheroid Cellular Architectures by Programmable Droplet Merging, *Adv. Mater.* 33 (2021) 2006434. <https://doi.org/10.1002/adma.202006434>.
- [166] R. Tomasi, S. Sart, T. Champetier, C. Baroud, Studying 3D cell cultures in a microfluidic droplet array under multiple time-resolved conditions, *BioRxiv.* XXX (2018) 407759. <https://doi.org/10.1101/407759>.
- [167] D.P. Saraiva, A.T. Matias, S. Braga, A. Jacinto, M.G. Cabral, Establishment of a 3D co-culture with MDA-MB-231 breast cancer cell line and patient-derived immune cells for application in the development of immunotherapies, *Front. Oncol.* 10 (2020) 1–13. <https://doi.org/10.3389/fonc.2020.01543>.

-
- [168] N.H. Baek, O.W. Seo, M.S. Kim, J. Hulme, S.S.A. An, Monitoring the effects of doxorubicin on 3D-spheroid tumor cells in real-time, *Onco. Targets. Ther.* 9 (2016) 7207–7218. <https://doi.org/10.2147/OTT.S112566>.
- [169] Y. Wang, A.B. Hummon, MS imaging of multicellular tumor spheroids and organoids as an emerging tool for personalized medicine and drug discovery, *J. Biol. Chem.* 297 (2021) 101139. <https://doi.org/10.1016/j.jbc.2021.101139>.
- [170] L. Yu, A. Dong, R. Guo, M. Yang, L. Deng, J. Zhang, DOX/ICG Coencapsulated Liposome-Coated Thermosensitive Nanogels for NIR-Triggered Simultaneous Drug Release and Photothermal Effect, *ACS Biomater. Sci. Eng.* 4 (2018) 2424–2434. <https://doi.org/10.1021/acsbiomaterials.8b00379>.
- [171] E. Preis, T. Anders, J. Širc, R. Hobzova, A.I. Cocarta, U. Bakowsky, J. Jedelská, Biocompatible indocyanine green loaded PLA nanofibers for in situ antimicrobial photodynamic therapy, *Mater. Sci. Eng. C.* 115 (2020). <https://doi.org/10.1016/j.msec.2020.111068>.

6.2 Abbreviations

AFM	Atomic force microscopy
ATCC	American type culture collection
CAM	Chorioallantoic membrane
CLSM	Confocal laser scanning microscopy
DAPI	4', 6-Diamidin-2-phenylindol
DLS	Dynamic light scattering
DMEM	Dulbecco's modified eagle medium
DMSO	Dimethyl sulfoxide
DOX	Doxorubicin
DSC	Differential scanning calorimetry
ICG	Indocyanine green
IC50	Half-maximal inhibitory concentration
LDV	Laser doppler velocimetry
MCTS	Multicellular tumor spheroid
NIR	Near-infrared
PBS	Phosphate buffered saline
PdI	Polydispersity index
PDT	Photodynamic therapy
PI	Propidium iodide
PS	Photosensitizer
PTT	Photothermal therapy
ROS	Reactive oxygen species
SEC	Size exclusion chromatography
TEM	Transmission electron microscopy
TIME	Tumor immune microenvironment
T _m	Phase transition temperature
TNBC	Triple negative breast cancer

T_p	Pretransition temperature
TSL	Thermosensitive liposomes

6.3 List of figures

Figure 1: A: Ultraviolet and visible spectrum of Doxorubicin hydrochloride in methanol.....	3
Figure 2: Classification of vesicle size and lamellarity.	6
Figure 3: Overview of liposome structure classification.	8
Figure 4: Chemical structure of the lipids used in liposomal formulations.....	9
Figure 5: Schematic illustration of the doxorubicin remote loading by using trans-membrane ammonium sulfate gradient.....	11
Figure 6: Schematic representation of the phase transition behavior of TSL.....	13
Figure 7: Schematic representation of tumor targeting via enhanced permeability and retention (EPR) effect	14
Figure 8: Temperature range of thermal treatment in cancer therapy.....	17
Figure 9: A: Chemical structure of Indocyanine Green (ICG). B: The absorption and emission fluorescence spectra of Indocyanine Green (ICG).....	19
Figure 10: Representation of photodynamic therapy (PDT) mechanism of Type I and Type II reactions.....	21
Figure 11: Mechanism of photothermal therapy (PTT).	23
Figure 12: Schematic representation of spheroid structure.....	26
Figure 13: Comparison of 2D cell culture and 3D cell culture.....	28
Figure 14: Schematic representation of the thin film hydration method for preparing liposomes	38
Figure 15: schematic representation of the seeding format on 96 well plate of spheroid generation.....	45
Figure 16: A: Schematic representation of DOX-TSL	49
Figure 17: DSC thermogram of TSL and mTSL	51
Figure 18: Atomic force microscopy (AFM) micrographs of TSL and DOX-TSL	53
Figure 19: Transmission electron micrographs (TEM) of TSL and DOX-TSL...	54

Figure 20: DLS Size analysis of DOX-TSL in DMEM/10% FCS	56
Figure 21: Cumulative release profile of DOX from DOX-TSL.....	57
Figure 22: Size and geometry of MDA-MB-231 spheroid generation with and without collagen I	60
Figure 23: MDA-MB-231 spheroids represent the proliferating zone, quiescent zone and necrotic zone.....	60
Figure 24: Proliferation of MDA-MB-231 spheroids in different seeding densities	62
Figure 25: The fusion process of two MDA-MB-231 spheroids over 6 days.	63
Figure 26: Relative 3D cell viability of MDA-MB-231 spheroids treated with DOX-TSL	65
Figure 27: Relative 3D cell viability of MDA-MB-231 treated with DOX-TSL at different temperature.....	67
Figure 28: Structure of 1000 cells seeded MDA-MB-231 spheroid on day 5	69
Figure 29: Confocal laser scanning acquisitions of MDA-MB-231 spheroids treated with DOX-TSL or free DOX.	73
Figure 30: Temperature-dependent confocal laser scanning acquisitions of MDA-MB-231 spheroids treated with DOX-TSL or free DOX.....	74
Figure 31: A: Schematic representation of ICG-DOX-mTSL.	75
Figure 32: Transmission electron micrographs (TEM) and Atomic force microscopy (AFM) images of ICG-mTSL	79

6.4 List of tables

Table 1: Lipid compositions of the prepared liposomes.	37
Table 2: Physiochemical properties of TSL and DOX-TSL liposomes.	50
Table 3: Colloidal stability of DOX-TSL for 6 weeks in dark at 4 °C.....	55
Table 4: Serum stability of DOX-TSL incubated in DMEM.....	56
Table 5: Physiochemical properties of mTSL, ICG-mTSL and ICG-DOX-mTSL.	77

6.5 Publications and Presentations

Tan Shi, Abdallah M. Ayoub, Alice Abu Dayyih, Muhammad Umair Amin, Konrad H. Engelhardt, Mohamad Alawak, Udo Bakowsky. The efficacy of doxorubicin thermosensitive liposomes under mild hyperthermia in 3D cell culture (2023), Manuscript in preparation

Abdallah M. Ayoub, Lena Bender, Ibrahim Awak, **Tan Shi**, Muhammad Umair Amin, Jens Schäfer, Udo Bakowsky. Preparation of Pirarubicin liposomes by dual asymmetric centrifuge (2023), Manuscript in preparation

Abdallah M. Ayoub, Jan Schulze, Ibrahim Awak, **Tan Shi**, Muhammad Umair Amin, Udo Bakowsky. Dual Asymmetric centrifuge as a novel method for preparation of different paclitaxel liposomes (2023), Manuscript in preparation.

Targeted thermosensitive Doxorubicin liposomes in 3D cell culture (**Poster**), **Tan Shi**, Alice Abu Dayyih, Mohamad Alawak, Muhammad Umair Amin, Udo Bakowsky. CRS local chapter 2021, Aachen

6.6 Curriculum vitae

PROFESSIONAL INFORMATION

Name	Tan Shi
Date of birth	30.01.1990
Place of birth	Heilongjiang, China
Nationality	Chinese

PROFESSIONAL EXPERIENCE

October 2018 - present	Research assistant (PhD candidate) Institute of Pharmaceutics and Biopharmaceutics Philipps University of Marburg Marburg, Germany
April 2014- June 2018	Ultrasound clinical doctor Guangdong Hospital of Traditional Chinese Medicine Guangzhou, China
October 2013 – March 2014	Clinical Medicine Intern (Ultrasound assistant) Shenzhen Baoxing Hospital Shenzhen, China
July 2012 -September 2013	Clinical Medicine Intern Jiamusi Central Hospital/ Longgang Central Hospital Jiamusi, China / Shenzhen, China

Education and Training

April. 2019 – Present	PhD in Pharmaceutics and Biopharmaceutics Philipps University of Marburg Marburg, Germany
------------------------------	--

April 2014 – December 2017 **Resident Standardization in Ultrasound medicine**
Guangdong Hospital of Traditional Chinese Medicine
Guangzhou, China

August 2008 – June 2014 **Bachelor in Applied Psychology**
Jiamusi University/ Harbin Normal University
Jiamusi, China/ Harbin, China

August 2008 – June 2013 **Bachelor in Clinical Medicine**
Jiamusi University
Jiamusi, China